Bringing bioelectricity to light: all-optical electrophysiology using microbial rhodopsins

Citation	Hochbaum, Daniel Ron. 2014. Bringing bioelectricity to light: all-optical electrophysiology using microbial rhodopsins. Doctoral dissertation, Harvard University.
Accessed	July 15, 2016 4:52:30 PM EDT
Citable Link	http://nrs.harvard.edu/urn-3:HUL.InstRepos:13064932
Terms of Use	This article was downloaded from Harvard University's DASH repository, and is made available under the terms and conditions applicable to Other Posted Material, as set forth at http://nrs.harvard.edu/urn-3:HUL.InstRepos:dash.current.terms-of-use#LAA

Bringing bioelectricity to light: all-optical electrophysiology using microbial rhodopsins

A dissertation presented
by
Daniel Ron Hochbaum
to
The School of Engineering and Applied Sciences
in partial fulfillment of the requirements
for the degree of
Doctor of Philosophy
in the subject of
Applied Physics

Harvard University
Cambridge, Massachusetts
September 2014

Adam Ezra Cohen Daniel Ron Hochbaum

Bringing bioelectricity to light: all-optical electrophysiology using microbial rhodopsins

Abstract

My work has focused on the development and application of fluorescent voltage-sensitive proteins based on microbial rhodopsins. These probes led to the discovery of electrical activity in the bacterium *Escherichia coli*, the first robust optical recordings of action potentials (APs) in mammalian neurons using a genetically encoded voltage reporter, and the development of a genetically targetable all-optical electrophysiology system.

I first introduce an engineered fluorescent voltage sensor based on green-absorbing proteorhodopsin. Expression of the proteorhodopsin optical proton sensor (PROPS) in *E. coli* revealed electrical spiking at up to 1 hertz. Spiking was sensitive to chemical and physical perturbations and coincided with rapid efflux of a small-molecule fluorophore, suggesting that bacterial efflux machinery may be electrically regulated.

I then present another microbial rhodopsin, Archaerhodopsin 3 (Arch), whose endogenous fluorescence exhibited a twofold increase in brightness between −150 mV and +150 mV and a sub-millisecond response time. In rat hippocampal neurons, Arch detected single electrically triggered APs with an optical signal-to-noise ratio > 10. A mutant, Arch(D95N), lacked endogenous proton pumping and had 50% greater sensitivity than the wild type but had a slower response (41 ms). Nonetheless, Arch(D95N) also resolved individual APs.

Finally, I introduce evolved archaerhodopsin-based voltage indicators and a spectrally orthogonal channelrhodopsin actuator, which together enabled all-optical electrophysiology. A directed evolution screen yielded two mutants, QuasAr1 and QuasAr2, that showed improved brightness and voltage sensitivity relative to previous archaerhodopsin-based sensors, and microsecond response times. An engineered channelrhodopsin actuator, CheRiff, showed high light sensitivity and rapid kinetics. A coexpression vector, Optopatch, enabled cross-talk–free genetically targeted all-optical electrophysiology. In cultured neurons, the Optopatch system probed membrane voltage across temporal and spatial scales, from the sub-cellular and sub-millisecond dynamics of AP propagation, to the simultaneous measurement of firing patterns of many neurons in a circuit. In brain slices, Optopatch induced and reported APs and subthreshold events with high signal-to-noise ratios. In human stem cell-derived neurons, Optopatch measurements revealed homeostatic tuning of intrinsic excitability, a subtle form of plasticity that had yet to be observed in human neurons.

The suite of tools and techniques presented here enable high-throughput, genetically targeted, and spatially resolved electrophysiology without the use of conventional electrodes.

Contents

AUTHOR LIST

The author for **Chapter 1** is D. R. Hochbaum.

The authors for **Chapter 2** are J. M. Kralj, D. R. Hochbaum, A. D. Douglass, and A. E. Cohen.

The authors for **Chapter 3** are D. R. Hochbaum, J. M. Kralj, A. D. Douglass, D. Maclaurin, and A. E. Cohen.

The authors for **Chapter 4** are D. R. Hochbaum, Y. Zhao, S. Farhi, N. Klapoetke, C. A. Werley, V. Kapoor, P. Zou, J. M. Kralj, D. Maclaurin, N. Smedemark-Margulies, J. Saulnier, G. L. Boulting, Y. Cho, M. Melkonian, G. K. Wong, D. J. Harrison, V. N. Murthy, B. L. Sabatini, E. S. Boyden, R. E. Campbell, and A. E. Cohen.

The author for **Chapter 5** is Daniel R Hochbaum.

Detailed information about author contributions are provided at the end of each chapter in the section entitled "Manuscript Information."

Acknowledgments

The work presented in this thesis would not have been possible without the support, guidance, and help of many individuals. I would first like to sincerely thank my advisor, Professor Adam Cohen. I appreciate the time you have invested in my development as a scientist. Your hands-on instruction was invaluable, and your enthusiasm was and still is infectious. I am deeply grateful.

I began my PhD working with Joel Kralj and Adam Douglass. I'm grateful to Joel for introducing me to the wonderful world of microbial rhodopsins, and to Adam for teaching me the nitty-gritty of neuroscience. I will not forget our first Arch recordings together, jumping for joy, and in the process, ruining our first traces.

I have learned so much from my present and former lab mates: Alex Fields, Jen Hou, Veena Venkatachalam, Dougal Maclaurin, Sami Farhi, Christopher Werley, Daan Brinks, Nan Yang, Sabrina Leslie, Hohjai Lee, Peng Zou, Yoav Adam, Shan Lou, Miao-Ping Chien, Min Ju Shon, Halil Bayraktar, and Yiqao Tang. Thank you all for creating such a wonderful and supportive environment to work in.

I am indebted to Lucy Rosenbaum, Tony Shen, Vedha Nathan, Nik Smedemark-Margulies, Vaibhav Joshi, Katherine Williams, Jeffrey Fosdick, and Magdalena Kenar for valuable assistance over the years. Thank you.

I'd also like to extend my gratitude to Sami Farhi and our collaborators Yongxin Zhao and Nathan Klapoetke for their contributions to the Optopatch project.

Thanks to my dissertation advisory committee: Sunney Xie, Venki Murthy, Evelyn Hu, and Vinny Manoharan; and my thesis committee: Evelyn Hu, and Daniel Needleman.

Finally, and most importantly, I'd like to thank my parents, Aharon and Dorit Hochbaum, and my brother, Allon Hochbaum, for their unconditional support, mentorship, and constant reminders that there is more to life than the PhD. There is also the postdoc, the faculty position, the marriage, the children, the grandchildren, and skiing.

I'm thankful for financial support from the National Science Foundation.

1

Introduction

NEURONAL FUNCTION and communication rely on a dynamic transmembrane potential. Traditionally, neuroscientists have studied these electrical signals using patch-clamp electrophysiology [116]. While this technique is unparalleled in sensitivity and temporal resolution, it does have inherent limitations. First, electrode-based techniques are typically confined to recording membrane voltage from the neuronal cell body. However, neurons have complex structures and are elaborated with axons, dendrites, and synapses. A neuron's electrical activity at the cell body is the integrated result of signal processing occurring in many subcellular compartments throughout the cell [21, 100], most of which are inaccessible to electrodes [31, 56][1].

Second, intracellular electrode measurements do not readily scale to the non-invasive recording of many neurons in parallel. Ref. [149] is an example of a partic-

---

[1] Hard-to-access structures extend beyond subcellular compartments of neurons. Other nonconventional electrophysiological systems include cellular organelles such as mitochondria [79, 117] and the endoplasmic reticulum [141], microorganisms such as bacteria [32] and yeast [55], and motile cells such as sperm [80] and immune cells [22]. All of these structures and organisms are impractical or impossible to access via electrodes.

ularly heroic experiment, where four neurons are recorded from simultaneously. Extracellular microelectrode arrays can measure the activity of larger ensembles of cells [28], however they blindly record extracellular neuronal signals, which can be difficult or impossible to map back to the original single cell locations and membrane voltage waveforms.

Ideally, to study the interactions underlying neuronal activity in a circuit, one would like to record from many genetically-defined neurons in parallel, with subcellular resolution. Optical techniques are a promising route towards this ambitious goal [139]. In principle, they allow direct measurement of activity over multiple length scales, from subcellular dynamics of individual dendritic spines [123, 135], to simultaneous measurements of many neurons in a circuit [35].

1.1 A BRIEF HISTORY OF OPTICAL RECORDINGS OF NEURONAL MEMBRANE POTENTIAL

Early attempts to optically record electrical signals in neurons employed intrinsic contrast mechanisms. In 1949, Hill and Keynes found that repeated stimulation of a bundle of nerve fibers (from the walking leg of the crab *Carcinus maenas*) was correlated with increased light scattering by the nerve bundle [61]. The minutes-long time course of their optical signal far exceeded the duration of the stimulus, suggesting that it was not a direct readout of membrane potential. Almost 20 years later, Cohen, Hille, and Keynes reported optical birefringence measurements that closely followed the underlying action potential waveform in a squid axon [29]. However, the signals were so small that they required the averaging of thousands of stimuli to produce an optical trace. Although intrinsic contrast techniques have found uses in wide-field brain imaging [50], they are confounded by their sensitivity to other dynamic processes (such as haemodynamic responses), and they do not offer sufficient signal-to-noise for single cell measurements.

Small-molecule voltage sensitive dyes (VSDs) were first used to record neuronal activity in the late 1960s [155]. Early studies demonstrated single-trial recordings of action potentials with single cell resolution in an invertebrate leech preparation [137], and these results were extended to the simultaneous recording of multiple cells [48, 138]. Fluorescent VSDs had sub-millisecond response times, and improved in voltage-sensitivity to the point that synaptic potentials (averaged over several trials) could be observed in individual neuronal processes [51]. While many important subcellular [123], and population-level *in vivo* measurements [15, 78] have been performed using VSDs (for an excellent review, see ref. [47]), a number of factors prevent their widespread use. First, VSDs stain every membrane they come into contact with. This simple fact restricts their use to population-level measurements of mammalian brain activity when introduced extracellularly (due to the dense packing of neurons and glial cells), or to single cell studies when introduced via a patch-pipette. In single cell measurements, the experimenter must typically wait for > 2 hours for the VSD to diffuse from the pipette tip into neuronal processes [129], and in most cases the dye does not fill distal dendrites and axons. VSDs indiscriminately label the internal membranes of the cell, resulting in background fluorescence insensitive to plasma membrane voltage fluctuations, reducing the signal-to-noise of the measurement. Finally, VSDs suffer from issues of phototoxicity which restricts the number of trials and time course of experiments.

Genetically encoded voltage indicators (GEVIs) promise to alleviate many of the limitations of VSDs. Genetic targeting is essential for parsing neural circuitry in intact tissue, where closely spaced cells often perform distinct functions. Genetic targeting *in vitro* is important for characterizing heterogeneous cultures that arise during stem cell differentiation to neurons [18] or while studying neurons cultured with other cell types. The first GEVI ('FlaSh') was reported in 1997 by Siegel and Isacoff [147]. Like many subsequent sensors, FlaSh coupled a voltage-dependent conformational change of a transmembrane protein to a change in fluorescence of a green fluorescent protein (GFP) [130]. This was achieved by fusing the GFP to the C-terminal of a voltage-gated K+ Shaker channel. The detailed mechanism of the voltage-dependent fluorescence remains unclear for this and many similar probes; presumably, the conformational rearrangement induces a change in the local chromophore environment, perturbing the fluorescence. While GEVIs show promise, they have been undermined by a combination of limited voltage sensitivity, slow kinetics, and poor membrane targeting [8, 139]. In the following chapters I will describe a new approach to fluorescent genetically encoded voltage sensing which employs microbial rhodopsins as the GEVI scaffold and offers substantial improvements on voltage sensitivity and speed.

1.2 Genetically encoded calcium-dependent fluorophores as indicators of neuronal activity

Neurons have many voltage- and ligand-dependent calcium conductances. Action potential generation triggers an increase in intracellular calcium concentration. Genetically encoded calcium indicators (GECIs) have matured rapidly over the past ~5 years. The most developed and widely used GECIs are the 'GCaMP' sensors (GCaMP6 [25] is the current iteration) which consist of a circularly permuted GFP fused to the calcium-binding protein calmodulin (CaM) and CaM-interacting M13 peptide. GCaMP sensors can now measure circuit level neuronal activity *in vivo* with single cell resolution [57, 67]. While calcium transients are coincident with super-threshold electrical activity (and NMDA-mediated synaptic events), their kinetics are much slower than the underlying electrical waveforms (hundreds of milliseconds compared to ~1 millisecond), which cannot be accurately recovered solely using GECIs as a readout. Furthermore, most AMPA-mediated sub-threshold depolarizations, and inhibitory hyperpolarizing events cannot be detected using a calcium-sensitive readout. GECI fluorescence is a sufficient proxy for neuronal activity in the context of many important neurobiological questions, however, a direct and robust optical reporter of membrane potential remains elusive.

1.3 Repurposing microbial rhodopsins as fluorescent voltage indicators

Microbial rhodopsins are light-sensitive proteins with seven transmembrane alpha helices that serve a wide variety of functions for their host microorganisms [151]. All microbial rhodopsins contain a retinal chromophore covalently bound via a Schiff base to the protein core, and they all undergo light-induced transformations. My initial work focused on the light-gated proton pump green-absorbing proteorhodopsin (GPR). Upon absorption of a photon, GPR undergoes a number of conformational changes as a proton is pumped across the membrane. These intermediate states of the photocyle change the color of the protein. In particular, deprotonation of the Schiff base results in a dramatic change in peak light absorption [87, 92]. We hypothesized that we could run GPR in reverse:

Instead of using light to pump a proton across the membrane, we could apply a transmembrane voltage to modulate the protonation of the Schiff base, and in doing so change the color of the protein. This mechanism of voltage-induced color shift had been previously reported in dried films of another light-gated proton pump, bacteriorhodopsin [85].

Changes in optical absorption would be challenging to detect in a single cell expressing GPR due to the small quantity of protein in the membrane. Fortunately, GPR was fluorescent in the near-infrared when excited with red light, and to our surprise, *E. coli* expressing our GPR-based indicator showed periodic flashes of fluorescence. We found that the GPR fluorescence was indeed voltage sensitive, and these blinks of fluorescence intensity revealed previously unknown electrical spiking in *E. coli*. This work is described in **Chapter 2**.

I next sought to apply our new fluorescent voltage indicator in mammalian cells. Unfortunately all efforts to express GPR in mammalian cells failed. After an extensive search of homologous proteins, we found that archaerhodopsin 3 (Arch), a proton pump from the microbe *Halorubrum sodomense*, expressed well in mammalian cells and produced fluorescence that responded with exquisite sensitivity and speed to changes in membrane voltage. We expressed Arch in rat hippocampal neurons, and made the first robust optical recordings of action potentials in mammalian neurons using a genetically encoded reporter. This work is described in **Chapter 3**.

However, the Arch voltage sensor had some warts. While Arch was extremely photostable, its fluorescence was dim, and the light used to excite this fluorescence generated a steady-state photocurrent, both undesirable attributes for a fluorescent voltage sensor. We addressed these problems by designing and implementing a directed evolution screen of Arch indicators. We evolved a pair of mutated Arch proteins with improved brightness and sensitivity. The molecules preserved the fast temporal response and photostability of wild-type Arch fluorescence, and lacked the undesirable photocurrents.

The red excitation of these engineered Arch sensors allowed for incorporation of spectrally orthogonal light-gated ion channels (channelrhodopsins, ChRs) [19], enabling simultaneous optical excitation and optical readout of electrical activity in neurons. Existing ChRs lacked the sensitivity to achieve robust all-optical electrophysiology, so we engineered a novel ChR (CheRiff) with high blue light sensitivity and photocurrent. We named our genetically targetable all-optical electrophysiology system ‘Optopatch’.

Using Optopatch, we demonstrated simultaneous excitation and single-trial imaging of electrical activity in intact brain slices. We interrogated networks of cultured neurons expressing Optopatch by activating single neurons and monitoring the synaptic responses in neighboring cells. We probed the membrane potential of single cells subjected to sub-cellular excitation, and mapped the ensuing action potential propagation within the neuron with high spatial and temporal resolution. Finally, we expressed Optopatch in human induced pluripotent stem cell (hiPSC) derived neurons, which show promise as a platform for drug discovery and neuronal disease modeling. The extent to which human iPSC-derived neurons recapitulate the full range of physiology in the brain remains an open question. We used Optopatch to provide the first evidence for homeostatic plasticity of intrinsic excitability, an important aspect of *in vivo* neuronal physiology, in human iPSC-derived neurons. This proof-of-concept experiment demonstrated that high-throughput Optopatch measurements can be a powerful tool for functional characterization of neuronal populations in hiPSC-based disease modeling efforts. This work is described in **Chapter 4**.

2

Electrical spiking in *Escherichia coli* probed with a fluorescent voltage-indicating protein

2.1 Introduction

Bacterial membrane potential provides a major component of the driving force for oxidative phosphorylation, membrane transport, and flagellar motion. Yet this voltage is inaccessible to techniques of conventional electrophysiology, owing to the small size of bacteria and the presence of a cell wall. Little is known about the electrophysiology of bacteria at the level of single cells [107].

We developed a genetically encoded optical indicator of membrane potential, V_m, in bacteria. The starting protein was green-absorbing proteorhodopsin (GPR), a light-driven proton pump found in bacteria in the ocean [12, 13, 151]. In the wild, light-driven transport of a proton through GPR changes the color of the protein. We sought to run GPR backward: to use V_m to reposition a proton, and thereby to induce a color shift [85].

2.2 RESULTS

2.2.1 PROPS: A GPR-BASED FLUORESCENT VOLTAGE SENSOR

The dominant color-determining moiety in GPR is the Schiff base (SB), which links the retinal to the protein core. When the SB was protonated, the protein was pink and weakly fluorescent in the near infrared; when the SB was deprotonated, the protein was yellow and nonfluorescent (**Supplementary Fig. 2.14**).We hypothesized that a change in V_m could alter the local electrochemical potential of protons on the SB, and thereby tip the acid-base equilibrium between the fluorescent and nonfluorescent states (**Supplementary Fig. 2.15**, **Supplementary Text 2.5**). However, the pK_a (acid dissociation constant) of the SB was >12, indicating that protons were bound too tightly to be removed by physiological V_m. The mutant GPR D97N had a SB pK_a of 9.6, showed pH-dependent fluorescence (**Fig. 2.1A**), and also lacked light-induced proton pumping [34], making it a promising candidate voltage sensor. We call GPR D97N a proteorhodopsin optical proton sensor (PROPS).

Induced transmembrane voltage (ITV) [132] was used to calibrate fluorescence versus V_m in intact *Escherichia coli* expressing PROPS (**Methods Section 2.4**). Voltage pulses were applied to field-stimulation electrodes spanning a plate of cells. During the voltage pulse, the depolarized end of each cell became transiently bright, and the hyperpolarized end became transiently dark (**Fig. 2.1B**), indicating a cytoplasm-exposed SB (**Supplementary Text 2.5**). The fluorescence of PROPS was five times as bright at an induced V_m of +70 mV than at −170 mV (**Fig. 2.1C**). The response to a voltage step occurred with a time constant of 4.7 ms (**Fig. 2.1D**).

2.2.2 PROPS FLUORESCENCE REVEALS TRANSIENT ELECTRICAL DEPOLARIZATIONS IN *E. COLI*

E. coli expressing PROPS were imaged at the interface of a coverslip and an agarose pad containing minimal medium. Unexpectedly, many cells exhibited quasi-periodic cell-wide blinks in fluorescence (**Fig. 2.2** and **Supplementary Movies 2.8.1 and 2.8.2**). The blinks occurred simultaneously over an entire

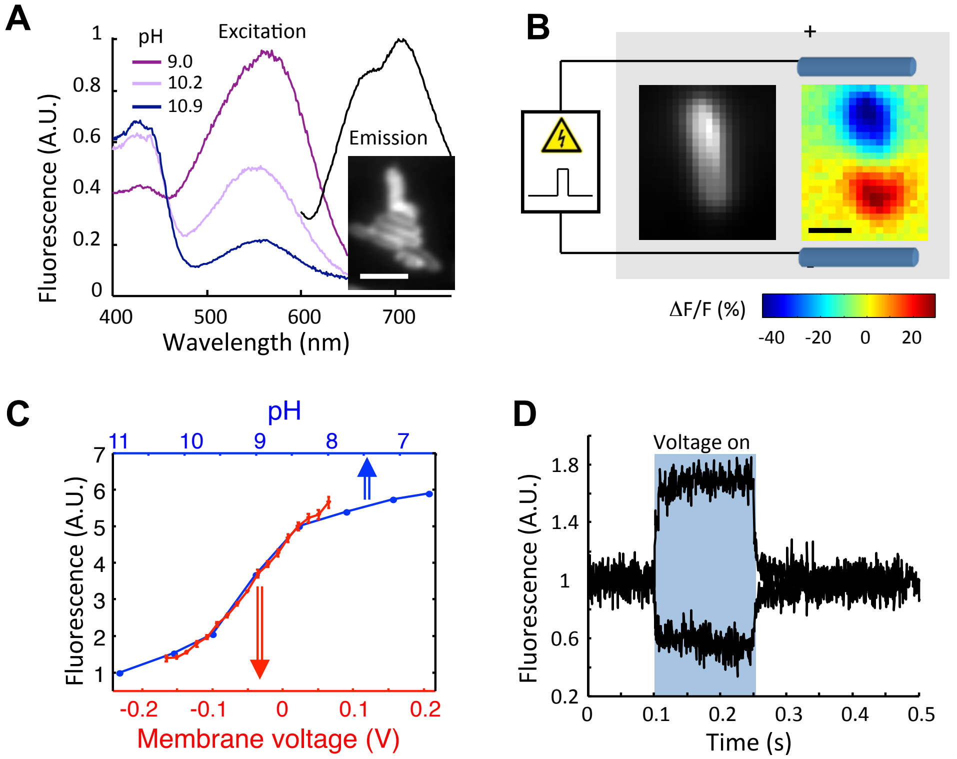

Figure 2.1: PROPS is a fluorescent indicator of bacterial membrane potential. (**A**) Fluorescence spectra of purified PROPS as a function of pH, indicating titration of the Schiff base, with a pK_a of 9.6 (versus >12 in wild-type GPR). Peak emission at $\lambda = 710$ nm, quantum yield 1.0×10^3. PROPS yielded 9.1 times as many photons per molecule before photobleaching as did the GFP (green fluorescent protein) homolog Venus (**Methods Section 2.4**). (Inset) Image of *E. coli* visualized via fluorescence of PROPS (scale bar, 5 μm). Cells were only fluorescent in the presence of retinal (**Supplementary Fig. 2.24**). Expression at ~28,000 copies per cell had a minor effect on growth rate in rich medium (**Methods Section 2.4**). Membrane fractionation yielded protein associated only with the inner membrane (**Methods Section 2.4**). (**B**) Spatially resolved change in fluorescence in a single cell subject to ITV. Scale bar, 2 μm. Electrodes not shown to scale; actual spacing, 1.6 mm. (**C**) Comparison of pH- and voltage- dependent fluorescence of PROPS. A change in membrane potential of 102 mV was equivalent to a change in pH of 1 unit in its effect on fluorescence. The sensitivity was ΔF/F = 150% per 100 mV (**Methods Section 2.4**). Error bars represent s.e.m. (**D**) Time course of the fluorescence response to positive and negative steps in membrane potential. Data in (**B**) to (**D**) represent the average of 20 voltage pulses.

cell, to within the 10-ms time resolution of our imaging system. Blinks were uncorrelated between neighboring cells.

We observed a variety of blinking behaviors within a nominally homogeneous population of cells (**Fig. 2.2A**). Some cells were dark for many minutes, blinked once, and then returned to darkness; others had periods of quiescence punctuated by bursts of blinking. Blinks had durations from 1 to 40 s with rapid rise times followed by slower decays. The intensity of blinks varied within and between cells, but occasionally we observed periodic bursts of blinking to the same brightness. Some cells remained bright for many minutes, and some remained dark. Many individual cells exhibited different motifs at different times. Blinking cells continued to grow and divide when incubated in the dark at 35°C (**Supplementary Fig. 2.16)**.

To determine whether blinks arose from fluctuations in internal pH (pH_i), we co-expressed the cytoplasmic pH indicator super-ecliptic pHluorin [111] and PROPS, and simultaneously observed the fluorescence of both (**Fig. 2.2B**). The pHluorin indicated intracellular pH at the single-cell level with a response time of < 1 s and a precision of better than 0.1 pH units (**Methods Section 2.4**). During a blink, pH_i remained constant to within measurement precision (**Fig. 2.2B** and **Supplementary Fig. 2.17**). Thus, blinks did not arise from fluctuations in pH_i.

To determine whether the blinks arose from electrical fluctuations, we used the torque of the flagellar motor as an indicator of the protonmotive force (PMF) [43]. Cells of strain JY29 were adhered to a coverslip by a single flagellum, and we monitored the blinking of PROPS and the rate of rotation of the cell body simultaneously (**Methods Section 2.4**). During a blink, the rotation slowed or stopped, indicating that blinks coincided with a loss of PMF (**Fig. 2.2C**, **Supplementary Fig. 2.18**, and **Supplementary Movie 2.8.3**). The loss of PMF, but stable pH_i, during a blink implied that blinks arose from electrical depolarization.

Lipophilic voltage-sensitive dyes (VSDs) did not label blinking cells (**Methods Section 2.4**) and thus were unable to provide independent confirmation that blinks were electrical. Within a field of view containing blinking and nonblinking cells, the VSDs only labeled nonblinking cells (**Supplementary Fig. 2.19**). The

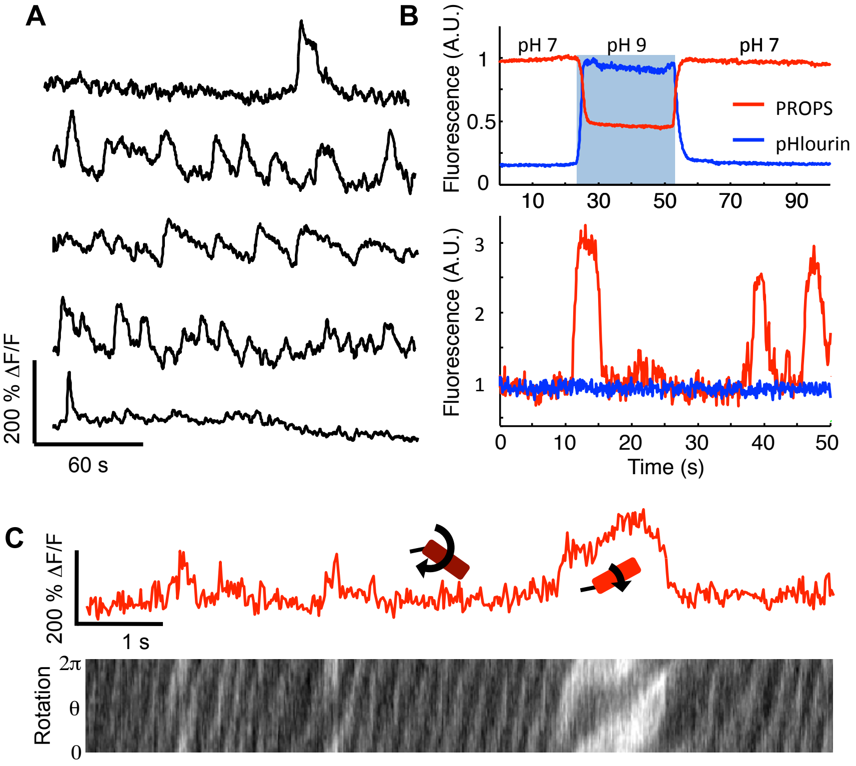

Figure 2.2: *E. coli* expressing PROPS show transient flashes of fluorescence. (**A**) Dynamics of fluorescence intensity (I = 4 W/cm²) of five single cells in a freshly grown sample under an agarose pad containing minimal medium at pH 7.0. (**B**) Top: Simultaneous recording of PROPS and pHluorin fluorescence in *E. coli* treated with CCCP (50 μg/ml) during steps in pH$_o$. Bottom: Intensities of PROPS and pHluorin in a single cell during a blink, in the absence of CCCP. (**C**) Simultaneous measurement of fluorescence (top) and rotation (bottom) of a cell (strain JY29 Δ*cheY*) tethered by its flagellum to a coverslip. Construction of the rotary kymograph is described in **Methods Section 2.4**.

reason for this heterogeneous labeling is unclear. Previous efforts to use VSDs in *E. coli* were unsuccessful [120].

2.2.3 PERTURBATIONS OF *E. COLI* MEMBRANE POTENTIAL

We examined the effect of metabolic state on blinking and pH_i in cells coexpressing PROPS and super-ecliptic pHluorin. Interruption of aerobic respiration caused blinking to cease and all cells to become bright in the PROPS channel. This behavior was seen for inhibition of the electron-transport chain by exposure to intense violet light (**Fig. 2.3A**) [150] or by removal of oxygen (**Fig. 2.3B**). Inhibition of the F_1–adenosine triphosphatase (ATPase) by sodium azide (10 mM, **Fig. 2.3C**) [118] and dissipation of the PMF by carbonyl cyanide *m*-chlorophenyl hydrazone (CCCP; 50 μg/ml, **Fig. 2.3D**) [77] induced similar responses (**Supplementary Movies 2.8.4 to 2.8.7**). None of these treatments affected the fluorescence of purified PROPS. Thus, *E. coli* needed to be alive and undergoing aerobic respiration to blink.

When the experiments above were performed at $pH_i \approx pH_o$ (external pH; corresponding to $pH_o = 8.3$, **Supplementary Fig. 2.20**), the perturbations induced minimal change in pH_i (**Fig. 2.3**). At other values of pH_o, the perturbations caused gradual equilibration of pH_i with pH_o, indicating a failure of pH homeostasis (**Supplementary Fig. 2.21**).

The intensity of the red laser used to image PROPS affected the shape and frequency of the blinks. At higher illumination intensity the blinks were briefer and more intense, and came in more regular and higher-frequency pulse trains (**Fig. 2.3E and 2.3F**). The mechanism by which illumination enhanced blinking is not known; but we note that *E. coli* contain endogenous chromophores in their electron transport chain with absorption throughout the visible spectrum [72]. Heating by the imaging laser is expected to be negligible (**Supplementary Text 2.5**).

2.2.4 TRANSIENT DEPOLARIZATIONS ARE CORRELATED WITH EFFLUX

The enhancement of blinking by increased laser power suggested that blinking might form part of the stress response mechanism in *E. coli*. We thus tested

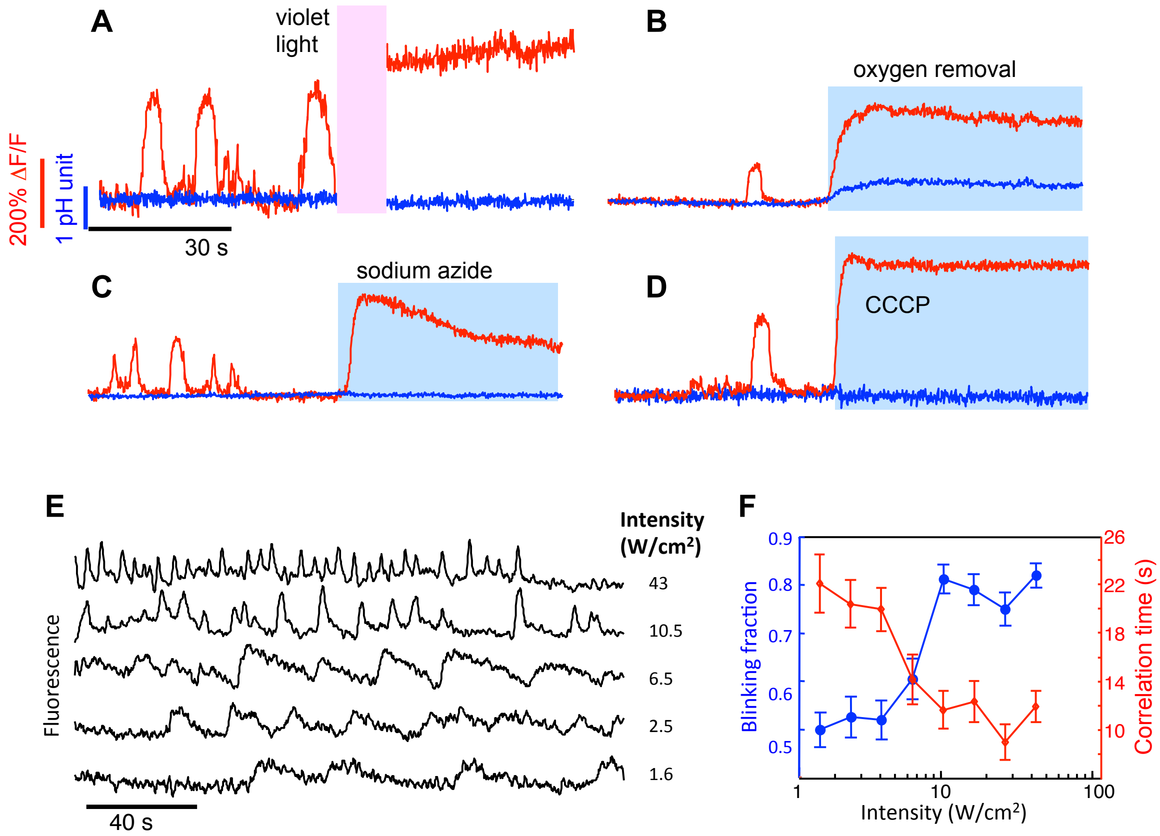

Figure 2.3: Single-cell responses to metabolic perturbations. Fluorescence of pHluorin and PROPS were recorded simultaneously to indicate responses of pH_i and V_m, respectively. (**A**) Violet light (100 W/cm²). Leakage of the violet light into the pHluorin and PROPS channels prevented acquisition of data during the perturbation. (**B**) Removal of oxygen. (**C**) Sodium azide (10 mM). (**D**) CCCP (50 μg/ml). Scale bars in (**A**) apply to data in (**A**) to (**D**). Colored bars indicate duration of the perturbation. (**E**) Blinking of *E. coli* expressing PROPS as a function of illumination intensity. (**F**) Blinks became more prevalent (blue) and shorter (red) at higher illumination intensity. Error bars represent s.e.m. Between 114 and 211 cells were analyzed at each intensity.

whether blinking was associated with cationic efflux, another important mechanism of stress response.

We observed surprising dynamics of a cationic membrane-permeable dye, tetramethyl rhodamine methyl-ester (TMRM), in blinking *E. coli*. As expected for this Nernstian voltage indicator [98], TMRM gradually accumulated in the cytoplasm over ~10 min. However, blinks in PROPS fluorescence coincided with precipitous stepwise drops in TMRM fluorescence that showed little or no recovery after the blink (**Fig. 2.4A**). The duration of the step in TMRM fluorescence coincided with the duration of the blink: At moderate intensities of red illumination (I = 10 W/cm^2) steps lasted less than 200 ms, whereas under little or no red illumination steps typically lasted several seconds (**Supplementary Fig. 2.22**).

Stepwise disappearance of TMRM was also observed in cells without the PROPS plasmid, when only dim green illumination was used to image the TMRM (30 mW/cm^2; **Fig. 2.4B** and **Supplementary Fig. 2.23**). The duration of these steps was comparable to that of steps in cells with PROPS under dim red illumination (2 W/cm^2). The rapid disappearance of TMRM during a blink suggested an active-transport mechanism. Dissipation of V_m lowers the thermodynamic barrier to cationic efflux (**Fig. 2.4C**, **Methods Section 2.4**). A concurrent dissipation of V_m and increase in membrane permeability would be sufficient to induce cationic efflux. PMF-dependent efflux of other cationic dyes has been observed in *E. coli* [16] in population-level assays that are insensitive to the dynamics of individual cells.

2.3 Discussion

Bacterial electrophysiology is likely to differ in several key regards from its eukaryotic version due to the comparatively small surface area, yet high surface-to-volume ratio found in bacteria. With a typical membrane capacitance between 10^{14} and 10^{13} F, a single ion channel with a conductivity of 100 pS can alter the membrane potential with a time constant of 10^3 to 10^4 s. In contrast, neurons only fire through the concerted action of a large number of ion channels. Thus, bacterial electrophysiology is likely to be dominated by stochastic opening of individual ion channels and pores. Additionally, the ionic composition of bacteria is

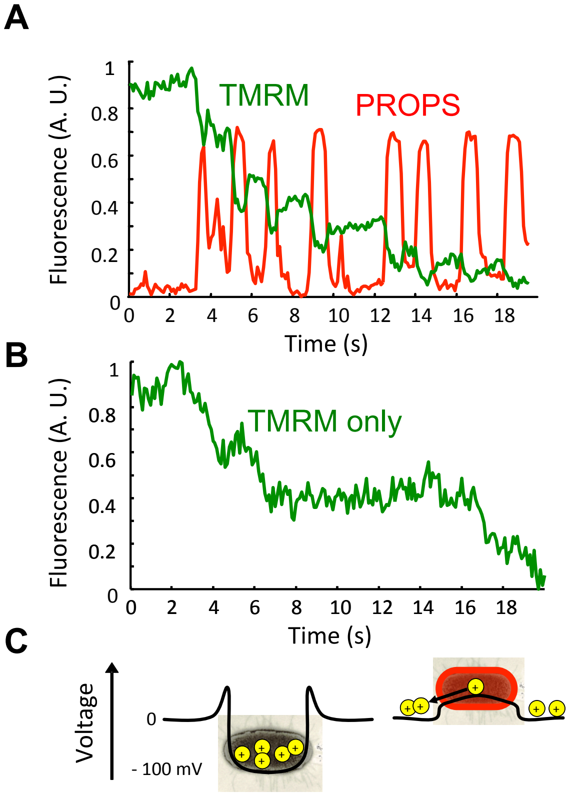

Figure 2.4: Blinks are accompanied by efflux of a cationic dye. (**A**) Simultaneous measurement of fluorescence from PROPS and TMRM. Blinks in PROPS (red) coincided with sudden drops in concentration of TMRM (green). (**B**) Cells not expressing PROPS showed stepwise efflux of TMRM, suggesting that electrical spiking occurred in the absence of PROPS. (**C**) Model for voltage-regulated cationic efflux. The resting potential of −80 to −120 mV is necessary for metabolism, but opposes cationic efflux. Transient depolarization lowers the barrier to efflux.

less robust than that of eukaryotes. A bacterium with a volume of 1 fl and a cytoplasmic Na^+ concentration of 10 mM contains only ~10^7 ions of Na^+. A single ion channel passing a current of 2 pA can deplete this store in less than 1 s. These simple estimates show that some of the tenets of neuronal electrophysiology may need rethinking in the context of bacteria.

2.4 METHODS

2.4.1 CONSTRUCTION OF PROPS AND PHLUORIN

Green absorbing proteorhodopsin strain EBAC31A08 [12] (GenBank AF279106) was used in a pBAD TOPO plasmid for arabinose induction or in a pACYC184 plasmid for IPTG induction. The D97N mutant was made using the QuikChange II kit (Stratagene) with the primers 5'-CGT CCC CCG GTA CAT CAA CTG GAT TCT CAC AAC-3' and the reverse complement 5'-GTT GTG AGA ATC CAG TTG ATG TAC CGG GGG ACG-3' (Integrated DNA Technologies). Mutants were checked by sequencing (Genewiz).

A plasmid containing super-ecliptic pHluorin [111] (GenBank AY533296) was a kind gift of Gero Meissenbock. The gene was cloned into a pCDF-Duet vector (Novagen) using forward BamH1 and reverse NotI restriction sites. Proper insertion of the gene was checked by sequencing. For dual expression of PROPS and pHluorin, the pACYC184 plasmid with GPR D97N and the pCDF-Duet plasmid were serially transduced into *E. coli* strain BL21.

A fusion of PROPS and the fluorescent GFP homolog Venus [115] was created by PCR sewing the fluorescent protein into the pBAD vector. The proper insertion of Venus was checked by sequencing. The fusion construct was transfected into strain BW25113.

2.4.2 *E. COLI* GROWTH

PROPS was expressed in five strains of *E. coli* (**Supplementary Table 2.1**). Cells were grown to early-log phase (OD600 = 0.3 – 0.4) in 50 mL of LB medium in a shaking incubator at 33 ° C. Inducer was added along with all-trans retinal (5 μM from a 20 mM stock in ethanol) and further growth was conducted in the dark. Cells were harvested after 3.5 hours and washed with 30 mL of minimal medium (1x M9 salts, 0.4% glucose, pH 7). Cells were resuspended in 5 mL minimal medium and used immediately or stored at 4 ° C for up to two weeks. All experiments were performed at room temperature, except for monitoring growth on an agarose pad which was performed at 35 ° C.

2.4.3 Protein purification

PROPS was expressed in E. coli and purified, following Ref. [14]. Briefly, cells (strain UT5600, pBAD TOPO plasmid) were grown in 1 L of LB with 100 μg/mL ampicillin, to an OD600 of 0.4 at 37 ° C. All-trans retinal (5 μM) and inducer (arabinose 0.02%) were added and cells were grown for a further 3 hours. Cells were harvested by centrifugation and resuspended in 50 mM Tris, 2 mM $MgCl_2$ at pH 7 and lysed with a tip sonicator for 5 minutes. The lysate was centrifuged and the pellet was resuspended in PBS supplemented with 1.5% octyl glucoside (OG). The mixture was homogenized with a glass/teflon Potter Elvehjem homogenizer and centrifuged again. The sample was passed through a Ni-agarose column (Qiagen) for purification, and bound protein was eluted with 400 mM imidazole. The imidazole was removed by dialysis against a solution of 1% OG in PBS.

Super-ecliptic pHluorin was expressed with a HIS tag and purified following standard procedures.

2.4.4 Purification of inner membrane

Inner membranes were purified following a modification of the protocol of Ref. [134]. *E. coli* strain BW25113 was grown as in **Supplementary Table 2.2**. 5 mL of cultured cells were harvested by centrifugation and resuspended in a chilled solution of 20% (weight:weight) sucrose in buffer of 500 mM potassium phosphate, 5 mM magnesium sulfate, and 1 mM phenylmethylsulfonyl fluoride (PMSF), pH 7.5. The suspension was passed through a French press at 8000 psi. The resulting solution was centrifuged for 10 min. at 3000 g. Cell membranes remained in the supernatant and were collected. Next, 20% sucrose in buffer described above (without PMSF), was added to bring the solution to 7 mL. A polyallomer centrifuge tube (Beckman Coulter) was filled sequentially with 1 mL 65% (w:w) sucrose in buffer, 4 mL 40% (w:w) sucrose in buffer, and the 7 mL of 20% sucrose solution with cell membranes. Tubes were spun in an ultracentrifuge with a SW41 rotor at 39,000 RPM for 16 hours at 4 ° C. Inner membranes segregated to the interface between the 20% and 40% sucrose solutions, while the outer membrane collected between the 40% and 65% sucrose solutions. We observed that the inner membranes remained pink while the outer membranes did not, implying that PROPS localized to the inner membrane.

2.4.5 Spectroscopic measurements

Absorption spectra of purified GPR WT and PROPS were recorded on a QE65000 spectrometer (Ocean Optics) equipped with a white-light LED illuminator. Fluorescence excitation and emission spectra were recorded on a Cary Eclipse fluorimeter (Varian) on purified PROPS solubilized in 1% octyl glucoside.

The quantum yield (QY) was calculated by comparison of the absorption and emission spectra of PROPS to corresponding spectra of Alexa 647 (112 pM in PBS, Molecular Probes). The QY of PROPS was calculated by

$$QY_{PROPS} = \frac{em_{props}}{em_{AF647}} \frac{abs_{AF647}}{abs_{PROPS}} QY_{AF647}$$

where *abs* is the absorbance of the sample at 633 nm and *em* is the integrated fluorescence emission over the range 650 nm – 750 nm for both species. The quantum yield of Alexa 647 is 0.33. The quantum yield obtained by this procedure was 1.0×10^{-3}.

To determine pH-dependent fluorescence, the pH of the PROPS solution was changed with NaOH and measured using a microtip pH meter.

2.4.6 Fluorescence imaging

Cells were imaged in a home-built inverted fluorescence microscope equipped with a dual-view emission pathway. Illumination was provided either in *trans* or *epi*. The light sources used in the experiments are given in **Supplementary Table 2.3**. The microscope was equipped with a high numerical aperture (N.A. 1.45) 60 x oil-immersion objective (Olympus), enabling through-the-objective total internal reflection fluorescence (TIRF) imaging. The cameras were frame-transfer EMCCDs (Andor iXon+) with either 512 x 512 pixels (for imaging a large field of view) or

128 x 128 pixels (for high-speed imaging).

For imaging of PROPS fluorescence alone, the 633 nm HeNe was used for excitation, and a Cy5 filter set (λ_{exc} = 633 nm, λ_{em} = 660-760 nm) was used to separate emission from excitation. Blinking was typically observed with an electron-multiplying gain of 300 and an exposure of 100 ms.

For simultaneous imaging of a fluorophore and PROPS, light from either the 532 nm laser, the 488 nm laser, or the supercontinuum source was combined with the 633 nm excitation using a 590 DCXR dichroic mirror (Chroma). A multi-band dichroic (Semrock Di01- R405/488/561/635) was used in the microscope to separate emission from excitation. Alternatively, in some cases the combined laser beams were brought in the *trans* configuration, in which case no dichroic mirror was used.

A two-color imaging system was constructed to image two fluorophores simultaneously on one camera. A variable slit (ThorLabs) was placed in the image plane to select a rectangular region of the image with an aspect ratio of approximately 2:1. A dichroic mirror (640 DCXR Chroma) separated the fluorescence into a long-wavelength path and a short-wavelength path. A 710/100 emission filter (Chroma) selected the emission from PROPS in the long-wavelength path, and a 580/60 filter selected the emission from pHluorin or TMRM in the short wavelength path. The beams were recombined on a second 640 DCXR dichroic mirror and imaged onto the EMCCD camera. For single color imaging, the variable slit was removed and one emission path blocked.

Through-the-objective TIRF imaging was used to observe TMRM because out of focus dye would otherwise overwhelm the signal from dye taken up by the *E. coli*.

2.4.7 PHOTOBLEACHING OF PROPS AND VENUS

To compare the photostability of PROPS and Venus, we recorded photobleaching traces of both, in a PROPS-Venus fusion. By measuring photobleaching on the fusion protein, and for both fluorochromes in the same sample, we ensured that an equal number of molecules of PROPS and Venus contributed to their respective signals. This 1:1 stoichiometry facilitated calculation of the relative number of photons emitted prior to photobleaching.

E. coli expressing the PROPS-Venus fusion were treated with CCCP to set $V_m = 0$ and $pH_i = pH_o$. Cells were adhered to a glass coverslip pre-treated with poly-L-lysine and imaged in minimal medium at pH 7.5.

Photobleaching of PROPS and Venus were measured sequentially on the same sample under wide-field laser illumination. PROPS was excited at $\lambda_{exc} = 633$ nm, with emission collected through a 710/100 nm bandpass filter. Venus was excited at $\lambda_{exc} = 488$ nm, with emission collected through a 550/50 nm bandpass filter. The laser powers were adjusted so that the initial fluorescence intensities were approximately equal for PROPS and Venus. For both fluorochromes, a background signal from a cell-free region of the sample was subtracted from the raw intensity. Intensities were then corrected for the wavelength-dependent quantum yield of the EMCCD and the overlap between the emission spectrum of the fluorochrome and the transmission spectrum of the corresponding band pass filter. The photobleaching decays were fit to a single exponential, and the relative areas under the fits for the two fluorochromes determined the relative number of total photons prior to photobleaching.

2.4.8 Estimate of the number of molecules of PROPS per cell

We determined the average number of molecules of PROPS per cell by measuring the amount of retinal required to saturate the binding. Free and bound retinal were spectroscopically distinguishable by their visible absorption maxima, at 380 and 555 nm, respectively. At low retinal concentrations, most added retinal was taken up by PROPS. Once the PROPS was saturated, additional retinal remained free. Addition of retinal drove the reaction:

$$Ret + Ops \rightleftharpoons PROPS$$

with equilibrium constant K_{eq}. In this scheme Ops is the microbial opsin without retinal, and PROPS is the assembled complex. The spectroscopically measureable concentrations were [Ret] and [PROPS]. The amount of retinal added was $[R^{(0)}] = [Ret] + [PROPS]$. Our goal was to determine $[P^{(0)}] = [Ops] + [PROPS]$.

50 mL culture of *E. coli* strain BW25113 was grown to OD600 0.4 and induced with 0.0005% arabinose, following the usual procedure for preparing cells for imaging. After 3.5 hours the cells were split into 20 aliquots of 1 mL, and to each

was added a known quantity of retinal. The retinal concentrations varied from zero to 45 μM. The cells were incubated with retinal overnight at 4° C.

Visible absorption measurements were taken on whole cells using a QE65000 spectrometer (Ocean optics). Cells expressing protein but without retinal were used as a reference to correct for scattering. A white LED (LuxeonV) provided illumination. Analysis was performed in Matlab.

Absorption spectra had two peaks, corresponding to free retinal (λ_{max} = 380 nm) and retinal bound to PROPS (λ_{max} = 555 nm). Singular Value Decomposition (SVD) [146] was applied to identify the spectral components that co-varied with retinal concentration. The two principal spectra returned by SVD appeared to be linear combinations of the spectra of free and bound retinal, so we generated two new basis functions by taking linear combinations that matched spectra of free and bound retinal. A projection of the measured spectrum onto these reference spectra was then performed at each retinal concentration to determine the concentrations of the free and bound retinal.

The concentrations of the measureable species are given by:

$$[PROPS] = \frac{1 + K_{eq}([P^{(0)}] + [R^{(0)}]) - \sqrt{-4[P^{(0)}][R^{(0)}]K_{eq}^{2} + (1 + K_{eq}([P^{(0)}] + [R^{(0)}]))^{2}}}{2K_{eq}}$$

and

$$[Ret] = \frac{-1 + K_{eq}([R^{(0)}] - [P^{(0)}]) + \sqrt{-4[P^{(0)}][R^{(0)}]K_{eq}^{2} + (1 + K_{eq}([P^{(0)}] + [R^{(0)}]))^{2}}}{2K_{eq}}$$

The ratio [Ret]/[PROPS] was fit as a function of $[R^{(0)}]$ yielding values $K_{eq} = 0.5\ \mu M^{-1}$ and $[P^{(0)}] = 5.5\ \mu M$ (**Methods Fig. 2.5**). A cell count on a hemocytometer yielded a density of 1.2×10^{11} cells/mL, whereupon we calculated 28,000 molecules of PROPS per cell.

2.4.9 Effect of PROPS expression on cell growth

E. coli strain BW25113 was grown in a 50 mL culture in a shaker at 33° C to OD600 of 0.4 (5 hrs.). The cells were then divided into four 50 mL samples which were exposed to different inducer concentrations and 5 μM retinal. The cells

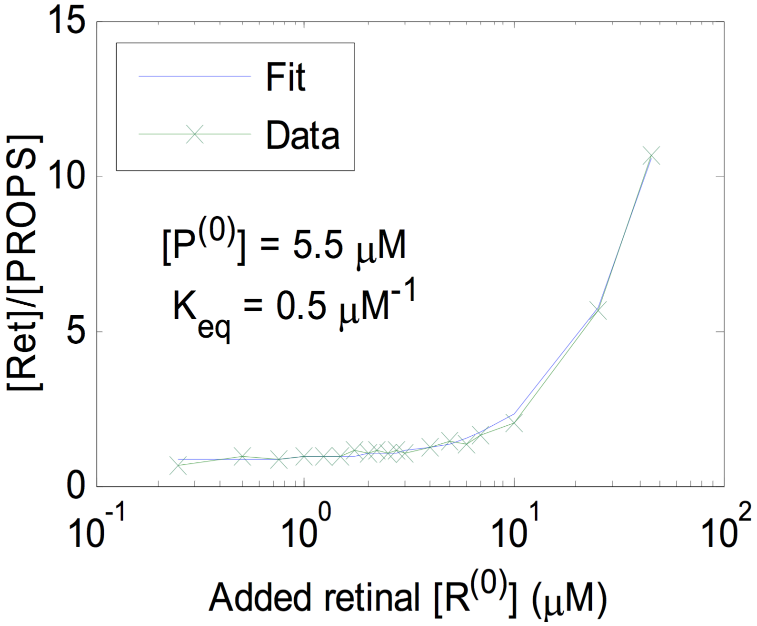

Figure 2.5: Titration of the quantity of PROPS in an E. coli by its ability to bind retinal.

were incubated with agitation in the dark for a further five hours. An inducer concentration of 0.0005% arabinose had minimal effect on the growth (**Methods Fig. 2.6**), so this concentration was chosen for further experiments with strain BW25113. Other strains and plasmids required separate determinations of the maximum inducer concentration at which the cells remained healthy.

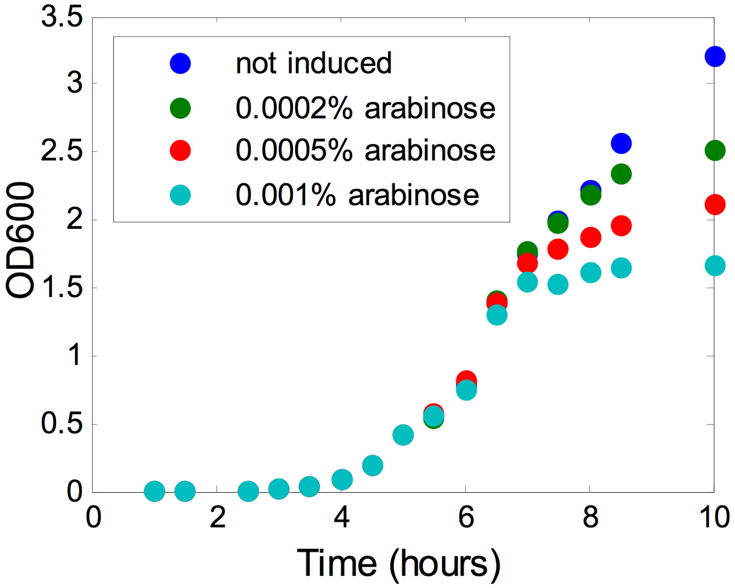

Figure 2.6: Growth of E. coli strain BW25113 as a function of inducer concentration.

2.4.10 ATTEMPTS TO CALIBRATE VOLTAGE RESPONSE OF PROPS

1) Eukaryotic expression. A large number of attempts were made to express PROPS in the plasma membrane of eukaryotic cells, following the protocols of Gradinaru and coworkers [46], as well as other strategies. Efforts included human codon optimization, addition of signaling sequences, golgi and endoplasmic reticulum export sequences, domain swaps with other microbial rhodopsins having good membrane targeting, variation of protein expression temperature and time, and transfection of multiple cell lines (**Supplementary Tables 2.4 and 2.5**).

All attempts resulted in protein expression localized to the internal membranes of the endoplasmic reticulum (ER), the golgi, or vesicles. No protein was detected in the plasma membrane.

2) Droplet hydrogel bilayers. We attempted to incorporate PROPS into artificial lipid bilayers for the purpose of imaging voltage-dependent fluorescence. Droplet hydrogel bilayers (DHBs) were formed at the interface of a thin agarose pad and a millimeter-scale aqueous droplet immersed in a lipid/oil emulsion. We constructed a custom-machined acrylic sample chamber for the DHB experiments, following Ref. [59]. We formed stable DHBs from 1,2-diphytanoyl-sn-glycero-3-phosphocholine (DPhPC), but addition of vesicles comprised of PROPS/DPhPC did not result in PROPS incorporation into the DHB. Addition of small amounts of dodecylmaltoside (0.001-0.005%) to facilitate protein insertion [63] resulted in unstable bilayers.

3) Xenopus oocytes. GPR has previously been expressed in xenopus oocytes [40], a model system for electrophysiological studies on membrane proteins. We found that oocytes had intense autofluorescence when illuminated at 633 nm, so we did not attempt protein expression.

4) Patch clamp measurements on *E. coli* spheroplasts Delcour and coworkers reported patch clamp studies of *E. coli* spheroplast membranes [32]. We formed spheroplasts following literature protocols [106], but found that the patch clamp protocol was incompatible with fluorescence imaging because the membranes were largely sucked into the pipette as soon as suction was applied.

2.4.11 INDUCED TRANSMEMBRANE VOLTAGE (ITV)

Cells were immobilized on a poly-L-lysine-coated glass coverslip and washed with copious deionized water. The coverslip was mounted in an inverted fluorescence microscope. Two steel electrodes (7 mm long, 0.5 mm diameter, separated by 1.6 mm) were mounted on a micromanipulator and positioned on opposite sides of the field of view (**Methods Fig. 2.7**). Voltage pulses from a high voltage amplifier (Trek 2205) were applied to the cells, following the waveform shown below. Pulses alternated polarity to minimize formation of electrochemical byproducts and polarization of the solution. A typical waveform had 1 pulse/s, each pulse lasting 200 ms, and pulse amplitudes ranging from 50 V to 400 V. At the maximum voltage of 400 V, the current was approximately 10 mA. Cells were washed with DI water after every experiment to prevent buildup of electrochemical biproducts.

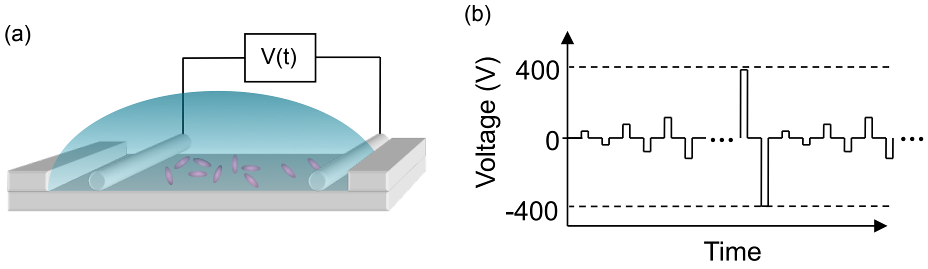

Figure 2.7: Induced transmembrane voltages applied to *E. coli*. (**a**) Experimental setup (not to scale). (**b**) Time-course of voltage pulses. This waveform probed both the fluorescence as a function of voltage, and the dynamic step-response.

In each experiment, a cell whose long axis was parallel to the electric field was selected for analysis. The magnitude of the ITV was proportional to the length of the cell, so usually an elongated cell was selected. To maximize frame rate, we used an Andor iXon$^+$ DU-897 camera with a small region of interest (ROI). The camera was externally clocked to synchronize image acquisition with the voltage pulses. Typical exposure times were 0.5 ms. **Methods Fig. 2.8** shows the average changes in fluorescence of a single cell as a function of the ITV.

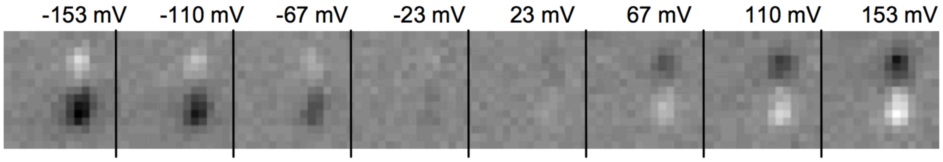

Figure 2.8: Average deviations in fluorescence as a function of induced membrane voltage in a single *E. coli*. Each image is an average over 10 voltage pulses. $\lambda_{exc} = 633$ nm.

We modeled the cell as a conducting prolate spheroid covered with a thin, perfectly insulating membrane. The Schwan equation gives the membrane potential for a spherical cell, and Kotnik and Miklavcic generalized the treatment to include spheroidal cells [86]. They showed that the ITV is given by:

$$V(\phi) = E\frac{(R_1^2 - R_2^2)}{R_1 - \frac{R_2^2}{\sqrt{R_1^2-R_2^2}}\ln\left(\frac{R_1+\sqrt{R_1^2-R_2^2}}{R_2}\right)} \times \frac{R_2\cos\phi}{\sqrt{R_1^2\sin\phi^2 + R_2^2\cos\phi^2}}$$

where E is the electric field strength and the geometrical parameters are defined in **Methods Fig. 2.9**.

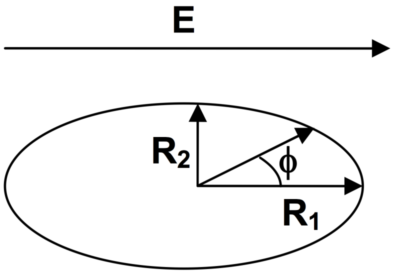

Figure 2.9: Model of an *E. coli* with its long axis parallel to an electric field.

For a spherical particle ($R_2 = R_1$) the ITV at each pole is $V_{sphere} = \frac{3}{2}ER$. In the limit as the cell becomes long and thin ($R_2/R_1 \rightarrow 0$), the ITV at each pole approaches $V_{line} = ER_1$. We usually picked cells with $R_1 > 5R_2$, in which case the long and thin approximation is adequate.

Calibration of the ITV signal. Direct application of the modified Schwan equation neglects possible voltage drops across the cell wall or outer membrane. To calibrate the ITV procedure we sought a different fluorescent indicator that functioned in **E. coli** and that had a known voltage response. We recently identified a mutant of Archaerhodopsin 3 (Arch) with voltage-indicating properties similar to those of PROPS, but with good membrane targeting in eukaryotic cells [88]. We calibrated the Arch-based sensor by direct patch clamp measurements in HEK293 cells. Upon expression in *E. coli*, this protein also showed blinking behavior. ITV-induced changes in fluorescence of the Arch-based indicator formed the basis of the calibration.

These measurements indicated that the modified Schwan equation overestimated the voltage drop across the inner membrane by a factor of 3.1, so calculated values were adjusted accordingly. The calibration indicated that under ITV conditions the *E. coli* had a resting membrane potential of V_0 ~ -50 mV. The voltage applied in ITV only induced changes in membrane potential, so the calibration of V_0 was used to position the voltage axis in **Fig. 2.1C**. The discrepancy between our measured V_0 and the literature value of -80 to -120 mV is likely due to the fact that ITV experiments were performed on cells that had been sitting for several minutes in deionized water. All other experiments were performed in minimal medium. Percentage change in fluorescence values (ΔF/F) were calculated as described below in **Methods Section 2.4.16**.

Control experiments in which we imaged fluorescence of Venus in the PROPS-Venus fusion confirmed that the changes in PROPS fluorescence were not due to voltage-induced motion of the entire cell. The Venus fluorescence showed a small ITV signal of opposite sign to the PROPS signal, but at present it is unclear whether this transient was due to changes in local proton activity (Venus shows pH-sensitive fluorescence) or due to changes in nonradiative energy transfer between Venus and the retinal in PROPS.

2.4.12 CALIBRATION OF SUPER-ECLIPTIC PHLUORIN IN *E. COLI*

Fluorescence excitation spectra were acquired on a bulk solution of pHluorin as a function of pH. **Methods Fig. 2.10** shows the bulk fluorescence under excitation at 488 nm and emission at 509 nm. This excitation wavelength was chosen to match the wavelength used later in microscopic imaging experiments.

PROPS and pHluorin were then co-expressed in *E. coli* strain BW25113. The cells were adhered to a coverslip with poly-L-lysine, and washed with CCCP to equalize pH_i and pH_o. The average fluorescence in the PROPS and pHluorin channels (with simultaneous excitation at 488 and 633 nm) was recorded as a function of pH. The pK_a of pHluorin reported *in vivo* was 7.4 while in bulk it was 7.2. The similarity of the titrations *in vivo* and in bulk confirmed that CCCP set pH_i = pH_o. We ascribe the slight difference in pK_a values to imperfect control of the pH in the small sample volumes used in the microscope. This pH error sets the accuracy of single-cell measurements of pH_i to 0.2 pH units. The pH-dependent fluorescence of PROPS showed a broad response, possibly indicative of multiple

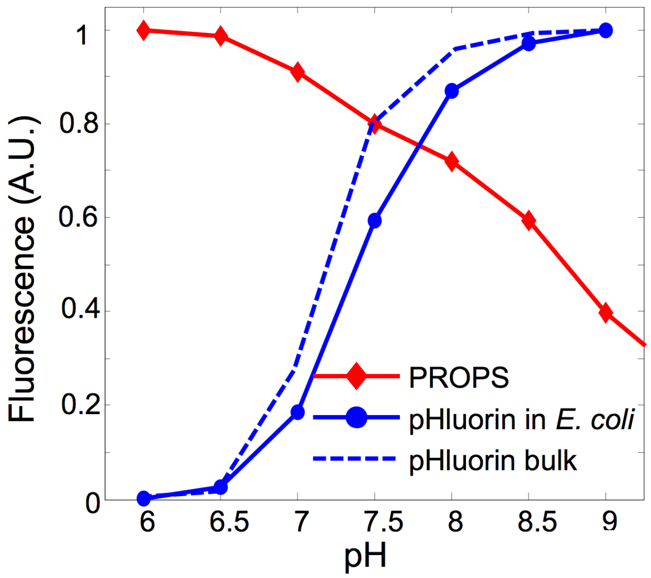

Figure 2.10: Fluorescence of PROPS and super-ecliptic pHluorin in *E. coli*. Cells were made permeable to protons by treatment with CCCP.

titratable groups that influenced the fluorescence of the protein.

The precision of single-cell measurements of pH_i was determined by comparing the noise in the pHluorin intensity under nominally constant pH, to the change in pHluorin intensity due to a step from pH 8 to 9. This procedure yielded a shot-noise limited precision of 0.02 pH units/(Hz)$^{1/2}$.

The response speed of pHluorin to pH steps was determined by rapidly exchanging the buffer around CCCP-treated cells. **Fig. 2.2B** in the main text shows that this response occurred in < 1 s (limited by the speed of buffer exchange). This result implies that pHluorin responds to changes in local pH faster than 1 s, and that pH changes propagate through the cytoplasm of *E. coli* faster than 1 s. Thus, if blinks in PROPS were accompanied by changes in pH_i of greater than 0.02 pH units, the pHluorin would have indicated these changes.

2.4.13 FLAGELLAR ROTATION ASSAY

A sample of *E. coli* strain JY29 Δ*cheY* was transformed with PROPS and grown as described in **Supplementary Table 2.2**. To shorten the flagella, the cells were sheared approximately 20 times by passage through a 27 gauge needle. Sheared cells were allowed to settle on a clean glass coverslip for several minutes. Some cells attached by a single flagellum and rotated in a circle. Fluorescence movies were acquired which showed simultaneously the rotation and blinking.

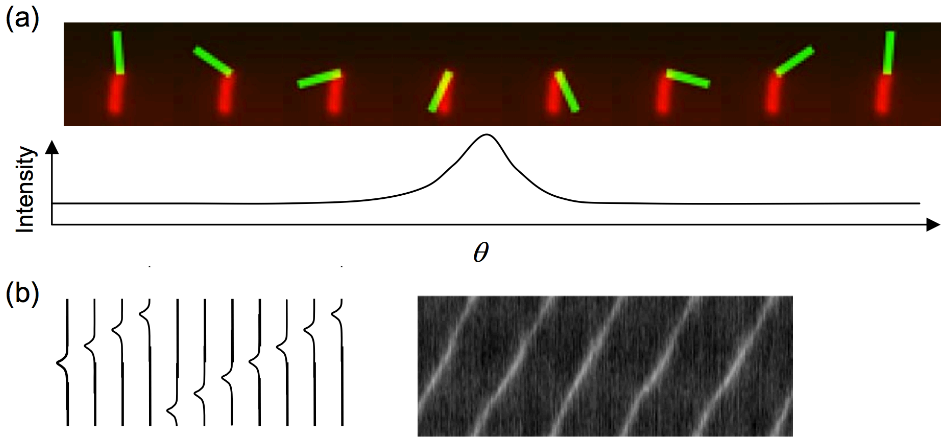

Figure 2.11: Procedure for constructing a rotary kymogram. (**a**) For each frame of the movie, the image of the cell (red) is overlapped with a rotating mask (green). The intensity underneath the mask at each rotation angle indicates the angular intensity distribution. (**b**) Successive intensity distributions are stacked adjacent to each other to create a kymograph which shows intensity of PROPS fluorescence by its brightness, and the angular velocity of the cell by its slope.

Movies were analyzed by constructing "rotary kymographs". For each cell, the center of rotation was identified by examination of an image of time-averaged fluorescence: rotating cells appeared as disks. For each frame, k, we then calculated the angular dependence $I(\theta)$ of the fluorescence brightness within one cell-length of the center of rotation (see **Methods Fig. 2.11**). Stacking all of these plots adjacent to each other led to the rotary kymograph, $I(\theta,k)$. Diagonal lines represent rotation at constant angular velocity, with higher slope corresponding to higher angular velocity. The brightness of the diagonal lines indicates the brightness of the cell. In this way it is simple to observe whether blinks coincide with pauses.

2.4.14 VOLTAGE-SENSITIVE DYES

We tested two classes of voltage-sensitive dyes: membrane-localized dyes whose brightness was directly modulated by membrane potential, and Nernstian dyes that accumulated in the cell in a potential-dependent manner. **Supplementary Table 2.6** lists the dyes that we tested. For Di-4-ANEPPS and Di-8-ANEPPS, cells were pre-incubated with the dye at a concentration between 0.5 and 2 μM in minimal medium, pH 7.5. Cells were then allowed to settle on a coverslip coated with poly-L-lysine, or were immobilized at the interface of an agarose pad and a coverslip. Simultaneous two-color movies of blinking and dye fluorescence were acquired.

The outer membrane of *E. coli* presents a barrier to entry of many small molecules, creating a challenge for loading fluorescent indicators. To increase the permeability of the membrane, we treated the cells with the chelator ethylenediaminetetraacetic acid (EDTA), following the procedure of Lo and coworkers [97]. Neither pre-treatment with EDTA, nor flowing dye solution over the cells during imaging, led to an increase in the fraction of cells that took up Di-4-ANEPPS or Di-8-ANEPPS.

To load cells with TMRM, the cells were incubated in 1 mM EDTA at 37° C for 1 min. The cells were then washed and immobilized on an agarose pad and sealed in place with a coverslip. 1 μL of a solution of TMRM (200 μM) was added to a hole in the glass slide on top of the agarose pad. After several seconds the cells became fluorescent under excitation at 532 or 633 nm. Efflux of TMRM during blinks precluded using this dye as an indicator of membrane potential.

2.4.15 SAMPLE CHAMBERS AND CHEMICAL PERTURBATIONS

E. coli cells were immobilized and imaged using one of three techniques: (1) poly-L-lysine (PLL) coated coverslips, (2) agarose pads, or (3) sticky flagella immobilization.

1) Immobilization on PLL. A well of approximately 5 x 10 mm area and 0.7 mm depth was formed on a coverslip by using piece of polydimethyl siloxane (PDMS) sheet. Approximately 5 μL of a solution of 0.01% PLL (Sigma P4707) in water was loaded into the well and allowed to evaporate to dryness. Cells suspended in minimal medium were added to the well and allowed to incubate for 2 min. The well was then washed with copious minimal medium to remove non-adhered cells. A glass slide containing holes for fluid inlet and outlet was reversibly sealed to the top of the PDMS sheet to create an enclosed flow cell (**Methods Fig. 2.12**).

2) Immobilization on an agarose pad. A mold was constructed by affixing a PDMS sheet of thickness 0.7 mm to a glass slide. The PDMS had a cutout of 10 x 10 mm, which was filled with a molten solution of 1.5% agarose in minimal medium. A second microscope slide was placed on top of the mold to form a flat top surface of the agarose. After the agarose gelled, one slide was removed and 0.7 μL of a suspension of *E. coli* was placed on the pad. As soon as the excess liquid had been absorbed by the agarose, a coverslip was placed on the pad to seal the cells at the agarose-coverslip interface. The remaining microscope slide was replaced with a slide with a small hole in the center, to allow addition of TMRM and diffusion of oxygen to the cells.

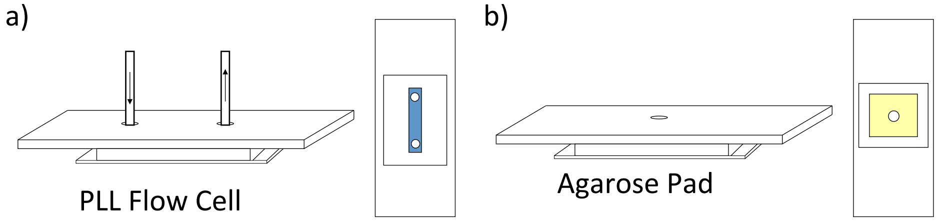

Figure 2.12: Sample chambers used for imaging. (**a**) The PLL flow cell allowed rapid exchange of buffer, but some cells retained residual freedom of movement. (**b**) Immobilization under an agarose pad avoided possible spurious effects from the PLL, but only allowed a single addition of a test chemical through the hole in the top slide.

3) Immobilization via adhesion of flagella. A suspension of sheared *E. coli* strain JY29 expressing PROPS were was placed in a PDMS well on a clean coverslip and allowed to settle for 10 minutes. The well was then sealed with a glass slide containing inlet and outlet ports. The cells were bathed in a gentle flow of minimal medium, but the flow was stopped during data collection to avoid perturbations to the rotation.

Chemical perturbations were applied by using a syringe pump to change the buffer above the *E. coli*. Flow rates were typically 200 μL/min. We estimate the time for buffer exchange was ~10 s. Unless indicated all buffers were adjusted to maintain constant pH during a perturbation. Oxygen removal was accomplished with Oxyrase (Oxyrase, Inc.) following manufacturer instructions. Oxygen was reintroduced by flowing freshly aerated buffer.

2.4.16 IMAGE PROCESSING

All data were analyzed in Matlab (R2009, Mathworks) using custom image processing scripts.

We used covariance-based techniques to automatically identify blinking cells. A simple approach to finding blinkers is to calculate the variance in the fluorescence at each pixel: more variable pixels correspond to blinkers. However, this approach is contaminated by the Poisson- distributed shot noise from bright but non-blinking pixels, which contributes a variance proportional to the intensity. We instead calculated the covariance of the intensity in each pixel with the intensity of its neighboring pixels in space (1 pixel over), and time (1 frame later). The shot noise is uncorrelated between frames and pixels, so this approach is immune to constant background fluorescence. **Methods Fig. 2.13** shows the result of such a calculation, in which the covariance-based measure of blinkiness is displayed in green, and the average brightness is displayed in red. Cells whose covariance intensity exceeded a threshold were deemed to have blinked.

Cells were identified by an automated segmentation algorithm, supplemented by manual scission of closely spaced cells that were marked as one, and manual removal of debris misidentified as a cell. The algorithm could be run either on the covariance image which showed only blinking cells, or on all cells.

Intensity traces were extracted for each cell, with all pixels inside the cell weighted equally. A background intensity trace was calculated from an annulus of pixels surrounding each cell. In cases where cells were immediately adjacent, a partial annulus that did not overlap the adjacent cell was used to calculate background. Fractional changers in fluorescence, ΔF/F, were calculated on the background-subtracted intensity traces, with F taken to represent the baseline

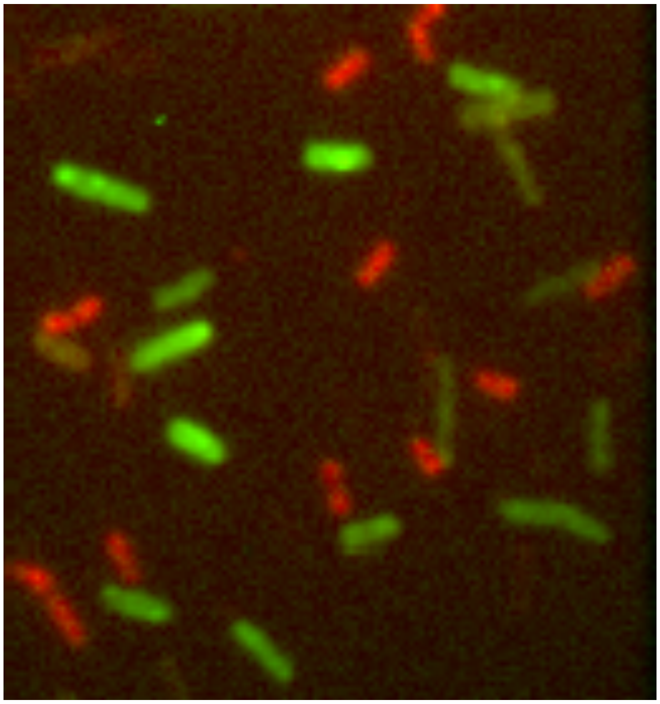

Figure 2.13: Covariance-based identification of blinking cells. The time-average fluorescence is in red, and the pixel-wise nearest-neighbor covariance is in green. Green cells blinked.

(dark state) fluorescence.

Single-cell intensity traces were analyzed for blink amplitude, duration, and inter-blink interval. This parsing was somewhat subjective because of the wide variety of blink dynamics. The duration of a blink was defined as the full width at half-maximum intensity. Rise times were defined as the time for the intensity to go from 20% to 80% of the maximum for that blink.

To analyze two-color data, images from the two halves of the EMCCD were overlaid. One image was subjected to translation, rotation, and a small change in magnification to maximize its overlap with the other image. Drift during long movies was removed by registering images to the first frame of the movie. In all cases, transformed images were generated by bicubic interpolation from the original. Images were also corrected for nonuniformities in the illumination spot. Reference images of the illumination spot were acquired for each color, and images were divided by this reference.

2.4.17 QUANTIFYING BLINKING AS A FUNCTION OF LASER POWER

We assayed blinkiness by counting the fraction of cells that blinked at least once during a 200 s observation. The timescale of blinking was determined by fitting the autocorrelation of the fluorescence intensity to a single exponential decay.

2.5 SUPPLEMENTARY TEXT

2.5.1 DESIGN PRINCIPLES UNDERLYING PROPS

Here we present a simple model of the voltage sensitivity in PROPS. This model guided our design of PROPS, but it likely neglects many important features of the real protein.

The key idea is that protonation of a titratable group depends on both bulk pH and local electrostatic potential. The local electrostatic potential is partially determined by the membrane potential.

Supplementary Fig. 2.15 illustrates the physical picture. We assume that the titratable group is primarily coupled to the cytoplasm (based on data described below). The cytoplasm acts as a reservoir of protons at constant chemical potential, given by pH_i. The local electrochemical potential at the titratable group is

$$\mu_{H^+} = V_{loc} + 59mV \times pH_i$$

where V_{loc} is the local electrostatic potential, measured relative to the cytoplasm, and pH_i is the internal (cytoplasmic) pH. An increase in V_{loc} of 59 mV is equivalent to an increase in pH of 1 unit at room temperature. The titratable group reaches thermal equilibrium by exchanging a proton with the cytoplasm. Thus the pK_a of the titratable group is $pK_a = pK_a^{(0)} - V_{loc}/59$ mV , where $pK_a^{(0)}$ is the pK_a in the absence of a membrane potential.

Most of the voltage drop between the periplasm and the cytoplasm occurs in the double layers on either side of the membrane. These have a thickness given by the Debye length, approximately 0.7 nm. As shown in **Supplementary Fig. 2.15(B) and (C)**, V_{loc} is generally smaller in magnitude than V_m, though the constant of proportionality is unknown a priori (one can think of the protein as a voltage divider with the SB at an intermediate point). Thus one expects a change in membrane potential greater than 59 mV to be equivalent to a change in bulk pH of 1 unit. We measured a correspondence of 102 mV in V_m to 1 pH unit, consistent with the above model (**Fig. 2.1C**).

Alternatively, deviations from our simple model may contribute to deviations from ideal Nernstian behavior. Membrane potential is likely to affect protonation of many functional groups, some of which will be electrostatically coupled to the SB. These indirect coupling mechanisms could alter the voltage response of PROPS. Additionally, the membrane potential may induce conformational changes in the protein, which could alter the accessibility of the SB, and its local electrostatic potential. If the SB is coupled to both the cytoplasm and the periplasm, then a nonequilibrium Goldman-type treatment is needed to predict the protonation of the SB. Finally, functional groups other than the SB may play a role in determining fluorescence. Membrane potential is likely to regulate the charge state and position of these functional groups as well.

It is important to note that voltage-induced changes in protonation of the SB do not require proton transport across the membrane nor are they accompanied by detectable changes in cytoplasmic pH.

2.5.2 CYTOPLASMIC ACCESSIBILITY OF THE SB IN PROPS

Our observation that the fluorescence-determining group in PROPS is exposed to the cytoplasm is contrary to the conventional view that the SB in the ground state of microbial rhodopsins is exposed to the extracellular medium [58]. Our evidence for the cytoplasm-exposed fluorescence-determining group is:

1) In freshly grown **E. coli**, variation in pH_o causes almost no change in pH_i (reported via pHluorin fluorescence), nor in PROPS fluorescence. After treatment with CCCP, pHluorin fluorescence reports that $pH_o = pH_i$, and PROPS fluorescence becomes sensitive to pH. Thus PROPS fluorescence appears sensitive only to pH_i.

2) ITV experiments and metabolic perturbations both indicate that PROPS fluorescence is bright when the membrane is electrically depolarized, while PROPS is dark in the electrically polarized membrane. This sign of response is consistent with a cytoplasm-exposed titrable group.

There are several possible explanations for this discrepancy between our observations and published structural models.

1) The exposure of the SB in PROPS may be different from in the WT protein. Precedent for this hypothesis comes from molecular dynamics simulations of the bacteriorhodopsin mutant D85N—homologous to D97N in GPR—which found that the mutations switched the accessibility of the SB from the extracellular to the cytoplasmic side [68]. Also, experiments on the D75N mutant of sensory rhodopsin II—homologous to D97N in GPR—also showed a transient inward-directed photocurrent, consistent with a cytoplasm-exposed SB (Fig. 4 in Ref. [142]).

2) The membrane potential may induce a conformational switch which favors a cytoplasm-exposed SB. Most spectroscopic experiments on microbial rhodopsins are performed without control of the membrane potential, so the conformation in an energized cell may differ from the conformation in a film or in a de-energized vesicle.

3) The voltage sensitivity of PROPS may be determined by a group or groups other than the SB; or by voltage-induced conformational changes in the protein that do not involve shifts in the acid-base equilibrium of the SB.

4) The voltage-sensitive fluorescence of PROPS may be produced from an excited intermediate state in the GPR photocycle where GPR is in a conformation that exposes the SB to the cytoplasm.

Additional spectroscopic and computational work is needed to determine the ground-state conformation of GPR D97N (PROPS), and how membrane potential affects this conformation.

2.5.3 Limits on laser heating of *E. coli*

To determine whether heating contributed to the illumination-dependent blinking of E. coli we estimate the maximum temperature rise expected under our imaging conditions. The highest intensity used in our experiments was I = 100 W/cm^2. We approximate a bacterium as a sphere 2 μm in diameter. If we assume that the cell absorbed all of the laser light incident on it, then the power delivered to the cell was P = 3 μW. The temperature rise ΔT of a sphere in a homogeneous continuum is given by

$$\Delta T = \frac{P}{4\pi\sigma r}$$

where r is the radius of the sphere and σ is the thermal conductivity of the medium. For our model bacterium in water (σ = 0.58 W/m K), this estimate yields ΔT = 0.4° C.

2.6 SUPPLEMENTARY FIGURES

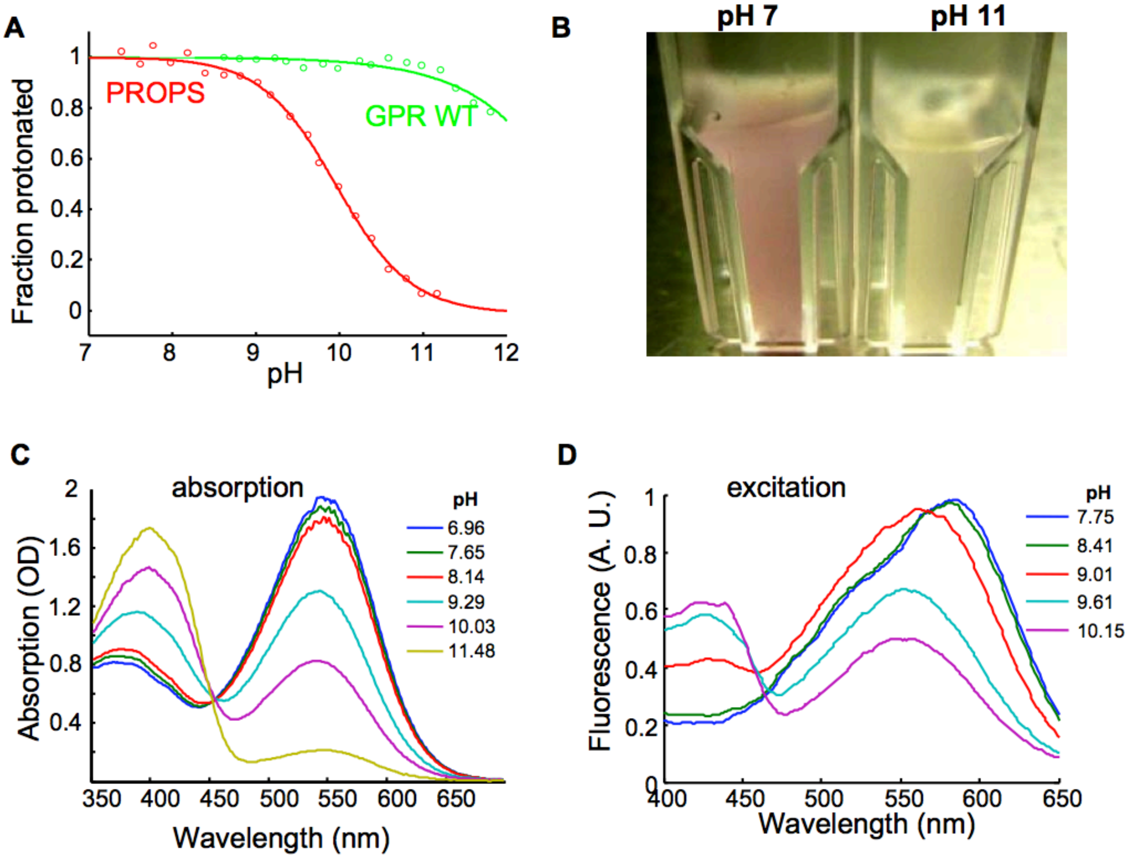

Figure 2.14: Photophysics of PROPS. (**A**) Titration of the Schiff Base (SB) in wild-type GPR and PROPS, as measured by visible absorption. We applied Singular Value Decomposition to a series of absorption spectra acquired at different pH values to determine the titration of the SB. In wild-type GPR, deprotonation of the SB occurred with a $\mathrm{p}K_a > 12$, consistent with earlier reports [71], while in PROPS the $\mathrm{p}K_a$ was 9.6. (**B**) The pH-induced color change in *E. coli* expressing PROPS was visible by eye. (**C**) pH-dependent absorption and (**D**) and fluorescence excitation spectra of PROPS. Both quantities showed a $\mathrm{p}K_a$ of 9.6, corresponding to protonation of the SB. The apparent shift in the excitation peak between pH 8.41 and 9.01 was an inner filter artifact: to acquire an excitation spectrum in reasonable time, the solution had to be so concentrated that it absorbed a significant portion of the incident light. Test measurements on more dilute solutions showed no shift in excitation spectrum between pH 8 and 9. The data in (**C**) and (**D**) imply that protonation of the SB modulated fluorescence by modulating the extinction coefficient at the excitation wavelength.

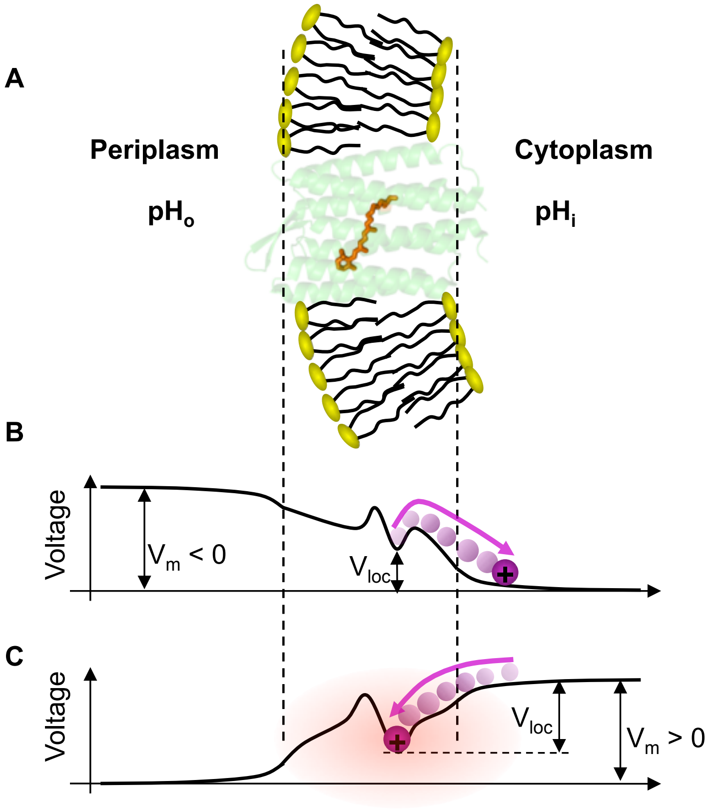

Figure 2.15: Model of voltage sensitivity PROPS. (**A**) Cartoon of PROPS in a lipid bilayer membrane. The structure shown is bacteriorhodopsin; the structures of GPR or PROPS are not known. (**B**) Potential profile when $V_m < 0$. The potential minimum inside the protein represents the Schiff base (SB). Protons move from the SB to the cytoplasm, causing the protein to become non-fluorescent. (**C**) Potential profile when $V_m > 0$. Protons move from the cytoplasm onto the SB, causing the protein to become fluorescent. The equilibrium ratio of protonated to deprotonated SB depends on the voltage drop, V_{loc}, between the SB and the cytoplasmic reservoir of protons. The total membrane potential, V_m, is in general greater in magnitude than V_{loc}.

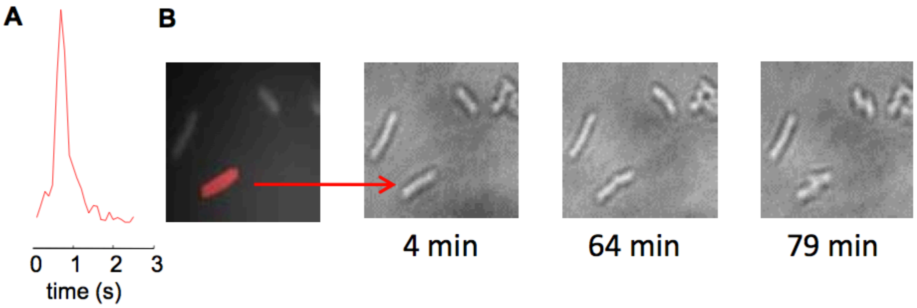

Figure 2.16: Blinking cells continue to grow and divide. A sample of *E. coli* expressing PROPS was incubated between a glass coverslip and an agarose pad made with minimal medium, pH 7.5. At t = 0 a fluorescence movie was acquired (1 min, 60 W/cm^2), showing blinking cells. The imaging laser was turned off, and the cells were incubated in the dark at 35° C. Cells that had initially blinked continued to grow and divide, establishing that blinking cells were alive. (**A**) Intensity trace showing a single blink from the red-highlighted cell. (**B**) White-light images showing subsequent growth and division.

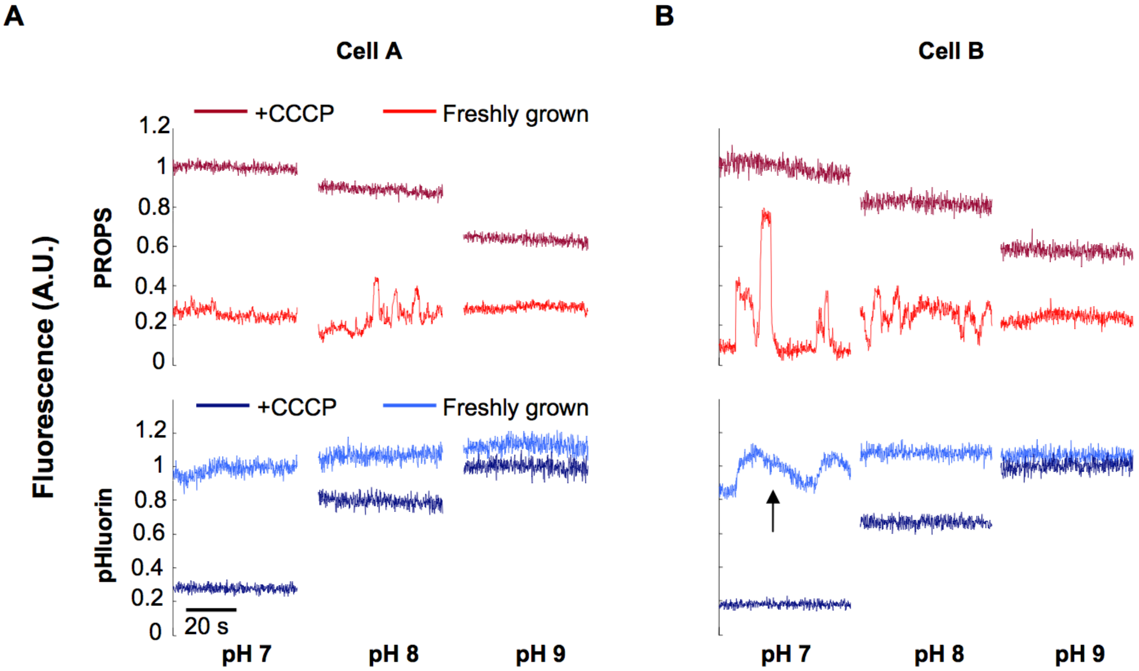

Figure 2.17: pH$_i$ is constant during spikes in V_m. Fluorescence of PROPS and pHluorin in single *E. coli*, as a function of pH$_o$, before and after treatment with CCCP. (**A**) and (**B**) show data from two representative cells and have the same scale and legend. In freshly grown cells, the fluorescence of pHluorin and PROPS were both only weakly sensitive to pH$_o$, consistent with homeostasis of pH$_i$ and a fluorescence-determining group in PROPS not exposed to the extracellular medium. At pH$_o$ = 7, we occasionally observed slow changes in pHluorin fluorescence accompanying large blinks in the PROPS channel (indicated by the arrow in panel **B**). The timecourse of the changes in pHluorin fluorescence was slower than the changes in PROPS fluorescence and slower than the intrinsic response speed of pHluorin, indicating that variation in pH$_i$ and variation in V_m are distinct processes. At pH$_o$ between 7.5 and 9 we never observed changes in pHluorin fluorescence during a blink.
After treatment with CCCP, pHluorin and PROPS showed pH-dependent fluorescence, confirming a cytoplasm-exposed fluorescence-determining group in PROPS.

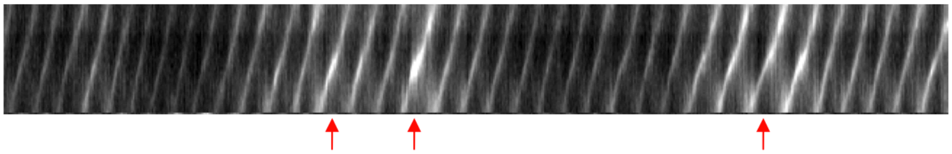

Figure 2.18: Rotary kymograph at pH$_o$ 7. We only observed a robust correspondence between blinking and loss of flagellar torque at pH$_o$ 8.5. At pH 7, the rotation slowed only slightly during blinks (red arrows). We attribute this pH-dependence to the varying contributions of V_m and ΔpH to the PMF, depending on pH$_o$. At low pH$_o$, the PMF was dominated by ΔpH. Only when pH$_o$ was raised so that pH$_o$ ~ pH$_i$ was the PMF determined predominantly by V_m. This condition occurred at pH$_o$ ~ 8.5.

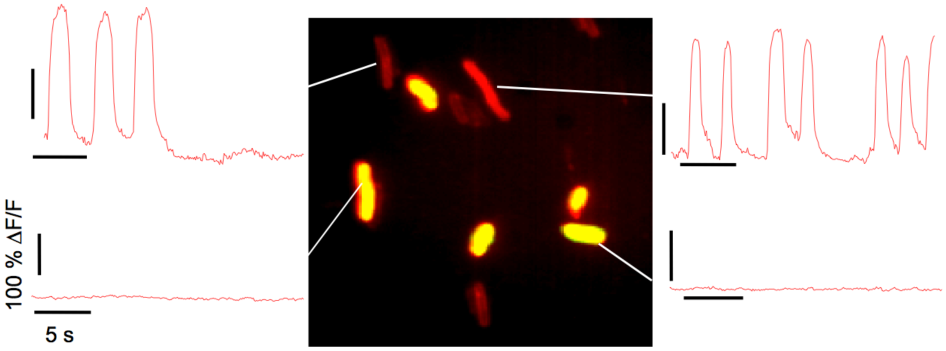

Figure 2.19: Voltage-sensitive dyes only labeled non-blinking cells. Red channel: PROPS fluorescence; Green channel: Di-4-ANEPPS fluorescence. Cells expressing PROPS and containing dye appear yellow. Red traces indicate PROPS dynamics. All scale bars are 100% ΔF/F vertical and 5 s horizontal. In every field of view we observed two populations: cells that blinked but that did not take up detectable levels of dye, and cells that took up detectable levels of dye but that did not blink. Washing the cells *in situ* with fresh dye solution did not lead to labeling of blinking cells. Pre-treatment with EDTA also did not lead to labeling of blinking cells. This puzzling observation may be due to blinking-associated efflux, or may be because blinking requires an intact outer membrane, which is also impermeable to dye. Alternatively, VSDs might inhibit blinking in cells that take up the dye.

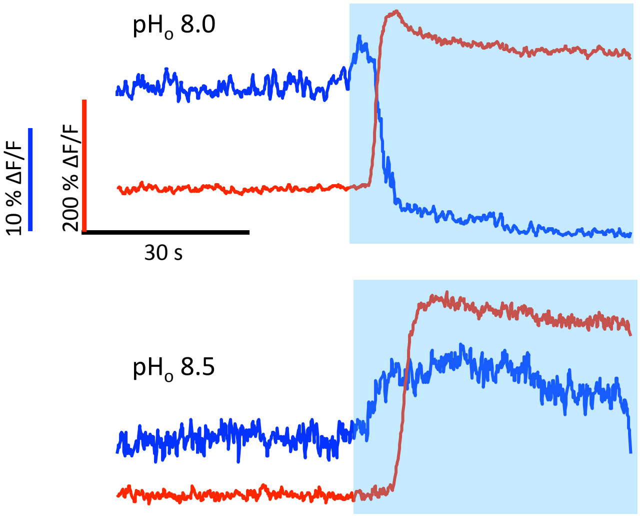

Figure 2.20: Determination of the value of pH$_o$ at which pH$_i$ = pH$_o$. Cells co-expressing PROPS and pHluorin were equilibrated in buffers with pH$_o$ values between 8 and 8.5. PROPS (red) and pHluorin (blue) fluorescence were monitored during addition of CCCP (50 μg/mL) at constant pH$_o$. Blue bar indicates addition of CCCP. The scale bars are the same for both panels. Addition of CCCP caused pH$_i$ to become equal to pH$_o$, with a corresponding change in pHluorin fluorescence. The case of pH$_i$ = pH$_o$ occurred at pH 8.3, and is shown in **Fig. 2.3D** in the main text. At all values of pH$_o$, addition of CCCP caused PROPS to become sharply brighter, indicating electrical depolarization.

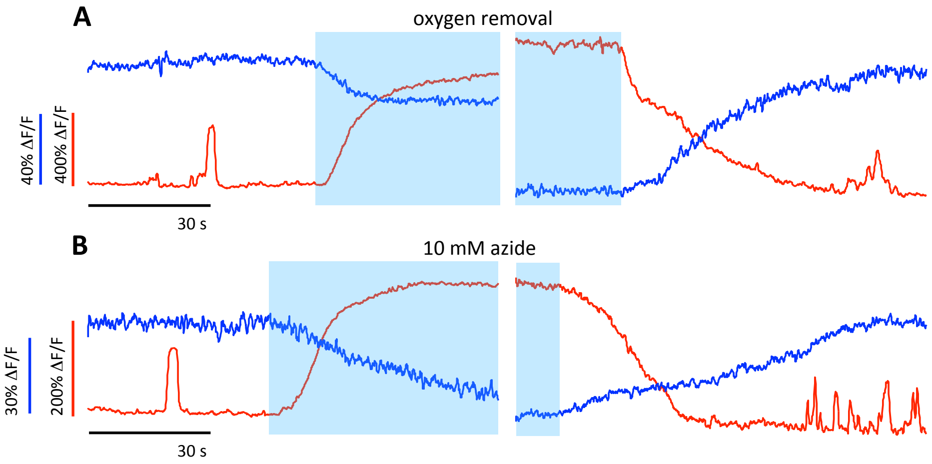

Figure 2.21: Metabolic perturbations interrupt pH homeostasis. PROPS and pHluorin fluorescence during (**A**) removal and reintroduction of oxygen and (**B**) addition and removal of sodium azide (10 mM). Data taken with $\lambda_{exc} = 633$, 10 W/cm^2 in minimal medium pH 7.5. (**B**) Removal of oxygen or addition of sodium azide at pH$_o$ 7.5 caused pH$_i$ to gradually equilibrate to pH$_o$. Reintroduction of regular minimal medium led to restoration of the initial pH$_i$ and resumption of blinking.

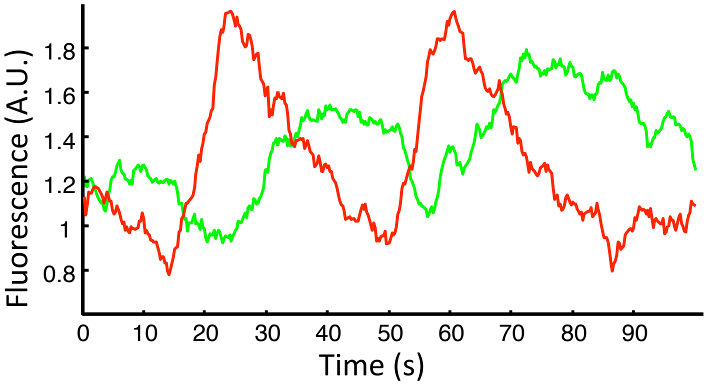

Figure 2.22: Efflux of TMRM during blinks under dim red illumination. 2 W/cm^2 at $\lambda_{exc} = 633$ nm, 0.23 W/cm^2 at $\lambda_{exc} = 532$ nm), pH 8. We observed efflux of TMRM coincident with blinks of PROPS at the lowest red illumination intensity at which PROPS was observable. In blinking cells containing enough TMRM to record a fluorescent signal, there were noticeable drops in TMRM intensity during a blink, though the TMRM fluorescence often recovered after the blink.

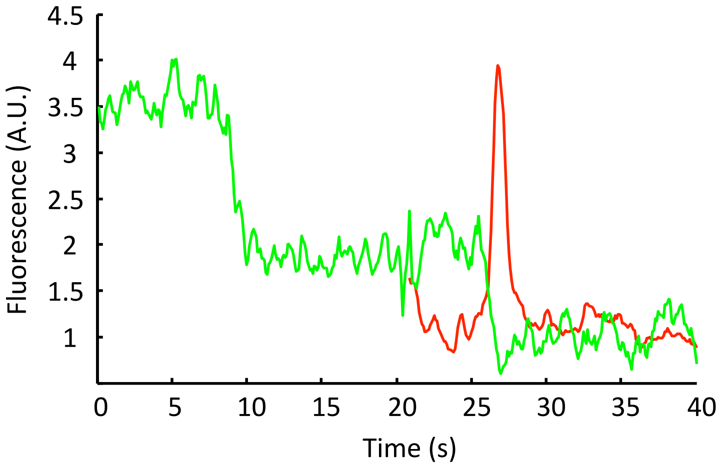

Figure 2.23: Efflux of TMRM in the absence of red illumination. Fluorescence of a single cell containing PROPS (red) and TMRM (green). The green laser was on for the whole experiment. The red laser was turned on at 20 s at I = 10 W/cm². Similar efflux events occurred before and after the red laser was turned on; when the red laser was on, efflux was accompanied by a blink in the PROPS channel. These results establish that blinking-associated efflux occurred in the absence of red illumination. Events like that shown here were rare.

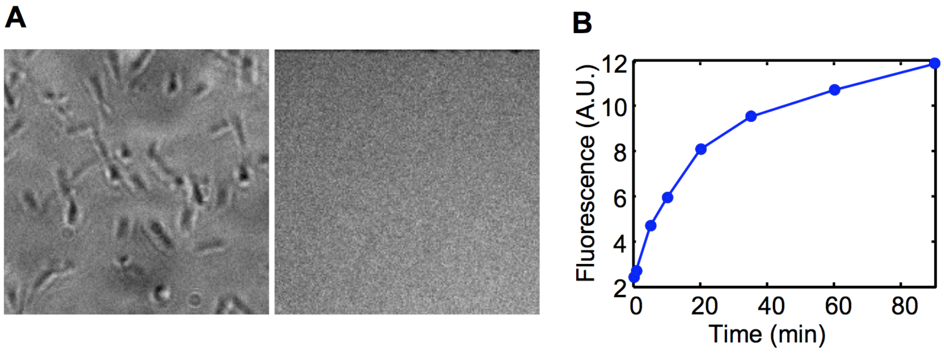

Figure 2.24: Retinal is necessary for PROPS fluorescence. (**A**) Left: transmitted light image of a field of cells expressing PROPS but without retinal. Right: fluorescence image of the same field of view. (**B**) Fluorescence of a single E. coli expressing PROPS after 20 μM retinal was added at 0 min.

2.7 SUPPLEMENTARY TABLES

Table 2.1: Genetic backgrounds of the *E. coli* strains used.

BL21 (DE3)	*fhuA2 [lon] ompT gal (λ DE3) [dcm] ΔhsdS* *λ DE3 = λ sBamHIo ΔEcoRI-B int::(lacI::PlacUV5::T7 gene1) i21 Δnin5*
BW25113 (Coli Genome Stock Center)	*Δ(araD-araB)567*, *ΔlacZ4787*(::rrnB-3), lambda-, *rph-1*, *Δ(rhaD-rhaB)568*, *hsdR514*
UT5600	F- *ara-14 leuB6 secA6 lacY1 proC14 tsx-67 Δ(ompT-fepC)266 entA403 trpE38 rfbD1 rpsL109 xyl-5 mtl-1 thi-1*
JY29 (Gift from Howard Berg)	*Thr-1 araC14 leuB6*(Am) *fhuA31 lacY1 tsx-78 λ- eda-50 hisG4(Oc) rfbC1 rpsL136 xylA5 mtl-1 metF159 thi-1 ΔfliC*, sticky fliC allele was cloned into pACYC184 (CmR) under the native promoter of fliC
Tuner™ (Novagen)	*fhuA2 [lon] ompT gal (λ DE3) [dcm] ΔhsdS λ DE3 = λ sBamHIo ΔEcoRI-B int::(lacI::PlacUV5::T7 gene1) i21 Δnin5 ΔlacZY*

Table 2.2: Growth and induction conditions.

Strain	**Temperature**	**Growth Medium**	**Inducer**	**Antibiotic resistance**
BL21	33 ºC	LB	IPTG 0.5 mM	Amp, Strep (for pHluorin)
BW25113	33 ºC	LB	Ara 0.0005%	Amp
UT5600	33 ºC	LB	Ara 0.02%,	Amp, Strep
JY29	30 ºC	Tryptone broth	IPTG 0.2 mM	Amp, Cm
Tuner™	33 ºC	LB	IPTG 0.5 mM	Amp

Table 2.3: Light sources used in the experiments. Multiple wavelengths were combined with appropriate dichroic mirrors.

Wavelength	Power	Type	Manufacturer
633 nm	17 mW	HeNe	SpectraPhysics
532 nm	50 mW	Solid-state	Coherent 215-M
488 nm	60 mW	Solid-state	Omicron PhoxX
407 nm	80 mW	Solid-state	Blue-ray DVD player
White light, wavelength selectable via AOTF	6 W	Supercontinuum	Fianium SC-450-6-AOTF
460 – 490 nm	3 W	Luxeon III	Philips

Table 2.4: Gene constructs tested in attempt at eukaryotic expression of PROPS. **GPR** – bacterial codon GPR, **hGPR** – human codon GPR, **ss(A)** – endogenous GPR signal sequence, **ss(B)** - B2 nicotinic acetylcholine receptor signal sequence, **ss(C)** – bovine pre-prolactin signal sequence, **ER export** – Kir2.1 ER export motif; FCYENEV, **TS** – Kir2.1 trafficking sequence, **G export** – Kir golgi export motif, **XC(BR)** – extracellular domain from bacteriorhodopsin, **XC(HR)** – extracellular domain from halorhodopsin.

Plasmid	Gene	Targeting to eukaryotic plasma membrane
pADD161	ss(A) – GPR	No
pADD173	ss(A) – hGPR	No
pADD191	ss(A) – hGPR – Venus	No
pADD192	ss(B) – hGPR – Venus	No
pADD193	ss(B) – hGPR – Venus – ER export	No
pADD194	ss(C) – hGPR – Venus	No
pADD195	ss(C) – hGPR – Venus – ER export	No
pADD206	ss(A) – hGPR – TS – Venus – ER export	No
pADD210	ss(B) – hGPR – TS – Venus – ER export	No
pADD211	ss(C) – hGPR – TS – Venus – ER export	No
pADD221	ss(A) – hGPR – TS – ER export	No
pADD223	ss(A) – hGPR – TS – G export – ER export	No
pADD224	ss(A) – hGPR – TS – Venus – G export – ER export	No
pADD226	XC(HR) – hGPR – TS – Venus – ER export	No
pADD227	XC(BR) – hGPR – TS – Venus – ER export	No
pADD222	SS(C) – Venus – hGPR – TS – ER export	No
pADD228	SS(C) – Venus – hGPR – TS – G Export – ER export	No

Table 2.5: Cell lines tested for eukaryotic expression.

Cell Line	Plasmid	Temperature	Targeting to eukaryotic plasma membrane
HEK 293	All plasmids	30 and 37 °C	No
3T3	pADD223, pADD227	30 and 37 °C	No
HeLa	pADD223, pADD227	30 and 37 °C	No
COS7	pADD223, pADD227	30 and 37 °C	No

Table 2.6: Voltage sensitive dyes attempted in *E. coli*.

Voltage Sensitive Dye	Excitation wavelength (nm)	Labeled blinking cells
Di – 4 – ANEPPS	488	No
Di – 8 – ANEPPS	488	No
TMRM	532	Yes, but effluxed during blinks

2.8 SUPPLEMENTARY MOVIES

2.8.1 SUPPLEMENTARY MOVIE

`http://www.sciencemag.org/content/suppl/2011/07/13/333.6040.345.DC1/1204763s1.avi`

E. coli strain BW25113 expressing PROPS imaged under high red light intensity (λ = 633 nm, I = 20 W/cm^2). Cells were in minimal medium (pH 8) at room temperature. Movie is sped up by 4x.

2.8.2 Supplementary Movie

`http://www.sciencemag.org/content/suppl/2011/07/13/333.6040.345.DC1/1204763s2.avi`

E. coli strain BW25113 expressing PROPS imaged under low red light intensity (λ = 633 nm, I = 1 W/cm^2). Cells were in minimal medium (pH 7) at room temperature. Movie is sped up by 8x.

2.8.3 Supplementary Movie

`http://www.sciencemag.org/content/suppl/2011/07/13/333.6040.345.DC1/1204763s3.avi`

E. coli strain JY29 expressing PROPS adhered to a coverslip by a sticky flagellum. Cells were in minimal medium (pH 8.5). Movie is slowed down by 3x.

2.8.4 Supplementary Movie

`http://www.sciencemag.org/content/suppl/2011/07/13/333.6040.345.DC1/1204763s4.avi`

E. coli strain BW25113 expressing PROPS exposed to violet light (λ = 407 nm, I = 100 W/cm^2) while imaging PROPS (λ = 633 nm, I = 20 W/cm^2). Cells were in minimal medium (pH 7) at room temperature. Movie is sped up by 6x.

2.8.5 Supplementary Movie

`http://www.sciencemag.org/content/suppl/2011/07/13/333.6040.345.DC1/1204763s5.avi`

E. coli strain BW25113 expressing PROPS during oxygen removal with the chemical system Oxyrase. Oxyrase was dissolved in minimal medium (pH 7) according to the manufacturer's directions. Imaging at λ = 633 nm, I = 20 W/cm^2. Movie is sped up by 6x.

2.8.6 SUPPLEMENTARY MOVIE

`http://www.sciencemag.org/content/suppl/2011/07/13/333.6040.345.DC1/1204763s6.avi`

E. coli strain BW25113 expressing PROPS during azide addition (10 mM). Imaging at λ = 633 nm, I = 20 W/cm^2. Movie is sped up by 6x.

2.8.7 SUPPLEMENTARY MOVIE

`http://www.sciencemag.org/content/suppl/2011/07/13/333.6040.345.DC1/1204763s7.avi`

E. coli strain BW25113 expressing PROPS during CCCP addition (50 μg/mL). Imaging at λ = 633 nm, I = 20 W/cm^2. Movie is sped up by 6x.

2.9 MANUSCRIPT INFORMATION

2.9.1 PREVIOUSLY PUBLISHED AS

A version of this chapter appeared in [87]:

J. M. Kralj, D. R. Hochbaum, A. D. Douglass, and A. E. Cohen. Electrical spiking in escherichia coli probed with a fluorescent voltage indicating protein. *Science*, 333:345–348, 2011.

2.9.2 ACKNOWLEDGEMENTS

We thank K. Rothschild for helpful discussions and for the GPR plasmid. We also thank H. Berg, R. Losick, J. Yuan, H. Inada, A. Garner, and D. Kahne for helpful discussions. G. Miesenbock provided the pHluorin plasmid. A. Fields, H. Bayraktar, V. Venkatachalam, and L. Bane helped with measurements. This work was supported by the Harvard Center for Brain Science, an Intelligence Community Postdoctoral Fellowship (J.M.K.), a National Science Foundation Graduate Fellowship (D.R.H.), a Helen Hay Whitney Postdoctoral Fellowship (A.D.D.), and a Charles A. King Trust Postdoctoral Fellowship (A.D.D).

2.9.3 THE AUTHOR'S CONTRIBUTION

Joel M. Kralj and Daniel R. Hochbaum conducted experiments. Adam D Douglass led attempts to express PROPS in mammalian cells. Adam E. Cohen, Daniel R. Hochbaum, and Joel M. Kralj analyzed the data. All authors contributed to writing the manuscript. Adam E. Cohen directed the project.

3

Optical recording of action potentials in mammalian neurons using a microbial rhodopsin

3.1 Introduction

To study the dynamics of a complex neural circuit, one would like to record action potentials from many neurons simultaneously. Optical imaging promises to realize this goal [2, 29, 127, 139, 155], and voltage indicators have been developed based on small molecules [65, 73], fluorescent proteins [147, 160], and hybrid protein-dye systems [20, 148]. Single action potentials with high signal-to-noise ratio (SNR) have been recorded recently in individual spines of mammalian neurons in slices using an organic voltage-indicating dye, but this approach required intracellular injection of dye and cumulative illumination of less than 2 s to avoid phototoxicity [129]. Electrical activity in mammalian neurons has been recorded *in vivo* using a genetically encoded voltage indicator, but this required averaging over multiple trials [2]. Signals suggestive of single spikes have been reported when the optical signal was aligned with an electrophysiology trace, but the SNR was inadequate for all-optical spike identification. Calcium imaging is widely used as an indirect readout of electrical activity but is only useful when slower readouts (hundreds of milliseconds) are acceptable [156]. Despite this progress, direct and sensitive optical measurement of membrane potential remains elusive. All approaches have one or more serious limitations, including slow response, lack of sensitivity, difficulty in targeting or phototoxicity. No genetically encoded voltage indicator has had adequate sensitivity and speed to reliably identify action potentials from mammalian neurons on a single-trial basis.

We recently developed a fast and sensitive voltage indicator based on green-absorbing proteorhodopsin [87]. This proteorhodopsin optical proton sensor (PROPS) revealed electrical spiking in *Escherichia coli*, but efforts to use PROPS in eukaryotic cells failed because the protein did not localize to the plasma membrane. Addition of targeting and localization sequences to PROPS did not help. Thus we decided to test other microbial rhodopsins as putative voltage sensors, focusing on proteins known to localize to the eukaryotic plasma membrane. Archaerhodopsin 3 (Arch) from *Halorubrum sodomense* is a light-driven outward proton pump that captures solar energy for its host [70]. Recently Arch has been expressed in mammalian neurons, where it enabled optical silencing of neural activity and was minimally perturbative to endogenous function in the dark [27]. We hypothesized that Arch could be 'run' in reverse: that a membrane potential could alter the optical properties of the protein and thereby provide a voltage sensor that functioned through a mechanism similar to that of PROPS.

We found that Arch resolved individual action potentials in mammalian neurons *in vitro*, with high SNR and low phototoxicity. Arch enabled mapping of neuronal action potentials with sub-millisecond temporal resolution and subcellular spatial resolution. However, the wild-type form of Arch generated a hyperpolarizing photocurrent upon exposure to the imaging laser. The mutation D95N in Arch eliminated this photocurrent but also slowed the response to 41 ms.

3.2 RESULTS

3.2.1 PHOTOPHYSICS OF ARCH

At neutral pH, bacterially expressed Arch was pink, but at high pH the protein turned yellow (**Fig. 3.1a**), with a pK_a for the transition of 10.1. Based on homology to other microbial rhodopsins [92], we attributed the pH-induced color change to deprotonation of the Schiff base, which links the retinal chromophore to the protein core. We reasoned that a change in membrane potential might change the local electrochemical potential of the proton at the Schiff base, tipping the acid-base equilibrium and inducing a similar color shift. This mechanism of voltage-induced color shift has been reported previously in dried films of bacteriorhodopsin [85] and formed the hypothesized basis of voltage-sensitivity in PROPS [87].

Changes in optical absorption would be challenging to detect in a single cell, owing to the small quantity of protein in the membrane. However, most microbial rhodopsins are weakly fluorescent [93], so we characterized Arch as a prospective fluorescent indicator (**Table 3.1**). At neutral pH, Arch emitted far-red fluorescence (emission wavelength, λ_{em}, was 687 nm), whereas at high pH Arch was not fluorescent (**Fig. 3.1b and Supplementary Fig. 3.6**). The fluorescence quantum yield of Arch was low (9×10^4) but the photostability was comparable to that of members of the GFP family [144]. We found that laser illumination and electron-multiplying charge-coupled device (EMCCD) detection were necessary for observing Arch fluorescence. A comparison of photobleaching rates of Arch (excited at 640 nm) with those of enhanced (e)GFP (excited at 488 nm), in a 1:1 Arch-eGFP fusion, showed that the mean numbers of photons emitted per molecule before photobleaching were ~1:3.9 (Arch:eGFP). The broad absorption peak enabled excitation of Arch at λ = 640 nm, a wavelength where few other cellular components absorb, and the far red emission occurred in a spectral region of little background autofluorescence.

Table 3.1: Optical and electrical response of Arch and Arch(D95N). [a]Excitation at $\lambda = 532$ nm. [b]Absorption spectra calibrated assuming the same peak extinction coefficient as bacteriorhodopsin, 63,000 M^{-1} cm^{-1} (ref. [133] and **Methods Section 3.4**). [c]Quantum yield (QY) determined via comparison to Alexa Fluor 647 with excitation at $\lambda = 633$ nm. [d]Measured in a 1:1 fusion with eGFP. [e]Determined via singular value decomposition on absorption spectra. [f]Determined from step response. Arch(D95N) has a minor component of its response (20%) that is fast (<500 μs). [g]$\hat{V}_{FL}$ is the membrane potential estimated from fluorescence. Noise determined at frequencies $f \geq 0.1$ Hz in HEK293 cells.

	λ_{max} absorbance (nm)	λ_{max} emission[a] (nm)	ε_{633} (M^{-1} cm^{-1})[b]	QY [c]	Photostability relative to eGFP[d]	pK_a of Schiff base [e]	$\tau_{response}$ [f] (ms)	Noise in V_{FL} ($\mu V\ Hz^{-1/2}$) [g]	Photo-current
Wild-type Arch	558	687	6,300	9×10^{-4}	0.25	10.1	< 0.5	625	yes
Arch(D95N)	585	687	37,500	4×10^{-4}	0.1	8.9	41	260	no

We imaged fluorescence of Arch in HEK293 cells supplemented with 5 μM all-trans retinal in an inverted fluorescence microscope with red illumination (λ = 640 nm, 20 mW, intensity (I) = 540 W/cm^2), a high-numerical-aperture objective, a Cy5 filter set and an EMCCD camera (**Methods Section 3.4 and Supplementary Fig. 3.7**). The cells exhibited fluorescence predominantly localized to the plasma membrane. Cells not expressing Arch were not fluorescent. Cells showed 17% photobleaching over a continuous 10-min exposure and retained normal morphology during this interval.

The fluorescence of HEK293 cells expressing Arch was highly sensitive to membrane potential, as determined via whole-cell voltage clamp (**Supplementary Movie 3.7.1**). Fluorescence of Arch in the plasma membrane increased by a factor of two between −150 mV and +150 mV, with a nearly linear response throughout this range (**Fig. 3.1c**). The response of fluorescence to a step in membrane potential occurred within the 500 μs time resolution of our imaging system on both the rising and falling edge (**Fig. 3.1d**)[1]. Application of a sinusoidally varying mem-

---

[1] Accurate application of fast steps in voltage is difficult due to potential electrical artifacts introduced by the compensation circuitry of the patch-clamp amplifier. Ref. [103] repeats the fluorescence step-response measurement we report here without compensation. Instead, they model the response of membrane voltage to a step in voltage from the amplifier and use it to extract the response speed of Arch fluorescence (using a PMT). They report τ_{up} of ~0.4 ms and τ_{down} of ~0.6 ms, similar to our result here.

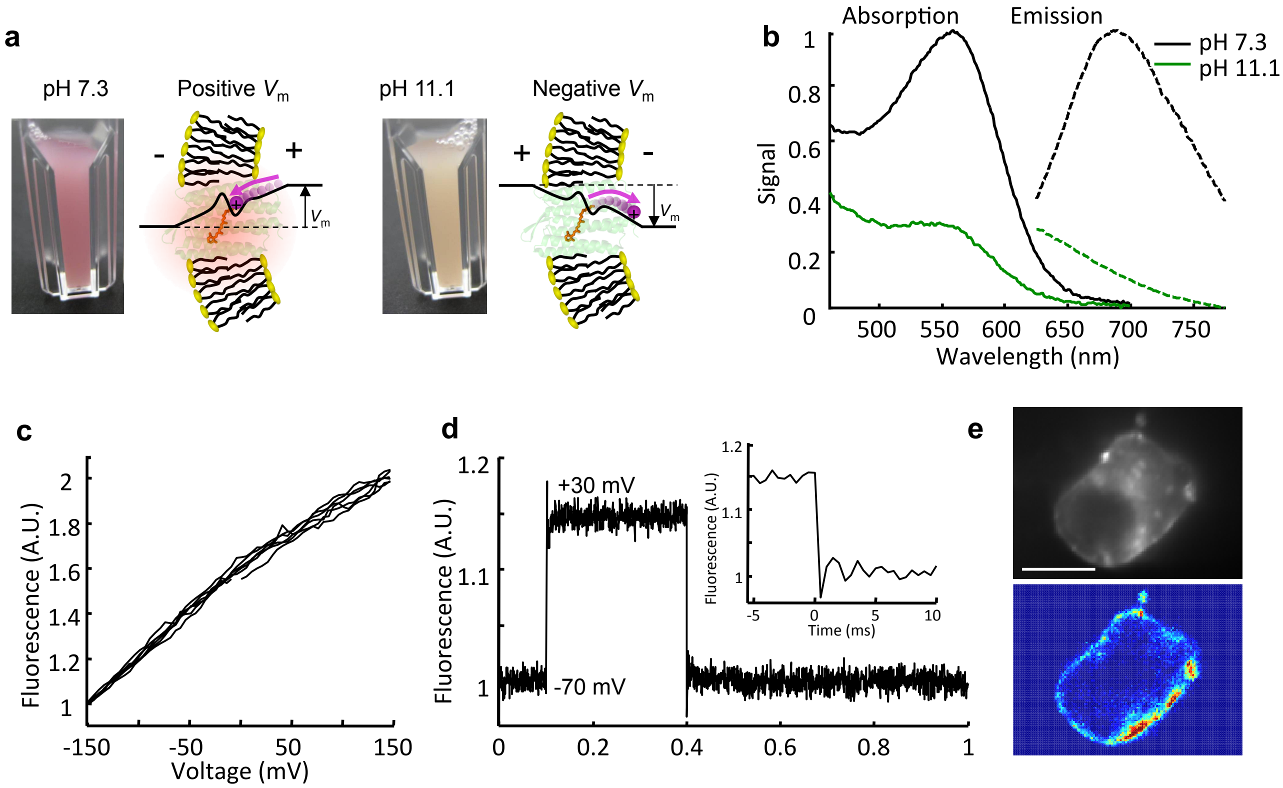

Figure 3.1: Arch is a fluorescent voltage indicator. (**a**) Model of Arch as a voltage sensor, in which pH and membrane potential can both alter the protonation of the Schiff base. The cuvettes contain intact *E. coli* expressing Arch. (**b**) Absorption and fluorescence emission spectra of Arch at neutral and high pH. (**c**) Fluorescence of Arch (divided by the value at −150 mV) as a function of membrane potential (recorded over six consecutive sweeps). (**d**) Dynamic response of Arch to steps in membrane potential between −70 mV and +30 mV. The overshoots on the rising and falling edges were an artifact of electronic compensation circuitry. The smaller amplitude compared to **c** is because background subtraction was not performed in **d**. Data were averaged over 20 cycles. Inset, step response occurred in less than the 500 μs resolution of the imaging system. (**e**) Fluorescence micrograph of an HEK293 cell expressing Arch (top) and pixel-weight matrix showing regions of voltage-dependent fluorescence (bottom). a.u., arbitrary units. Scale bar, 10 μm.

brane potential led to sinusoidally varying fluorescence; at a frequency (f) of 1 kHz, the fluorescence oscillations retained 55% of their low-frequency amplitude (**Supplementary Fig. 3.8**). Arch retained its endogenous proton-pumping capability, and illumination with the imaging laser generated outward photocurrents of 10–20 pA.

Fluorescent voltage indicators are often characterized by the fractional change in fluorescence, $\Delta F/F$, per 100 mV of membrane potential. This metric suffers from subjectivity in the choice of which pixels are chosen to represent 'signal' and which are chosen for 'background'.The quantity $\Delta F/F$ also does not indicate temporal stability of the signal, nor information about the SNR (except in the rarely achieved case of shot noise–limited detection). Thus we sought an objective measure of the precision with which small changes in membrane voltage (V_m) could be detected.

We developed a linear regression algorithm to identify pixels whose intensity varied together with an external 'training' stimulus (**Methods Section 3.4**). When trained on the unweighted whole-field fluorescence, this algorithm identified pixels associated with the cell membrane (**Fig. 3.1e**) and rejected pixels corresponding to bright but voltage-insensitive intracellular aggregates. Application of the pixel weight matrix to the raw fluorescence data led to estimates of voltage-induced changes in fluorescence with improved SNR relative to unweighted whole-field fluorescence. This use of the pixel-weighting algorithm made no use of electrophysiology data.

Fluorescence data alone were insufficient to determine true membrane potential because variation in the cell morphology, expression, extent of membrane localization and illumination conditions led to an a priori unknown offset and scale factor between fluorescence and voltage. When trained on the electrophysiology data, the algorithm returned pixel-weight coefficients that could be used to convert fluorescence images into a maximum likelihood estimate of the membrane potential, $\hat{V}_{FL}$ (**Methods Section 3.4**).

After training the algorithm on voltage sweep data from −150 mV to +150 mV, the fluorescence-based $\hat{V}_{FL}$ matched the electrically recorded V_m with an accuracy of 625 $\mu V/Hz^{1/2}$ (**Supplementary Fig. 3.9**). Over timescales longer than ~10 s, laser power fluctuations and cell motion degraded the sub-millivolt precision of the voltage determination but had little effect on the ability to detect fast transients in V_m. Our simple algorithm does not accommodate cell motion, multiple cells undergoing different voltage dynamics or substantial lags in voltage propagation from one region to another. Other algorithms [114] exist to handle such scenarios, however.

3.2.2 ARCH FLUORESCENCE IDENTIFIED ACTION POTENTIALS *IN VITRO*

We tested Arch as a voltage indicator in cultured rat hippocampal neurons, using viral delivery. Neurons expressing Arch showed membrane-localized fluorescence (**Fig. 3.2a**). Under whole-cell current clamp, cells exhibited spiking upon injection of current pulses of 200 pA. Individual spikes were accompanied by clearly identifiable increases of whole-field fluorescence (**Fig. 3.2b and Supplementary Movie 3.7.2**). After scaling of the fluorescence trace to overlay on the voltage, the root-mean-square (r.m.s.) deviation between the two was $\sigma_{\hat{V}}$ = 7.2 mV. Training the pixel-weighting algorithm on the whole-field fluorescence led to a 74% improve- ment in SNR, with an r.m.s. deviation between the predicted and measured voltage (after scaling and offset adjustment) of $\sigma_{\hat{V}}$ = 4.2 mV (**Fig. 3.2c**). This training procedure made no use of the electrical recording. Training the pixel-weighting algorithm on the electrical recording led to an additional 5% increase in SNR, to $\sigma_{\hat{V}}$ = 4.0 mV, and did not require adjustment of scaling and offset (**Fig. 3.2d**).

We imaged the dynamics of action potentials with subcellular resolution (**Supplementary Fig. 3.10**). To improve the SNR we averaged multiple temporally registered movies of single spikes (**Fig. 3.2e and Supplementary Movie 3.7.3**). Action potentials appeared to occur nearly simultaneously throughout most regions of the cell, as expected given the field of view (100 μm) and exposure time (2 ms). However, in localized regions the action potential lagged by 2–3 ms. The pixel-weighting algorithm did not detect the cellular regions with delayed action potentials, but the lag was readily seen in **Supplementary Movie 3.7.3**. These results suggest that Arch may be used to map intracellular dynamics of action potentials in genetically specified neurons, in a manner similar to a recent demonstration with voltage-sensitive dyes [129].

We created single-trial optical and electrical recordings (**Fig. 3.2f**). At a 2-

Figure 3.2 ***(following page)*****: Optical recording of action potentials with Arch.** (**a**) luorescence micrograph of a cultured rat hippocampal neuron expressing Arch (composite of two fields of view). (**b**) Low-magnification image of the neuron in **a** (left). Whole-field fluorescence (red) during a single-trial recording at 500 frames/s (right). The fluorescence was scaled to overlay the electrical recording (blue). (**c**) Pixel-by-pixel map of cross-correlation between whole-field and single-pixel intensities (red) overlaid on the average fluorescence (gray) (left). Note that the process extending to the top left of the cell body does not appear in the red channel; it is electrically decoupled from the cell. Pixel-weighted fluorescence (red) and electrical recording (blue) (right). (**d**) Pixel-by-pixel map of cross-correlation between electrical recording and single-pixel intensities (red) overlaid on the average fluorescence (gray) (left). Pixel-weighted fluorescence (red) and electrical recording (blue) (right). (**e**) Subcellular localization of an action potential in regions indicated by colored polygons (left) and time course of an action potential averaged over 98 events (right) in the regions indicated with the corresponding colors. The top black trace is the electrical recording. Optical recordings appear broadened owing to the finite (2 ms) exposure time of the camera. The white arrow indicates a small protrusion that has a substantially delayed action potential relative to the rest of the cell. Vertical scale on fluorescence traces is arbitrary. (**f**) Single-trial recordings of action potentials recorded at a frame rate of 2 kHz. The pixel weight matrix was determined from the accompanying electrophysiology recording. Averaged spike response for 269 events in a single cell is shown on top right. (**g**) Application of a voltage to a single neuron caused an increase in fluorescence that distinguished a neuron from its neighbors (top). Time-average Arch fluorescence of multiple transfected neurons (left). Same field of view after membrane potential was modulated by whole-cell voltage clamp (right). Responsive pixels were identified via cross-correlation of pixel intensity and applied voltage (V, red). Scale bars, 10 μm (**a,e,g**) and 50 μm (**b–d**).

Figure 3.2: (continued)

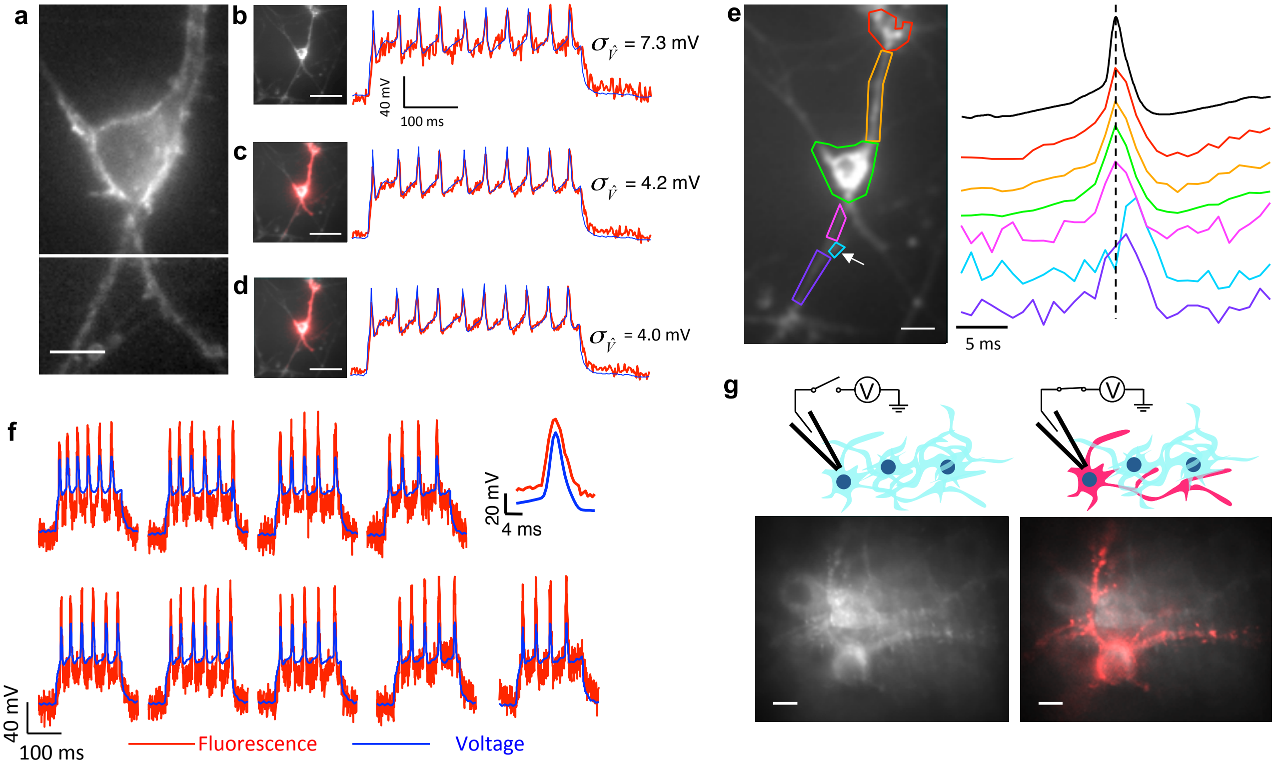

kHz frame rate, the SNR in the fluorescence (spike amplitude:baseline noise) was 10.5. A spike-finding algorithm correctly identified 99.6% of the spikes (based on comparison to simultaneously recorded membrane potential), with a false positive rate of 0.7% (n = 269 spikes; **Methods Section 3.4**). The average action potential waveform determined by fluorescence coincided with the waveform recorded electrically. We observed single cells for up to 4 min of cumulative exposure, with no detectable change in resting potential or spike frequency.

We developed a procedure to electrically tag a single cell in an otherwise overgrown field of neurons, similar to that in reference [17]. The average fluorescence of the population of cells, all expressing Arch, did not show clearly resolved cellular structures (**Fig. 3.2g**). We formed a whole-cell patch on one cell, which we then subjected to a voltage clamp triangle wave of amplitude 150 mV, under video observation. The weight matrix, indicating which pixels contained information about the applied voltage, yielded a clear image of the target cell and its processes. Electrical tagging provides a complement to genetic [96] and chemical [119] methods that are currently used to label single neurons.

In the absence of added retinal, neurons expressing Arch showed clearly identifiable fluorescence flashes accompanying individual spikes (**Supplementary Fig. 3.11a**), indicating that neurons contained sufficient endogenous retinal to populate some of the protein. Addition of supplemental retinal led to a 30–60% increase in fluorescence over 30 min (**Supplementary Fig. 3.11b**). Experiments with Arch and other microbial rhodopsins *in vivo* have shown that endogenous retinal is sufficient for optogenetic control of neural activity [19]. Thus, Arch may function as a voltage indicator in vivo without exogenous retinal.

3.2.3 ARCH(D95N) IS A NONPUMPING VOLTAGE INDICATOR

Illumination at 640 nm was far from the peak of the Arch absorption spectrum (λ = 558 nm), but the imaging laser nonetheless induced photocurrents of 10–20 pA in HEK293 cells expressing Arch (**Fig. 3.3a**). We sought to develop a mutant which did not perturb the membrane potential, yet which maintained voltage sensitivity. The mutation D85N in bacteriorhodopsin eliminated proton pumping [157], so we introduced the homologous mutation, D95N, into Arch. This mutation eliminated the photocurrent (**Fig. 3.3a**) and shifted several other photophysical properties of importance to voltage sensing (**Table 3.1, Fig. 3.3 and Supplementary Fig. 3.12**). Arch(D95N) was more sensitive to voltage than Arch and displayed a threefold increase in fluorescence between −150 mV and +150 mV, with nearly linear sensitivity from −120 to +120 mV, but had a slower response (**Fig. 3.3b–d and Supplementary Movies 3.7.4 and 3.7.5**). After calibration with a voltage ramp, Arch(D95N) resolved voltage steps of 10 mV, with a noise in the voltage estimated from fluorescence of 260 μV/Hz$^{1/2}$ over timescales < 12 s.

Under illumination conditions typically used for imaging neural activity ($I = 1{,}800$ W/cm^2 and $\lambda = 640$ nm), the light-induced outward photocurrent was typically 10 pA[2] in neurons expressing Arch. Under current-clamp conditions this photocurrent shifted the resting potential of the neurons by up to −20 mV. For neurons near their activation threshold, this photocurrent could suppress firing (**Fig. 3.4a**), so we explored the nonpumping Arch(D95N) variant as a voltage indicator in neurons. Illumination of Arch(D95N) did not perturb membrane potential in neurons (**Fig. 3.4b**).

Arch(D95N) reported neuronal action potentials on a single-trial basis (**Fig. 3.4c**). The response to a depolarizing current pulse was dominated by the slow component of the step response, yet the fast component of the response was sufficient to indicate action potentials. Efforts are underway to identify a nonpumping mutant with speed comparable to that of Arch.

3.3 Discussion

We compared Arch and Arch(D95N) to other fluorescent voltage indicators, plotted according to sensitivity and response speed (**Fig. 3.5**; data and references are in **Supplementary Table 3.2**). Data for existing indicators are approximate, and we obtained them from literature. The most sensitive fluorescent proteins, the VSFP 2.x family, have changes in fluorescence of 10% per 100 mV of voltage, with a response time of approximately 100 ms. The sodium channel protein–based ac-

---

[2] I went on to characterize Arch WT outward photocurrents in detail in [62] and found that they exceeded 100 pA. The discrepancy may be explained due to variation in expression levels. Regardless, the photocurrents are sufficient to perturb neural activity.

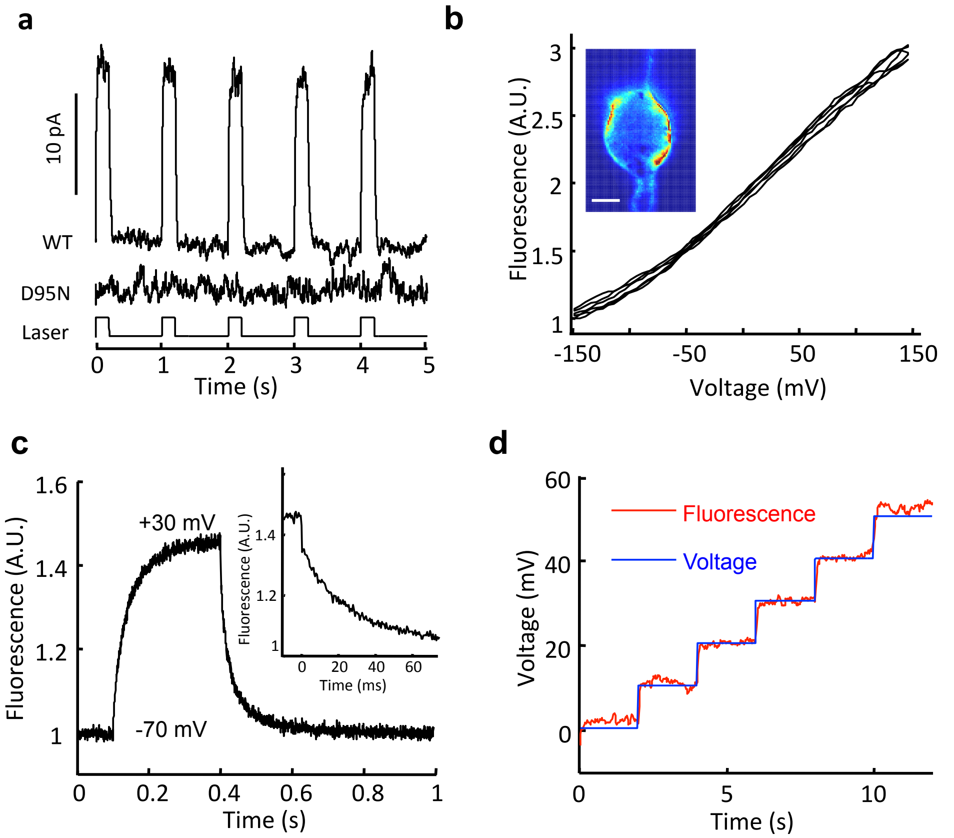

Figure 3.3: Arch(D95N) shows voltage-dependent fluorescence but no photocurrent. (**a**) Photocurrents in Arch and Arch(D95N), expressed in HEK293 cells clamped at V = 0 mV. Cells were illuminated with pulses of light (λ = 640 nm; I = 1,800 W/cm²). (**b**) Fluorescence of Arch(D95N) as a function of membrane potential. Inset, map of voltage sensitivity. Scale bar, 5 μm. (**c**) Dynamic response of Arch(D95N) to steps in membrane potential between −70 mV and +30 mV. Data were averaged over 20 cycles. Inset, step response comprised a component faster than 500 μs (20% of the response) and a component with a time constant of 41 ms. (**d**) Response of Arch(D95N) to 10-mV steps in membrane potential.

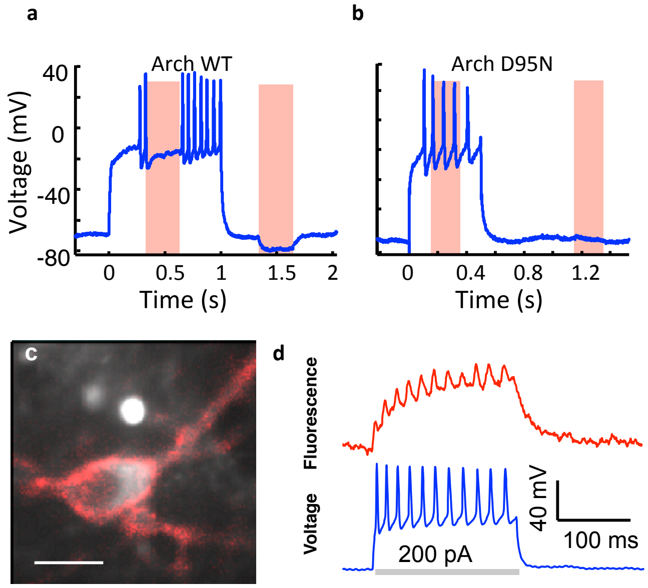

Figure 3.4: Optical recording of action potentials with Arch(D95N). (**a**, **b**) Electrically recorded membrane potential of a neuron expressing Arch (**a**) or Arch(D95N) (**b**), subjected to pulses of current injection and laser (red bars) illumination. (**c**) Fluorescence micrograph of a neuron expressing Arch(D95N), showing Arch(D95N) fluorescence (gray) and regions of voltage-dependent fluorescence (red). Scale bar, 10 μm. (**d**) Single-trial recording of whole-cell membrane potential (blue) and weighted Arch(D95N) fluorescence (red) during a train of action potentials.

tivity reporting construct (SPARC) family of voltage sensors has a 1 ms response time and shows a fluorescence change of <1% per 100 mV. Microbial rhodopsin–based indicators are notably more sensitive than other probes. The most sensitive microbial rhodopsin–based indicator is PROPS, but PROPS only functions in prokaryotes [87]. Fluorescent voltage-sensitive dyes have enabled optical recording of action potentials in brain slices with SNR exceeding that of Arch [121, 129], though phototoxicity and challenges with delivery prevent widespread use.

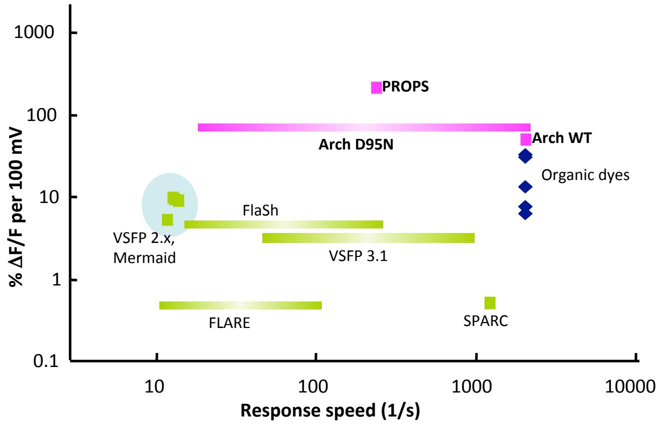

Figure 3.5: Optical indicators of membrane potential classified by speed and sensitivity. Green marks represent indicators based on fusions of GFP homologs to membrane proteins. Pink marks represent indicators based on microbial rhodopsins. Blue diamonds represent organic dyes and hybrid dye-protein indicators. Extended bars denote indicators where two time constants have been reported. PROPS is homologous to Arch(D95N) but only functions in bacteria. The speeds of most organic dyes are not known precisely; but they respond in less than 500 μs.

Arch is one of 5,000 known microbial rhodopsins [163]. We suggest that this family of proteins should be explored for its ability to label biological membranes with a color-tunable, photostable and environmentally-sensitive chromophore, with no homology to GFP. The fluorescence and voltage-sensing properties of microbial rhodopsins are orthogonal to their native biological function, suggesting that these properties can be improved through minor changes to the protein sequence. Screens of wild-type and mutated microbial rhodopsins will be essential for identifying variants that are fast, like Arch, but that lack pumping, like

Arch(D95N). Efforts to increase the brightness or to find other nonfluorescent imaging modalities are also of paramount importance. Initial efforts to observe two-photon fluorescence from Arch were not successful; but the excitation of Arch is red-shifted relative to most two-photon fluorophores, so additional studies with spectrally tuned two-photon excitation are warranted. Simultaneous imaging of fluorescence from Arch and eGFP in a fusion protein may enable ratiometric voltage measurements, with improved robustness to variations in expression or to movement, relative to single-band measurements. Care will be needed to avoid artifacts from environmental and statistical noise in the reference channel as well as from differential photobleaching. Fusions with other fluorescent indicator proteins may enable simultaneous measurements of voltage and pH or Ca^{2+} concentration. We expect the combination of optogenetic voltage measurement with the recently established techniques of optogenetic voltage control [37] to enable progress toward all-optical electrophysiology.

3.4 METHODS

3.4.1 PROTEIN CONSTRUCTS AND MEMBRANE FRACTIONATION

All experiments were performed with an Arch-eGFP fusion. A lentiviral backbone plasmid encoding Arch-eGFP (*FCK-Arch-EGFP*; BAA09452; Addgene plasmid 22217) was used to clone the *Arch* gene into the pet28b vector using the restriction sites EcoRI and NcoI. The sequence encoding the D95N mutation was created separately in the pet28b and FCK backbones, using the QuikChangeII kit (Agilent) and the same DNA primers for both backbones (**Supplementary Table 3.3**).

Arch and its D95N mutant were expressed in *E. coli*, as previously described [14]. Briefly, *E. coli* (strain BL21, pet28b plasmid) was grown in 1 L of LB with 100 μg ml^{1} kanamycin, to an optical density at 600 nm of 0.4 at 37° C. All-trans retinal (5 μM) and inducer (isopropyl β-D-1-thiogalactopyranoside (IPTG), 0.5 mM) were added, and cells were grown for an additional 3.5 h in the dark. Cells were collected by centrifugation and resuspended in 50 mM Tris with 2 mM $MgCl_2$ at pH 7.3 and lysed with a tip sonicator for 5 min. The lysate was centrifuged and the pellet was resuspended in PBS (pH 7.2) supplemented with 1.5% dodecyl maltoside. The mixture was homogenized with a glass and teflon Potter Elvehjem homogenizer and centrifuged again. The solubilized protein in the supernatant was used for experiments.

3.4.2 SPECTROSCOPIC CHARACTERIZATION OF ARCH AND ARCH(D95N)

The absorption spectra of fractionated *E. coli* membranes containing Arch and Arch(D95N) were determined using an Ocean Optics USB4000 spectrometer with a DT-MINI-2-GS light source (**Supplementary Fig. 3.6**). The peak extinction coefficients of microbial rhodopsins vary across rhodopsin types from 48,000 M^{-1} cm^{-1} to 63,000 M^{-1} cm^{-1} (refs. [122, 133, 140, 164]). Owing to the high homology between Arch and bacteriorhodopsin, we used the bacteriorhodopsin extinction coefficient, 63,000 M^{-1} cm^{-1}, for Arch. The differing wavelengths of maximum absorption of Arch (558 nm) and Arch(D95N) (585 nm) led to different extinction coefficients at 633 nm (**Table 3.1**). For Arch, 633 nm was in the tail of the absorption, whereas for Arch(D95N) 633 nm lay half way down the shoulder. The relative extinction coefficients of Arch and Arch(D95N) at

633 nm are independent of our choice to use bacteriorhodopsin as the reference for the peak extinction coefficient. Absorption spectra for Arch and Arch(D95N) were measured as a function of pH between pH 6 and 11.

The fluorescence emission spectra of Arch and Arch(D95N) were determined in bulk samples using illumination with a 100 mW, 532 nm laser (Dragon Lasers, 532GLM100) or a 25 mW, 633 nm HeNe laser (Spectra-Physics) (**Supplementary Fig. 3.6**). Scattered laser light was blocked with a 532 nm Raman notch filter (Omega Optical, XR03) or a 710/100 emission filter (Chroma), and fluorescence was collected perpendicular to the illumination with a 1,000 μm fiber, connected to an Ocean Optics QE65000 spectrometer. Spectra were integrated for 2 s. Arch and Arch(D95N) both had emission maxima at 687 nm. We do not know why the two proteins have such different peak absorption wavelengths but the same peak emission wavelength.

The fluorescence quantum yields of Arch and Arch(D95N) were determined by comparing the integrated emission intensity to emission of a sample of the dye Alexa Fluor 647 (Invitrogen). Briefly, the concentrations of micromolar solutions of dye and protein were determined using a visible absorption spectrum. We used the extinction coefficients of 270,000 M^{-1} cm^{-1} for Alexa Fluor 647 and 63,000 M^{-1} cm^{-1} for Arch and Arch(D95N), assuming that these microbial rhodopsins have the same peak extinction coefficient as bacteriorhodopsin. The dye solution was then diluted 1:1,000 to yield a solution with comparable fluorescence emission to that of Arch. The fluorescence emission spectra of dye and protein samples were measured with 633-nm excitation. The quantum yield (QY) was then determined by the formula

$$QY_{Arch} = \frac{Fl_{Arch}}{Fl_{Alexa}} \times \frac{\epsilon_{Alexa}}{\epsilon_{Arch}} \times \frac{c_{Alexa}}{c_{Arch}} \times QY_{Alexa}$$

where *Fl* is the integrated fluorescence from 660 nm to 760 nm, ϵ is the extinction coefficient at 633 nm, c is the concentration, and Alexa stands for Alexa Fluor 647.

3.4.3 Relative photostability of Arch and eGFP

To directly compare photostability of Arch and eGFP, we studied the photobleaching of the Arch-eGFP fusion. This strategy guaranteed a 1:1 stoichiometry of the two fluorophores, simplifying the analysis. The experiments were performed on permeabilized cells, in the microscope, with video recording as the cells photobleached. We first recorded a movie of photobleaching of Arch under 640-nm illumination; then on the same field of view we recorded photobleaching of eGFP under 488-nm illumination, with illumination intensity adjusted to yield approximately the same initial count rate as for Arch. Fluorescence background levels were obtained from nearby protein-free regions of each movie and were subtracted from the intensity of the protein-containing regions. The area under each photobleaching time trace was calculated, yielding an estimate of the total number of detected photons from each fluorophore. The eGFP emission (λ_{max} = 509 nm) and the Arch emission (λ_{max} = 687 nm) were collected through different emission filters, so the raw counts were corrected for the transmission spectra of the filters and the wavelength-dependent quantum yield of the EMCCD camera. The result was that the relative number of photons emitted before photobleaching for eGFP:Arch was 3.9:1, and for eGFP:Arch(D95N) this ratio was 10:1.

3.4.4 HEK293 CELL CULTURE

HEK293 (HEK) cells were grown at 37° C, 5% CO2, in Dulbecco's modified Eagle medium (DMEM) supplemented with 10% FBS and penicillin-streptomycin. Plasmids were transfected using Lipofectamine and PLUS reagent (Invitrogen) following the manufacturer's instructions, and assayed 48–72 hrs later. The day before recording, cells were replated onto glass-bottom dishes (MatTek) at a density of ~5,000 cells/cm^2.

The concentration of endogenous retinal in the HEK cells was not known, so the cells were supplemented with retinal by diluting stock retinal solutions (40 mM, DMSO) in growth medium to a final concentration of 5 μM and then placing the cells back in the incubator for 1–3 hrs. All imaging and electrophysiology were performed in Tyrode's buffer (containing 125 mM NaCl, 2mM KCl, 3mM $CaCl_2$, 1mM $MgCl_2$, 10mM HEPES,30mM glucose (pH 7.3) and adjusted to 305–310 mOsm with sucrose). Only HEK cells having reversal potentials between −10 mV and −40 mV were included in the analysis.

3.4.5 MICROSCOPY

Simultaneous fluorescence and whole-cell patch-clamp recordings were acquired on a home-built, inverted epifluorescence microscope, operated at room temperature (24° C). Here we summarize the design considerations; a detailed specification is given in **Supplementary Fig. 3.7**. A key challenge was to collect fluorescence with high efficiency while also achieving a large enough field of view to image an entire neuron and its processes. Typically, microscope objectives offer a trade-off between magnification and light-gathering capacity (numerical aperture), which we sought to avoid. Additionally, we wanted the ability to change magnification while maintaining a patch on a single cell. The vibrations associated with switching objectives, particularly water- or oil-immersion objectives, are incompatible with simultaneous patch clamp. Finally, we wanted the capability to split the field of view into two wavelength bands and to change magnification without changing the registration of the two halves of the image.

To achieve these goals simultaneously, we designed our microscope around a 60× numerical aperture (NA) 1.45 oil-immersion objective (Olympus 1-U2B616), with variable zoom camera lenses to change illumination area and magnification. The magnification was continuously variable between 10× and 66×, without touching the objective. The microscope readily converted between single-band and dual-band imaging, with only minor realignment.

On an upright electrophysiology setup retrofitted with a laser and EMCCD camera, a dipping objective (Olympus LUMPlanFl 40× W/IR; NA 0.8) collected enough light to record voltage-dependent fluorescence of HEK cells. However, recording of action potentials with high SNR required a high-NA objective (for example, Olympus 1-U2B893 60× water, NA 1.2 or 1-U2B616 60× oil, NA 1.45).

3.4.6 ELECTROPHYSIOLOGY

Filamented glass micropipettes (WPI) were pulled to a tip resistance of 3–10 MΩ, fire-polished and filled with internal solution (containing 125 mM potassium gluconate, 8 mM NaCl, 0.6 mM $MgCl_2$, 0.1 mM $CaCl_2$, 1 mM EGTA, 10 mM HEPES, 4 mM Mg-ATP, 0.4 mM Na-GTP (pH 7.3); adjusted to 295 mOsm with sucrose). The micropipettes were positioned with a Burleigh PCS 5000 micromanipulator. Whole-cell, voltage-clamp recordings were acquired using an AxoPatch 200B amplifier (Molecular Devices), filtered at 2 kHz with the internal Bessel filter and digitized with a National Instruments PCIE-6323 acquisition board at 10 kHz. Ambient 60 Hz noise was removed using a HumBug Noise Eliminator (AutoMate Scientific). For experiments requiring rapid modulation of transmembrane potential, series resistance and whole-cell capacitance were predicted to 95% and corrected to 50%. Electrical stimuli were generated using the PCIE-6323 acquisition board and sent to the AxoPatch, which then applied these signals in either constant-current or constant-voltage mode.

Measurements of photocurrents were performed on HEK cells held in voltage clamp at 0 mV while being exposed to brief (200 ms) pulses of illumination at 640 nm at an intensity of 1,800 W/cm^2.

All experiments were performed at 24° C.

3.4.7 RAMP AND STEP RESPONSE OF ARCH AND ARCH(D95N)

To measure fluorescence as a function of membrane potential, a triangle wave was applied, with amplitude from −150 mV to +150 mV and period 12 s, with video recording at 100 ms per frame. A pixel weight matrix was calculated according to **Equation 3.2** (see below) and applied to the movie images to generate a fluorescence number for each frame. These fluorescence values were divided by their minimum value (at V = −150 mV). The result is plotted as a function of V in **Figs. 3.2 and 3.3**.

The step response was measured in a similar manner, except that test waveforms consisted of a series of voltage pulses, from −70 mV to +30 mV with duration 300 ms and period 1 s. Cells were subjected to 20 repetitions of the waveform, and the fluorescence response was averaged over all iterations. No background subtraction was applied.

3.4.8 FREQUENCY-DEPENDENT RESPONSE FUNCTIONS OF ARCH AND ARCH(D95N)

Test waveforms consisted of a concatenated series of sine waves, each of duration 2 s, amplitude 100 mV, zero mean and frequencies uniformly spaced on a logarithmic scale between 1 Hz and 1 kHz (31 frequencies total). The waveforms were discretized at 10 kHz and applied to the cell, while fluorescence movies were acquired at a frame rate of 2 kHz.

The model parameters for extracting $\hat{V}_{FL}(t)$ were calculated from the fluorescence response to low frequency voltages. These parameters were then used to calculate an estimated voltage at all frequencies.

The applied voltage was downsampled to 2 kHz to mimic the response of a voltage indicator with instantaneous response. For each applied frequency, the Fourier transform of $\hat{V}_{FL}(t)$ was calculated and divided by the Fourier transform of the downsampled $V(t)$. The amplitude of this ratio determined the response sensitivity. It was crucial to properly compensate pipette resistance and cell membrane capacitance to obtain accurate response spectra. Control experiments on cells expressing membrane-bound eGFP showed no voltage-dependent fluorescence.

The power spectrum of $\hat{V}_{FL}(t)$ under constant V = 0 mV was also measured to enable calculations of SNR for any applied $V(t)$.

3.4.9 ESTIMATES OF MEMBRANE POTENTIALS FROM FLUORESCENCE IMAGES

A common practice in characterizing fluorescent voltage indicators is to report a value of ΔF/F per 100 mV of membrane potential. We feel that this parameter is of limited use, for several reasons. First, the value of ΔF/F is highly sensitive to the method of background subtraction, particularly for indicators in which the value of F approaches zero at some voltage. Second, ΔF/F contains no information about SNR, which depends on absolute fluorescence levels, background, and membrane targeting of the indicator. Third, the ratio ΔF/F contains no information about the temporal stability of the fluorescence. Fluctuations may arise owing to intracellular transport, photobleaching or other photophysics. Fourth, definitions of absolute fluorescence are often subjective, depending on a user-defined region of interest that might or might not include pieces of internal membranes or other cells.

We therefore sought a measure of the performance of a voltage indicator that reported the information content of the fluorescence signal. We sought an algorithm to infer membrane potential from fluorescence images. We used the accuracy with which the estimated membrane potential matched the true membrane potential (as reported by patch clamp recording) as a measure of indicator performance. The algorithm described below is implemented in our analysis.

The estimated membrane potential, $\hat{V}_{FL}(t)$, was determined from the fluorescence in two steps. First we trained a model relating membrane potential to fluorescence at each pixel. We used the highly simplified model that the fluorescence signal, $S_i(t)$, at pixel i and time t, is given by:

$$S_i(t) = a_i + b_i V(t) + \epsilon_i(t) \tag{3.1}$$

where a_i and b_i are position-dependent but time-independent constants, the membrane potential $V(t)$ is time-dependent but position independent, and $\epsilon_i(t)$ is spatially and temporally uncorrelated Gaussian white noise with pixel-dependent variance:

$$\langle \epsilon_i(t_1) \epsilon_j(t_2) \rangle = \sigma_i^2 \delta_{i,j} \delta(t_1 - t_2)$$

where $\langle \rangle$ indicates an average over time.

This model neglects nonlinearity in the fluorescence response to voltage, finite response time of the protein to a change in voltage, photobleaching, cell-motion or stage drift and the fact that if $\epsilon_i(t)$ is dominated by shot-noise then its variance should be proportional to $S_i(t)$, and its distribution should be Poisson, not Gaussian. Despite these simplifications, the model of **Equation 3.1** provided good estimates of membrane potential when calibrated from the same dataset to which it was applied.

The pixel-specific parameters in **Equation 3.1** are determined by a least-squares procedure, as follows. We define the deviations from the mean fluorescence and mean voltage by

$$\delta S_i(t) = S_i(t) - \langle S_i(t) \rangle$$

$$\delta V(t) = V(t) - \langle V(t) \rangle$$

Then the estimate for the slope $\hat{b}_i$ is:

$$\hat{b}_i = \frac{\langle \delta S_i \delta V \rangle}{\delta V^2}$$

and the offset is:

$$\hat{a}_i = \langle S_i \rangle - \hat{b}_i \langle V \rangle$$

A pixel-by-pixel estimate of the voltage is formed from

$$\hat{V}_i(t) = \frac{S_i(t)}{\hat{b}_i} - \frac{\hat{a}_i}{\hat{b}_i}$$

The accuracy of this estimate is measured by

$$\zeta_i^2 = \langle (\hat{V}_i(t) - V(t))^2 \rangle$$

A maximum likelihood weight matrix is defined by:

$$w_i = \frac{1/\zeta_i^2}{\sum_i 1/\zeta_i^2} \tag{3.2}$$

This weight matrix favors pixels whose fluorescence is an accurate estimator of voltage in the training set. To estimate the membrane potential, the pixel-by-pixel estimates are combined according to:

$$\hat{V}_{FL}(t) = \sum_i w_i \hat{V}_i(t) \tag{3.3}$$

Within the approximations underlying **Equation 3.1**, **Equation 3.3** is the maximum likelihood estimate of $V(t)$.

In cases where the membrane potential is not known, one can replace $V(t)$ by the total intensity of the entire image $I(t)$, provided that there is only a single cell with varying membrane potential in the image. In this case, the algorithm preferentially weights pixels whose intensity varies with the mean intensity. Such pixels are associated with the membrane. This modified procedure yields an estimate of the underlying intensity variations in the membrane. The output resembles the true membrane potential, apart from an unknown offset and scale factor. A key feature of this modified procedure is that it enables spike identification without a patch pipette.

On a video record of 30,000 frames taken (for example, 30 s of data at 1,000 frames s^1), the training phase of the algorithm took approximately 3 min to run on a desktop PC. Application of the weighting coefficients to incoming video data could be performed in close to real time. Small shifts in the field of view owing to stage drift or bumps of the apparatus are compensated by using image registration techniques to translate the pixel weight map. Large changes in focus or movement to a new field of view required retraining of the algorithm.

3.4.10 MOLECULAR BIOLOGY AND VIRUS PRODUCTION

Plasmids encoding Arch-eGFP (*FCK-Arch-eGFP*) were either used directly for experiments in HEK cells or first used to produce VSVg-pseudotyped virus according to published methods [27]. For pseudotyping, HEK cells were transfected together with pDelta 8.74, VSVg and either of the Arch backbone plasmids using Lipofectamine and PLUS reagent. Viral supernatants were collected 48 h later and filtered using a 0.45-μm membrane. The virus medium was used to infect neurons without additional concentration.

3.4.11 NEURONAL CELL CULTURE

Embryonic day 18 (E18) rat hippocampi (BrainBits) were mechanically dissociated in the presence of 1 mg/ml papain (Worthington) before plating at 5,000–30,000 cells per dish on poly(l-lysine) and Matrigel-coated (BD Biosciences) glass-bottom dishes. At this density synaptic inputs did not generate spontaneous firing. Cells were incubated in N+ medium (100 ml Neurobasal medium, 2 ml B27 supplement, 0.5 mM glutamine, 25 μM glutamate and penicillin-streptomycin) for 3 hrs. An additional 300 μl virus medium was added to the cells and incubated overnight, then brought to a final volume of 2 ml N+ medium. After 2 d, cells were fed with 1.5 ml N+ medium. Cells were fed with 1 ml N+ medium without glutamate at 4 days in vitro (DIV), and fed 1 ml every 3–4 d after. Cells were allowed to grow until 10–14 DIV. Cells were supplemented with retinal by diluting stock retinal solutions (40 mM, DMSO) in growth medium to a final concentration of 5 μM, and then placing the cells back in the incubator for 1–3 h, after which they were used for experiments.

Whole-cell current clamp recordings were obtained from neurons under the same conditions used for HEK cells recordings. Series resistance and pipette capacitance were corrected. Only neurons with resting potentials between −50 mV and −70 mV were used in the analysis.

3.4.12 SPIKE SORTING

We used a simple spike identification algorithm that could be applied either to electrically recorded $V(t)$ or to optically determined $\hat{V}_{FL}(t)$. The input trace was convolved with a reference spike. Sections of the convolved waveform that crossed a user-defined threshold were identified as putative spikes. Multiple spikes that fell within 10 ms (a consequence of noise-induced glitches near threshold) were clustered and identified as one.

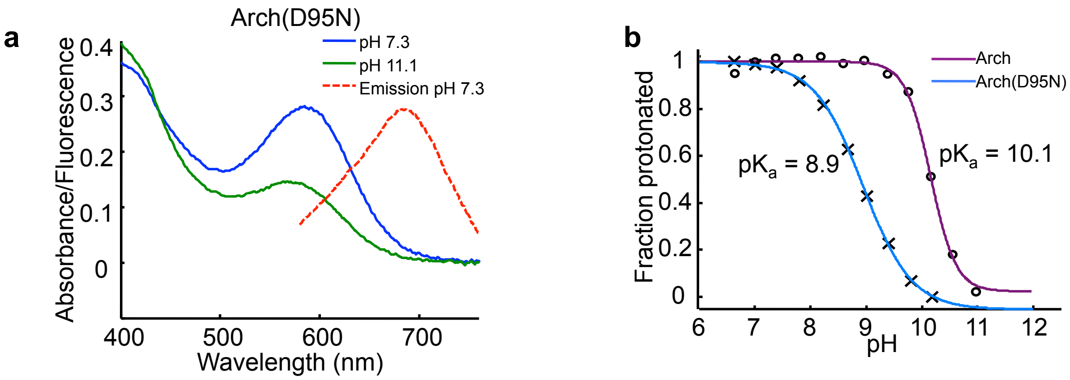

Figure 3.6: pH-dependent spectra of Arch and Arch(D95N). (**a**) Arch(D95N) absorption at neutral (blue) and high (green) pH. At neutral pH, Arch(D95N) absorbed maximally at 585 nm. Fluorescence emission (red dashed line) was recorded on 2 μM protein solubilized in 1% DM, with $\lambda_{exc} = 532$ nm. (**b**) Absorption spectra were recorded on solubilized protein between pH 6 – 11. Singular Value Decomposition of absorption spectra between 400 – 750 nm was used to calculate the fraction of the SB in the protonated state as a function of pH. The result was fit to a Hill function to determine the pK_a of the SB.

Figure 3.7 ***(following page)*****: Diagram of fluorescence microscope. Illumination sources**: S1 – 488 nm, 60 mW (Omicron PhoxX). S2 – 640 nm, 100 mW (CrystaLaser, DL638-100-O, ultra-stable option). **Dichroic mirrors**: D1 - 405/488/561/635 quad pass (Semrock). D2, D3 - 662 long pass, imaging flatness (Semrock). D4 - 503 long pass (Semrock). **Broadband mirrors**: M1, M2 and M3 are Θ2" broadband dielectic mirrors. All other mirrors shown are Θ1". **Fixed lenses** (all achromatic doublets): L1 - Θ1" f = 25 mm, L2 - Θ1" f = 60 mm, L3 - Θ2" f = 150 mm, L4, L6, L7, L8, L9 - Θ2" f = 100 mm, L5 - Θ1" f = 100 mm. **Filters**: F1 - 700/75 bandpass (Chroma). F2 - 580/60 bandpass (Chroma). **Zoom lenses**: Z1 - 18-200 mm f/3.5-6.3 (Sigma). Z2 - 18-200mm f/3.6-5.6 (Nikon). **Objective**: Olympus 1-U2B616 60X oil NA 1.45.

Wide-field illumination was provided by diode lasers S1 and S2. A variable zoom camera lens, Z1, set the beam diameter entering the microscope, and thereby the diameter and intensity of the illumination spot (50 - 500 μm; 40 – 4000 W/cm²). A quad-band dichroic mirror, D1, enabled simultaneous illumination at 640 nm and 488 nm, with collection at other wavelengths. To minimize background from out-of-focus debris, illumination was often performed in through-the-objective total internal reflection fluorescence (TIRF) mode, although in the absence of debris conventional epifluorescence illumination provided similar signal-to-noise ratio. A mirror, M1, placed 1f away from the wide-field lens, L4, enabled switching between TIRF and epifluorescence modes.

Fluorescence emission was collected through the same objective, passed through the dichroic mirror, and re-imaged through a second variable zoom camera lens, Z2, onto an adjustable slit. The image was split by a dichroic mirror, D2, passed through emission filters (F1 for Arch fluorescence and F2 for eGFP fluorescence), recombined on a second dichroic mirror, D3, and imaged onto an EMCCD camera. For fast imaging of dynamic fluorescence responses and APs, images were acquired on an Andor iXon$^+$ 860 EMCCD operating at up to 2,000 frames/s (using a small region of interest and pixel binning). Slower images with higher spatial resolution were acquired on an Andor iXon$^+$ 897 EMCCD. Custom software written in LabView (National Instruments) was used to synchronize illumination, collection of images, recording of membrane potential and cell current, and application of electrical stimuli to the cell.

Figure 3.7: (continued)

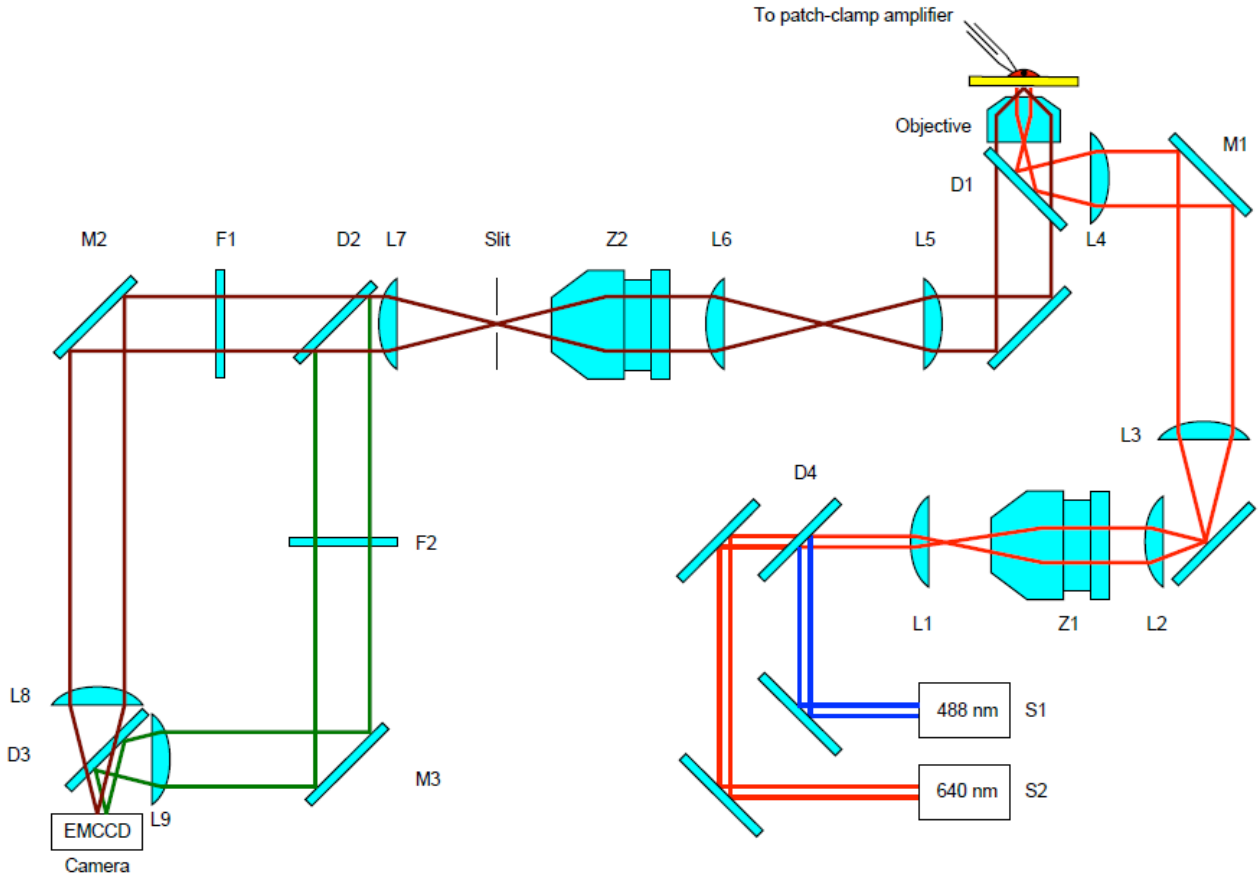

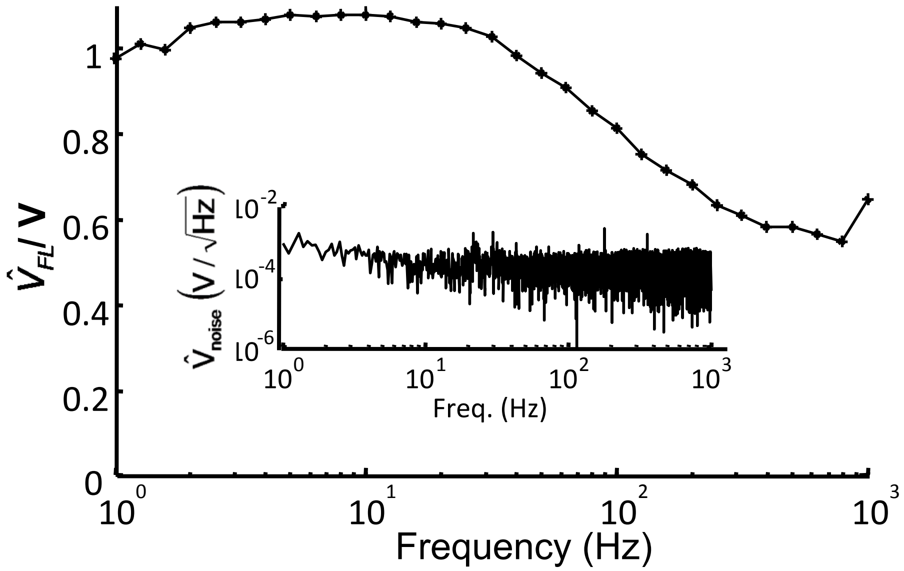

Figure 3.8: Frequency response of Arch. A chirped sine wave with amplitude 50 mV and frequency from 1 Hz – 1 kHz was applied to the cell. Membrane potential $\hat{V}_{FL}$ was determined from fluorescence and the Fourier transform of $\hat{V}_{FL}$ was calculated. The uptick at 1 kHz is an artifact of electronic compensation circuitry. Inset: power spectrum of noise in $\hat{V}_{FL}$, under voltage clamp at constant V = 0 mV shows a shot-noise limited noise floor of 470 μV/(Hz)$^{1/2}$ at frequencies above 10 Hz. The noise figures reported here are specific to our imaging system and serve primarily as an indicator of the possible sensitivity of Arch.

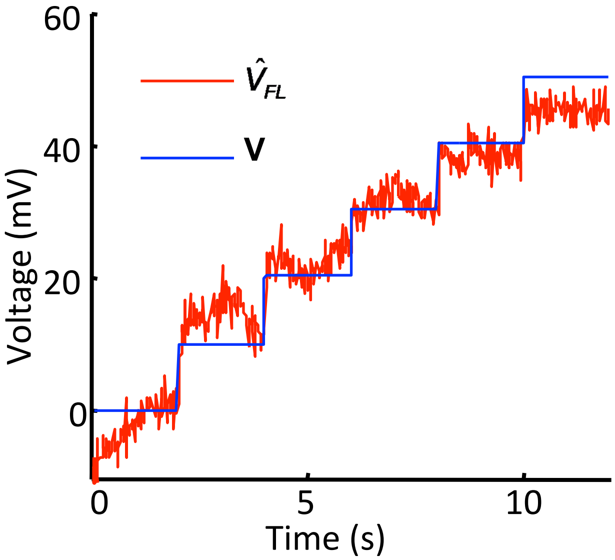

Figure 3.9: Sensitivity of Arch to voltage steps of 10 mV. Whole-cell membrane potential determined via direct voltage recording, V, (blue) and weighted Arch fluorescence, $\hat{V}_{FL}$, (red).

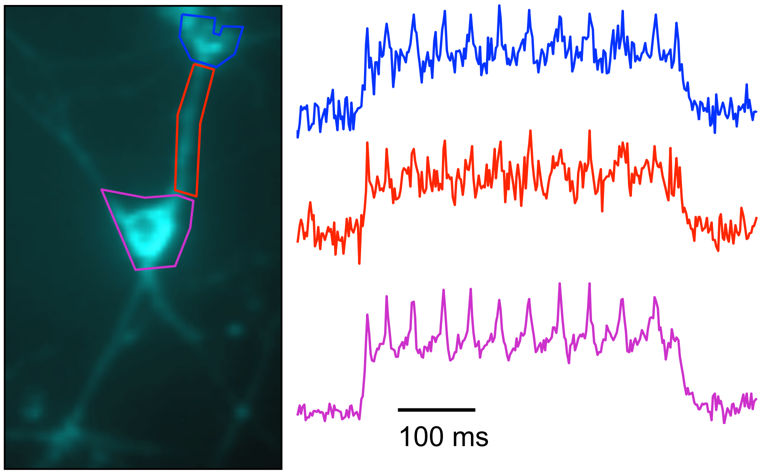

Figure 3.10: Sub-cellular localization of action potentials on a single-trial basis. The vertical scale on the fluorescence traces is arbitrary. The lower regions of the cell, shown in **Fig. 2e**, did not have adequate SNR to indicate APs on a single-trial basis.

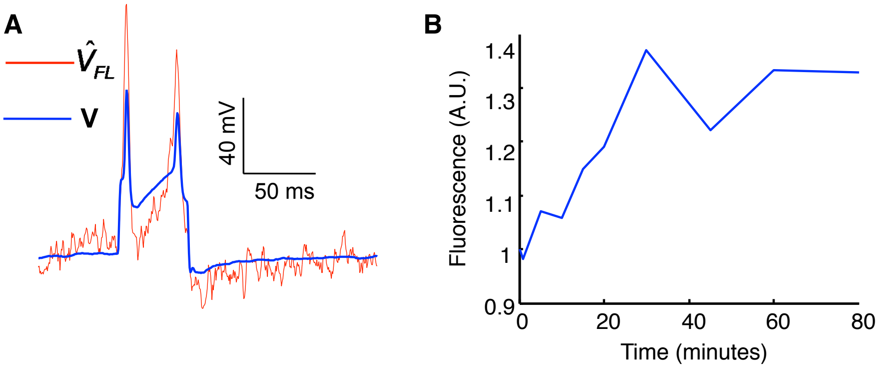

Figure 3.11: Arch reports action potentials without exogenous retinal. A) Single-trial recording of APs from a 14 DIV neuron expressing Arch, without exogenous retinal, showing electrical (blue) and fluorescence (red) traces. APs are clearly resolved. **B**) Fluorescence of a single neuron as a function of time after addition of 10 μM retinal. To avoid conflation of voltage dynamics with the effects of retinal incorporation, the neuron was depolarized by treatment with CCCP prior to the experiment.

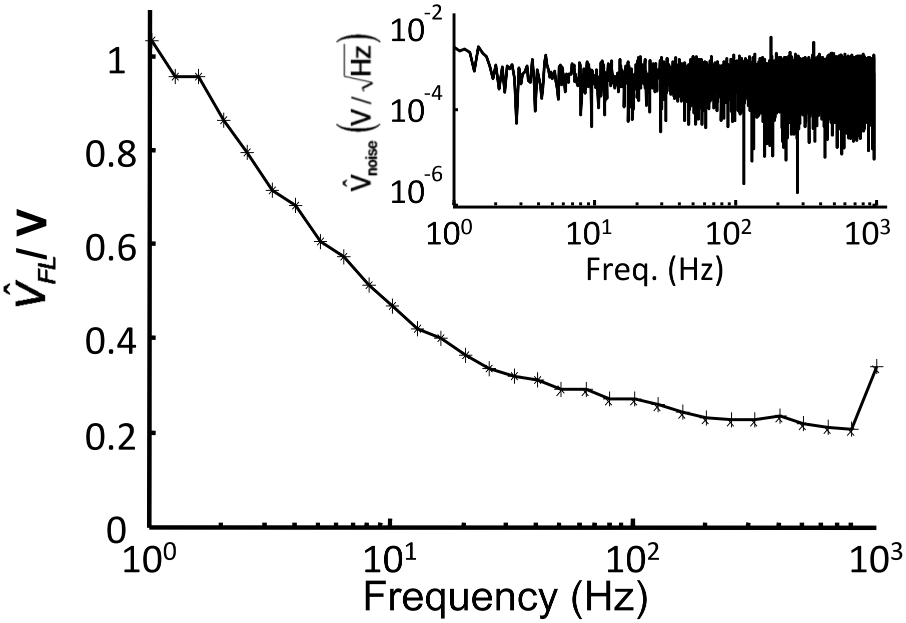

Figure 3.12: Frequency response of Arch(D95N). measured in the same manner as for Arch (**Supplementary Fig. 3.8**).

3.6 SUPPLEMENTARY TABLES

Table 3.2: Approximate characteristics of fluorescent voltage indicating proteins. Characteristics were compiled from Refs. [4, 7, 20, 41, 42, 49, 52, 83, 87, 101, 113, 126, 147, 148]. In some cases numbers were estimated from published plots. The table contains representative members of all families of fluorescent indicators but omits many.

Molecule	Approx ΔF/F per 100 mV	Approx response time	Comments
VSFP 2.3	9.50%	78 ms	Ratiometric (ΔR/R)
VSFP 2.4	8.90%	72 ms	Ratiometric (ΔR/R)
VSFP 3.1	3%	1-20 ms	Protein
Mermaid	9.20%	76	Ratiometric (ΔR/R)
SPARC	0.50%	0.8 ms	Protein
FlaSh	5.10%	2.8 – 85 ms	Protein
Flare	0.50%	10 – 100 ms	Protein
PROPS	150%	5 ms	Protein
di-4-ANEPPS	8%	< 1 ms	Dye
di-8-ANEPPS	10%	< 1 ms	Dye
RH237	11%	< 1 ms	Dye
RH421	21%	< 1 ms	Dye
ANNINE-6plus	30%	< 1 ms	Dye
hVOS	34%	< 1 ms	hybrid
DiO/DPA	56%	< 1 ms	hybrid

Table 3.3: Primers used for mutagenesis, cloning, and sequencing.

Arch D95N forward primer	TTATGCCAGGTACGCCAACTGGCTGTTTACCAC
Arch D95N reverse primer	GTGGTAAACAGCCAGTTGGCGTACCTGGCATAA
Arch to pet28 forward primer	GATTAGCCATGGACCCCATCGCTCTG
Arch to pet28 reverse primer	CATATCGAATTCGCCTTGTACAGCTC
pet28 sequence primer	TAA TAC GAC TCA CTA TAG GG
FCK sequence primer	GCTCGTCAATCAAGCTGGTTC

3.7 SUPPLEMENTARY MOVIES

3.7.1 SUPPLEMENTARY MOVIE

`http://www.nature.com/nmeth/journal/v9/n1/extref/nmeth.1782-S2.avi`

Fluorescence from an HEK cell expressing Arch. The cell was subjected to steps in voltage from −100 mV to 100 mV at 1 Hz. The apparent voltage-sensitive pixels inside the cell are due to out-of-focus fluorescence from the upper and lower surfaces of the plasma membrane. Images are unmodified raw data. Movie is shown in real time.

3.7.2 SUPPLEMENTARY MOVIE

`http://www.nature.com/nmeth/journal/v9/n1/extref/nmeth.1782-S3.avi`

Fluorescence from a rat hippocampal neuron expressing Arch, showing single-trial detection of action potentials. The field on the left shows the time-averaged fluorescence; the field on the right shows deviations from the time average. Movie has been slowed 25-fold.

3.7.3 SUPPLEMENTARY MOVIE

`http://www.nature.com/nmeth/journal/v9/n1/extref/nmeth.1782-S4.avi`

Fluorescence from a rat hippocampal neuron expressing Arch, averaged over n = 98 action potentials. Note the delayed rise and fall of the action potential in the small protrusion coming from the process at 7 o'clock relative to the cell body. The time-averaged fluorescence from the cell has been subtracted to highlight the change in fluorescence during an action potential. The background, in gray, shows the time-averaged image.

3.7.4 SUPPLEMENTARY MOVIE

`http://www.nature.com/nmeth/journal/v9/n1/extref/nmeth.1782-S5.avi`

Fluorescence from a HEK cell expressing Arch(D95N) subjected to steps in voltage from −100 mV to 100 mV at 1 Hz. The apparent voltage-sensitive pixels inside the cell are due to out-of-focus fluorescence from the upper and lower surfaces of the plasma membrane. Images are unmodified raw data. Movie is shown in real time.

3.7.5 SUPPLEMENTARY MOVIE

`http://www.nature.com/nmeth/journal/v9/n1/extref/nmeth.1782-S6.avi`

Fluorescence from a HEK cell expressing Arch(D95N) subjected to a voltage-clamp triangle wave from −150 mV to 150 mV. The apparent voltage-sensitive pixels inside the cell are due to out-of-focus fluorescence from the upper and lower surfaces of the plasma membrane. The movie is sped up threefold. Images are unmodified raw data.

3.8 MANUSCRIPT INFORMATION

3.8.1 PREVIOUSLY PUBLISHED AS

A version of this chapter appeared in [88]:

J. M. Kralj*, A. D. Douglass*, D. R. Hochbaum*, D. Maclaurin, and A. E. Cohen. Optical recording of action potentials in mammalian neurons using a microbial rhodopsin. *Nature Methods*, 9(1):90–95, 2012.

3.8.2 ACKNOWLEDGEMENTS

We thank F. Engert (Harvard University) for generously providing support to A.D.D., providing laboratory space during the early stages of this work, and for facilitating this collaboration, E. Boyden (Massachusetts Institute of Technology), K. Rothschild (Boston University) and A. Ting (Massachusetts Institute of Technology) for discussions and contributions of equipment and reagents, and G. Lau, B. Lilley and H. Inada for technical assistance. This work was supported by the Harvard Center for Brain Science, US National Institutes of Health grants 1-R01-EB012498-01 and New Innovator grant 1-DP2-OD007428, the Harvard–Massachusetts Institute of Technology Joint Research Grants Program in Basic Neuroscience, an Intelligence Community postdoctoral fellowship (J.M.K.), a National Science Foundation Graduate Fellowship (D.R.H.), a Helen Hay Whitney Postdoctoral Fellowship (A.D.D.) and Charles A. King Trust Postdoctoral Fellowship (A.D.D.).

3.8.3 THE AUTHOR'S CONTRIBUTION

Daniel R Hochbaum, Joel M Kralj, and Adam D Douglass contributed equally to this work. Adam E Cohen conceived the project. Daniel R Hochbaum, Joel M Kralj, Adam D Douglass carried out experiments. Dougal Maclaurin designed and built the imaging system used in **Figure 3.2**. All authors designed experiments, analyzed data and wrote the paper.

4

All-optical electrophysiology in mammalian neurons using engineered microbial rhodopsins

4.1 INTRODUCTION

TO DISENTANGLE THE COMPLEX INTERACTIONS underlying neural dynamics, one would like to visualize membrane voltage across spatial scales, from single dendritic spines to large numbers of interacting neurons, while delivering spatially and temporally precise stimuli [125, 128]. Optical methods for simultaneous perturbation and measurement of membrane potential could achieve this goal [139].

One would further like to target the stimulation and recording to genetically specified cells. Genetic targeting is particularly important in intact tissue where closely spaced cells often perform distinct functions. Genetic targeting is also valuable *in vitro*, for characterizing heterogeneous cultures that arise during stem cell differentiation to neurons [18], or while studying neurons co-cultured with other cell types.

Optical stimulation has been demonstrated with glutamate uncaging [44], photoactivated ion channel agonists [89], and microbial rhodopsin actuators [19]. Genetically encoded functional readouts include reporters of intracellular Ca2+ and membrane voltage [99]. Voltage-sensitive dyes offer good speed, sensitivity, and spectral tuning [112, 168], but cannot be delivered to a genetically specified subset of cells and often suffer from phototoxicity.

Optical stimulation has been paired with voltage imaging [45, 94, 159, 165]. However, robust and cross-talk-free genetically targeted all-optical electrophysiology has not been achieved due to limitations on the speed and sensitivity of genetically encoded voltage indicators (GEVIs), and spectral overlap between existing GEVIs and optogenetic actuators. GFP-based GEVIs experience severe optical crosstalk with even the most red-shifted channelrhodopsins, which retain ~20% activation with blue light excitation [82]. There remains a need for sensitive, fast, and spectrally orthogonal tools for genetically targeted simultaneous optical perturbation and measurement of membrane voltage.

Here we introduce variants of a near-infrared archaerhodopsin-based voltage indicator and a blue light gated channelrhodopsin actuator which individually show greatly improved performance relative to published optogenetic tools and which together constitute a tool for all-optical electrophysiology. First, we characterize the optical and electrophysiological properties of the indicator, the actuator, and the co-expressed pair (Optopatch) and compare against published tools. Second, we use Optopatch to probe neuronal excitation across spatial and temporal scales: from single dendritic spines to fields containing dozens of neurons measured in parallel, and from microsecond delays associated with action potential propagation to days-long changes in excitability. Third, we apply Optopatch to study excitability in human induced pluripotent stem cell (hiPSC)-derived neurons. These measurements revealed the first evidence for homeostatic plasticity of intrinsic excitability in hiPSC-derived neurons. Fourth, we apply Optopatch in tissue. In organotypic brain slice, Optopatch initiates and reports action potentials and subthreshold dynamics with higher signal-to-noise ratios, better photostability, and better time resolution than ArcLight, a recently introduced GFP-based GEVI [75].

4.2 RESULTS

4.2.1 DIRECTED EVOLUTION OF AN ARCH-BASED VOLTAGE INDICATOR

We previously showed that Archaerhodopsin 3 (Arch) functions as a fast and sensitive voltage indicator [88]. Arch has the furthest red-shifted spectrum of any GEVI, giving it the unique property of little spectral overlap with channelrhodopsin actuators and GFP-based reporters. Thus it is natural to pair Arch-based indicators with optogenetic actuators for crosstalk-free all-optical electrophysiology.

However, wild-type Arch had some undesirable attributes for a reporter: it was very dim, and the brightness was a nonlinear function of illumination intensity [103]. Illumination for imaging generated a hyperpolarizing photocurrent, which partially suppressed neural firing. The mutant Arch(D95N) did not pump, but its step response was dominated by a 41 ms time constant, too slow to resolve action potential (AP) waveforms. Other non-pumping mutants improved speed relative to Arch(D95N) but did not reach the speed of wild-type Arch and did not address the low brightness [45].

We sought to repair these defects in engineered mutants of Arch. To accommodate the multiple selection criteria, we adopted a hierarchical screen (**Fig. 4.1a**). Five rounds of brightness screening in *E. coli* and random mutagenesis on a library of $> 10^4$ Arch mutants resulted in a brighter Arch variant, containing 5 point-mutations (**Methods Section 4.4**). Further site-directed mutagenesis at known key residues improved voltage sensitivity and speed (**Supplementary Fig. 4.6**), while addition of an endoplasmic reticulum export motif and a trafficking sequence improved trafficking (**Methods Section 4.4**). The two most promising mutants were named QuasArs (Quality superior to Arch). QuasAr1 comprised mutations P60S, T80S, D95H, D106H, F161V and QuasAr2 comprised QuasAr1(H95Q). Both proteins had fluorescence excitation maxima at 590 nm and emission maxima at 715 nm (**Supplementary Fig. 4.7**). The fluorescence quantum yields of solubilized QuasAr1 and 2 were 19- and 10-fold enhanced, respectively, relative to the non-pumping voltage indicator Arch(D95N) (**Supplementary Table 4.1**). All fluorescence microscopy of QuasArs used 640 nm excitation.

We compared the fluorescence, voltage sensitivity, and speed of the QuasArs to wild-type Arch in HEK cells, using epifluorescence microscopy and whole-cell patch clamp electrophysiology. Under low intensity illumination (500 mW/cm^2), QuasAr1 was 15-fold brighter than wild-type Arch, and QuasAr2 was 3.3-fold brighter (**Fig. 4.1b**; **Methods Section 4.4**). Neither mutant showed the optical nonlinearity seen in the wild-type protein, implying that fluorescence was a 1-photon process with the voltage-sensitive transition occurring from the ground state. At high intensity (> 100 W/cm^2) QuasAr1 was 2.5-fold brighter than wild-type Arch, while the brightness of QuasAr2 and of wild-type Arch were comparable.

Fluorescence of Arch, QuasAr1, and QuasAr2 increased nearly linearly with membrane voltage between -100 mV and +50 mV (**Fig. 4.1c**, **Methods Section 4.4**). Sensitivities were (ΔF/F per 100 mV): 32 ± 3% for QuasAr1 (n = 5 cells; all statistics are mean ± s.e.m. unless specified) and 90 ± 2% for QuasAr2 (n = 6 cells). The sensitivity of QuasAr2 is a substantial improvement over both Arch (40% per 100 mV) and Arch(D95N) (60% per 100 mV).

Steps in membrane voltage (-70 mV to +30 mV) induced rapid fluorescence responses in both mutants, which we quantified on a fast photomultiplier (**Fig. 4.1d**). At room temperature (23 °C) QuasAr1 had a step response time constant of 0.053 ± 0.002 ms (n = 6 cells), close to the 0.05 ms time resolution of the electronics and substantially faster than the 0.6 ms step response of wild-type Arch [103]. QuasAr2 had a bi-exponential step response with time constants of 1.2 ± 0.1 ms (68%) and 11.8 ± 1.5 ms (32%) (n = 6 cells). At 34 °C, the apparent speed of QuasAr1 remained at the 0.05 ms resolution of the electronics, and the time constants of QuasAr2 decreased to 0.30 ± 0.05 ms (62%) and 3.2 ± 0.4 ms (38%) (n = 7 cells). Both mutants had similar response times on rising and falling edges (**Supplementary Table 4.2**). Neither QuasAr1 nor QuasAr2 generated detectable steady-state photocurrent under red light (tested up to 900 W/cm^2) or blue light (**Supplementary Fig. 4.8**).

We expressed QuasArs in cultured rat hippocampal neurons, evoked APs and recorded the fluorescence responses from the soma and proximal dendrites (1 kHz frame rate, **Fig. 4.1e-h**, **Supplementary Fig. 4.9**). Single APs produced fluorescence transients with amplitude ΔF/F = 21 ± 2% for QuasAr1 (n = 11 cells) and

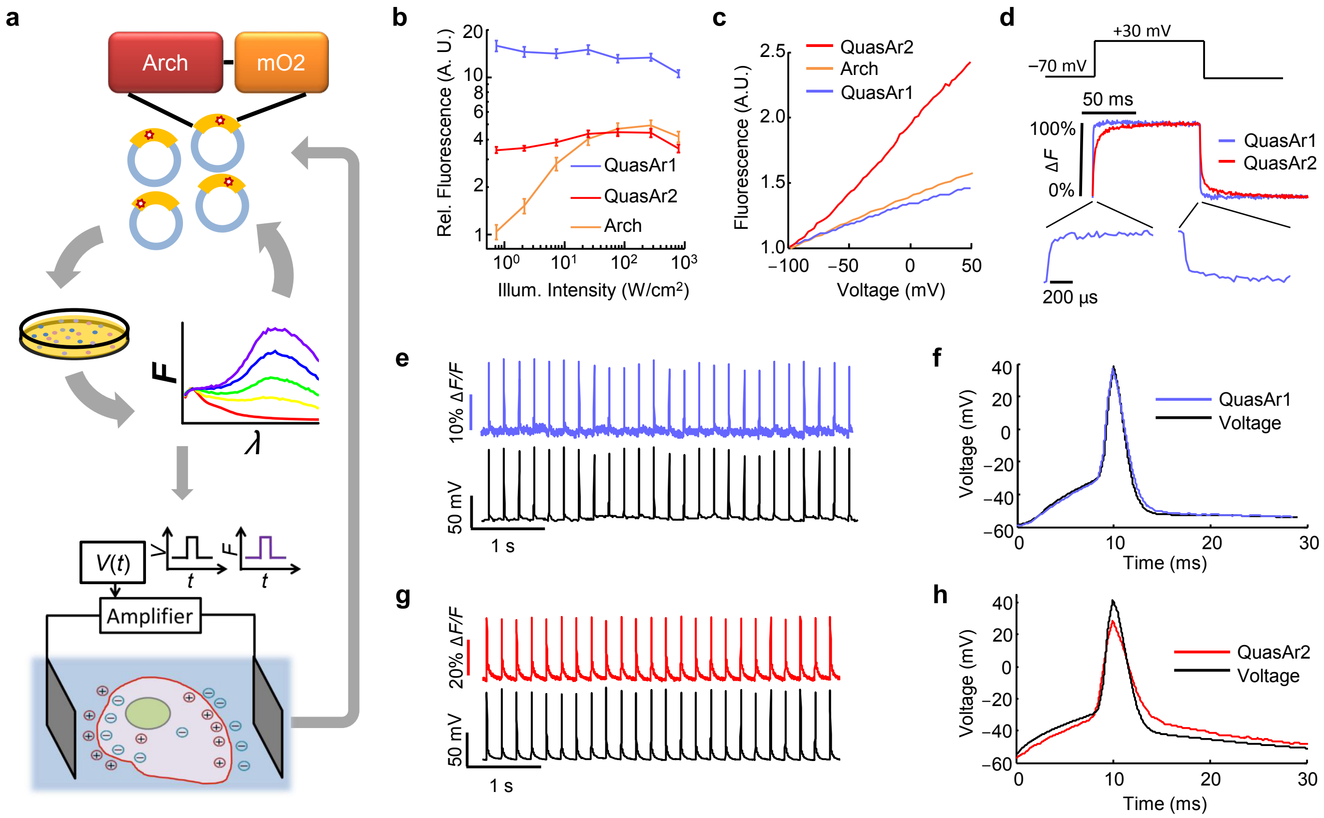

Figure 4.1: Non-pumping Arch-derived voltage indicators with improved speed, sensitivity, and brightness. (**a**) Hierarchical screen to select improved Arch mutants. Five rounds of random mutagenesis and screening for brightness were performed in E. coli. The brightest mutants were subjected to targeted mutagenesis and screening for speed and voltage sensitivity in HeLa cells via induced transient voltage (**Supplementary Fig. 4.6**). (**b**) Fluorescence of Arch mutants fused to eGFP and expressed in HEK cells, as a function of illumination intensity. The plot shows Arch fluorescence normalized by 640 nm illumination intensity and by eGFP fluorescence (488 nm exc., 525 – 575 nm em.) to control for cell-to-cell variations in expression. A linear fluorophore (i.e. brightness proportional to illumination intensity) would appear as a horizontal line. Error bars represent s.e.m. (n = 7 cells for each mutant). (**b**) Fluorescence vs. membrane voltage for Arch, QuasAr1, and QuasAr2 expressed in HEK cells. (**d**) Fluorescence responses to a step in membrane voltage from -70 to +30 mV. (**e**) Simultaneous optical and electrical recording of APs in a rat hippocampal neuron expressing QuasAr1. Frame rate 1 kHz. (**f**) Overlay of mean optically and electrically recorded AP waveforms. Frame rate 2 kHz. (**g, h**), Same as **e**, **f** in neurons expressing QuasAr2. Data in **b** – **h** acquired on a 128 x 128 pixel EMCCD camera (**Methods Section 4.4**).

ΔF/F = 48 ± 3% for QuasAr2 (n = 24 cells). Signal-to-noise ratios (SNRs) for single APs increased with illumination intensity. For QuasAr1, SNR values were 21 ± 2 (300 W/cm^2, n = 6 cells) and 32 ± 4 (800 W/cm^2, n = 6 cells). For QuasAr2, SNR values were 41 ± 4 (300 W/cm^2, n = 12 cells) and 70 ± 8 (800 W/cm^2, n = 12 cells). These SNRs correspond to equivalent electrical noise levels of 3.0 to 4.3 mV (800 to 300 W/cm^2) for QuasAr1, or 1.5 to 2.2 mV (800 to 300 W/cm^2) for QuasAr2 (**Methods Section 4.4**).

QuasAr1 did not introduce detectable broadening in the optically recorded AP waveform, acquired at a 2 kHz frame rate (**Fig. 4.1f**). At room temperature, QuasAr2 broadened the optically recorded AP by 650 ± 150 μs relative to the simultaneously recorded electrical waveform at 70% maximum depolarization (n = 5 cells; mean ± s.d.) (**Fig. 4.1h**). At 34 °C, QuasAr2 broadened the optically recorded AP by 180 ± 120 μs (n = 5 cells; mean ± s.d). Both probes reported AP peak times with < 100 μs jitter relative to simultaneously acquired patch clamp recordings (**Methods Section 4.4**).

Photostability is a concern with any voltage indicator, so we quantified the stability of QuasArs under continuous illumination at standard imaging intensity (300 W/cm^2). Photobleaching time constants were 440 s for QuasAr1 and 1020 s for QuasAr2. We further tested for red light-induced phototoxicity using QuasAr2 as the readout. Under continuous illumination at 300 W/cm^2, QuasAr2 reported APs with 100% fidelity for the 30 min duration of the experiment, with no detectable change in AP width or waveform (**Supplementary Fig. 4.10**).

We compared the QuasArs to ArcLight A242 [75]. Photophysical comparisons were performed in HEK cells (**Supplementary Table 4.2**), and action potential comparisons were performed in matched neuronal cultures (**Methods Section 4.4**). ArcLight can be imaged with ~30-fold lower illumination intensity than is required for the QuasArs, facilitating measurements on readily available microscope systems. However, the QuasArs reported action potentials with 7 to 16-fold larger fractional fluorescence changes, 3 to 8-fold higher SNR, 30 to 1000-fold higher temporal resolution, and 6 to 15-fold greater photostability (**Supplementary Fig. 4.11**).

The QuasArs represent, to our knowledge, the fastest and most sensitive GEVIs reported to-date. The 50 μs response time of QuasAr1 is more than 10-fold faster than the fastest previously reported GEVIs [103, 136] and is comparable to fast voltage-sensitive dyes. QuasAr1 opens the possibility of accurate mapping of AP waveforms for even the fastest-spiking neurons [11]. The QuasArs report voltage with greatly improved sensitivity and time resolution compared to the first generation of Arch-based GEVIs, despite requiring ~5-fold lower illumination intensity [88]. From a signal-to-noise perspective, QuasAr2 is superior to QuasAr1: the greater voltage sensitivity of QuasAr2 outweighs the greater brightness of QuasAr1. From a temporal resolution perspective, QuasAr1 is superior. We recommend QuasAr2 for spike counting and measurement of sub-threshold events, and QuasAr1 for measurement of microsecond-precision AP waveforms and timing. Furthermore, the far red excitation of the QuasArs allows, in principle, combination with channelrhodopsin actuators or other GFP-based reporters.

4.2.2 CheRiff, a sensitive blue-shifted optogenetic actuator

We next sought to combine the QuasAr reporters with a blue light-activated channelrhodopsin. To achieve spatially precise optical excitation, the channelrhodopsin should trigger APs when only a subsection of a cell is excited. Existing optogenetic actuators have had only marginal success in achieving this goal [143]. To avoid optical cross-talk, the blue light intended for the channelrhodopsin should not perturb the GEVI fluorescence. Existing optogenetic actuators require blue light intensities that perturb QuasAr fluorescence (**Supplementary Fig. 4.12**). We thus sought a more sensitive channelrhodopsin that could reliably trigger APs with sub-cellular illumination and at lower light intensity, while maintaining fast opening and closing kinetics.

During a screen of plant genomes [76] we identified a novel optogenetic actuator, *Scherffelia dubia* ChR (sdChR) [82], derived from a fresh-water green alga first isolated from a small pond in Essex, England (**Supplementary Fig. 4.13**) [110]. SdChR had promising sensitivity and a blue action spectrum (I_{max} = 474 nm). Addition of a trafficking sequence improved membrane targeting (**Supplementary Fig. 4.13**). Introduction of the mutation E154A sped the kinetics and shifted the peak of the action spectrum to I_{max} = 460 nm (**Fig. 4.2a**), which decreased spurious channelrhodopsin activation by red light (**Supplementary Fig. 4.14, Supplementary Table 4.3**). We dubbed the final construct CheRiff in reference to *Scherffelia*, its genus of origin. CheRiff showed good expression and membrane trafficking in cultured rat hippocampal neurons (**Fig. 4.2b**).

Under typical neural culture conditions, rapid and robust AP initiation requires currents of approximately 1 nA (ref. [108]). In a paired comparison, CheRiff passed a photocurrent of 1 nA at a whole-cell illumination intensity of 22 ± 10 mW/cm^2 (n = 5 neurons), 9-fold lower than was required for ChR2 H134R (200 ± 80 mW/cm^2, n = 5 neurons) (**Fig. 4.2c**). For stimulation localized to the soma, CheRiff passed a photocurrent of 1 nA under illumination at 100 mW/cm^2, while ChR2 H134R did not achieve this photocurrent under any illumination intensity. Upon pulsed whole-cell illumination, CheRiff induced high-frequency and high-reliability spike trains (**Fig. 4.2d**) at five to ten-fold lower illumination intensities than have been reported for ChR2 H134R, ChIEF, or ChETA [108] using the same protocol.

We measured the photophysical properties of CheRiff, ChR2 H134R and ChIEF [95] in matched neuronal cultures (**Supplementary Fig. 4.14, Supplementary Table 4.4**). CheRiff showed 2-fold larger maximal photocurrents than ChR2 H134R or ChIEF. CheRiff had an opening rate 2-fold faster than ChR H134R and 4-fold faster than ChIEF. CheRiff had a similar closing rate to ChIEF, and was 1.5-fold faster than ChR H134R.

Finally, we tested for optical cross-talk between QuasArs and CheRiff in cultured neurons (**Supplementary Table 4.5**). Illumination sufficient to induce high-frequency trains of APs (488 nm, 140 mW/cm^2) perturbed fluorescence of QuasArs by $< 1\%$ (**Supplementary Fig. 4.12**). Illumination with high intensity red light (640 nm, 900 W/cm^2) induced an inward photocurrent through CheRiff of 14.3 ± 3.1 pA, which depolarized neurons by 3.1 ± 0.2 mV (n = 5 cells) (**Supplementary Fig. 4.14**). For most applications this level of optical crosstalk is acceptable.

Of the many attributes that determine channelrhodopsin function, the most important in CheRiff are its greatly increased sensitivity at low illumination intensity and its fast opening kinetics. These properties allow sub-cellular and low-intensity triggering of precisely timed APs.

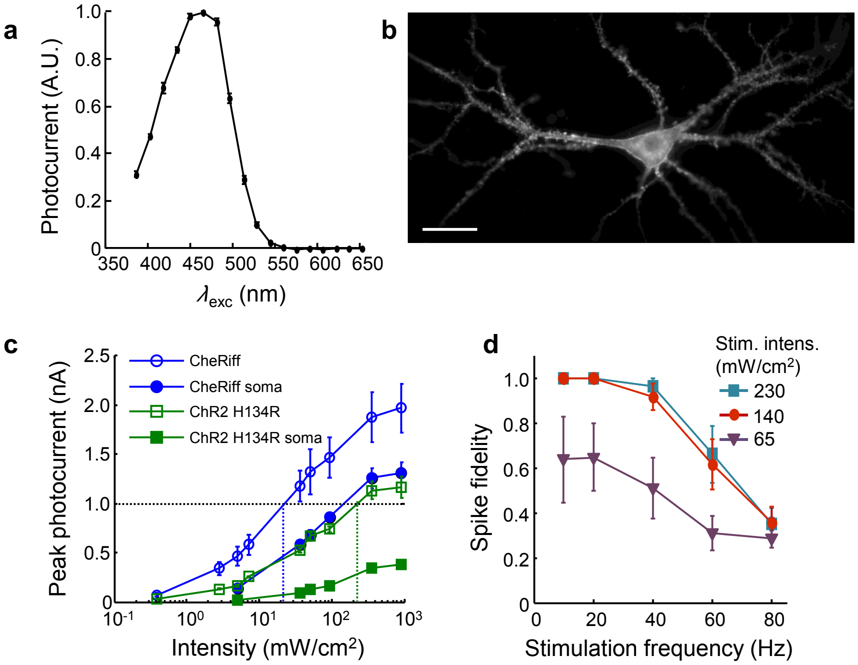

Figure 4.2: CheRiff is a fast and sensitive blue-shifted channelrhodopsin. (**a**) Action spectrum acquired in HEK293T cells (n = 6 cells). CheRiff had a blue-shifted action spectrum with a peak at I_{max} ~ 460 nm. (**b**) Cultured rat hippocampal neuron expressing CheRiff-eGFP, imaged via eGFP fluorescence. Scale bar 25 μm. Image acquired on an sCMOS detector. (**c**) Comparison of photocurrents as a function of illumination intensity in matched neuronal cultures expressing CheRiff (n = 5 cells) or ChR2 H134R (n = 5 cells). Illumination was either over the whole cell or confined to the soma. (**d**) Spiking fidelity as a function of stimulation frequency and illumination intensity in neurons expressing CheRiff (n = 5 cells). Cells were stimulated with trains of 40 pulses (2 ms pulse width, 10 to 80 Hz) at three different blue light intensities. Error bars in (**c**) and (**d**) represent s.e.m.

4.2.3 OPTOPATCH CONSTRUCTS

Optopatch1 and Optopatch2 consisted of bicistronic vectors for co-expression of CheRiff-eGFP and QuasAr1- or QuasAr2-mOrange2, respectively (**Supplementary Fig. 4.15**). We also made Optopatch variants which contained non-fluorescent eGFP and mOrange2 mutants, freeing the spectrum for other uses (**Methods Section 4.4**). The QuasAr and CheRiff constructs could also be delivered separately, but the bicistronic vector maintained a more uniform ratio of actuator to reporter expression levels.

We characterized Optopatch2 in detail. When expressed under a CaMKIIα promoter in cultured rat hippocampal neurons (**Methods Section 4.4**), Optopatch2 showed high expression and good membrane trafficking of both CheRiff and QuasAr2 (**Fig. 4.3a**). Patch clamp measurements found no statistically significant effect of expression on membrane resistance ($P = 0.72$, two-tailed student's *t*-test), membrane capacitance ($P = 0.87$), resting potential ($P = 0.31$), threshold current ($P = 0.67$), or threshold potential ($P = 0.38$), when compared to paired cultures transfected with cytoplasmic GFP driven by a CaMKIIα promoter ($n = 8$ cells for Optopatch2, $n = 7$ cells for GFP) (**Supplementary Fig. 4.16**).

A neuron expressing Optopatch2 was exposed to whole-field illumination with pulses of blue light (10 ms, 25 mW/cm^2) to stimulate CheRiff, and simultaneous constant illumination with red light (800 W/cm^2) to excite fluorescence of QuasAr2. We imaged fluorescence of QuasAr2 at a 1 kHz frame rate and calculated fluorescence from whole-cell average intensity (**Supplementary Fig. 4.9**), while simultaneously recording membrane voltage via a patch pipette. The optical and electrical traces corresponded closely (**Fig. 4.3b**).

Raw movies acquired at 1 kHz clearly showed fluorescence changes due to optically triggered APs (**Supplementary Movie 4.7.1**). Averaging temporally registered AP movies over multiple trials improved the SNR for sub-cellular AP mapping (**Supplementary Movie 4.7.2**). Under focused red illumination (2200 W/cm^2), back-propagating APs were detected in single dendritic spines on a single-trial basis, with an SNR of 2.5 (**Fig. 4.3c**).

4.2.4 PROBING SYNAPTIC TRANSMISSION

With Optopatch, one can stimulate and record from independently selected and rapidly reconfigured regions of a neural circuit. We implemented this capability in culture using a digital micromirror device (DMD) to pattern the blue CheRiff excitation [154], and wide-field red illumination to monitor voltage throughout the field of view (**Methods Section 4.4**).

We probed synaptic transmission by optically stimulating the soma of single cells, and optically monitoring electrical responses in neighboring cells. Optically induced single APs in the presynaptic cell led to fluorescence transients indicative of excitatory post-synaptic potentials (EPSPs), as well as occasional failures of synaptic transmission, in the postsynaptic cell (**Fig. 4.3d**). The mean interval between the peak of the AP in the upstream cell and the onset of the optically detected EPSP in the downstream cell was < 2 ms, indicating a monosynaptic connection [38]. Addition of synaptic blockers (10 μM NBQX, 20 μM Gabazine, 25 μM AP-V) quieted the fluorescence response in the postsynaptic cell, without perturbing presynaptic activity. Validation measurements with patch clamp recordings showed millivolt-level correspondence of optically and electrically recorded postsynaptic potentials, as well as inhibition of these signal by synaptic blockers (**Supplementary Fig. 4.17**).

4.2.5 PROBING AP PROPAGATION

We next sought to apply the extremely fast response of Optopatch1 (containing QuasAr1) to probe the microsecond-timescale dynamics of AP initiation and propagation within a single cell. We used the DMD to target optical stimulation to either a dendrite or the soma and recorded the fluorescence dynamics at a 1 kHz frame rate. To improve the SNR we averaged 100 to 400 temporally registered optically induced APs. These mean-AP movies showed spread of the subthreshold voltage outward from the stimulated region, followed by a sudden spike in cell-wide fluorescence that peaked within two frames (**Supplementary Movie 4.7.3**). Thus the native 1 kHz frame rate was insufficient to resolve the details of AP prop-

Figure 4.3 ***(following page)*****: Optopatch enables high fidelity optical stimulation and recording in cultured neurons.** (**a**) Trafficking of Optopatch components in cultured rat hippocampal neurons. Left: CheRiff-eGFP, measured via eGFP fluorescence. Right: QuasAr2, measured via retinal fluorescence. Scale bars: top 20 μm, bottom 5 μm. (**b**) Temporally precise optical initiation and monitoring of single APs. Blue: CheRiff excitation (488 nm, 25 mW/cm², 10 ms pulses, repeated at 5 Hz). Red: whole-cell single-trial unfiltered fluorescence. Black: patch clamp recording. (**c**) Optical mapping of an AP induced via stimulation of the soma (488 nm, 95 mW/cm², 10 ms pulses, repeated at 5 Hz). Top: Filmstrip showing average of $n = 20$ temporally registered APs. Fluorescence is normalized to mean fluorescence of the dendrite. Images are composite of mean fluorescence (gray) and changes in fluorescence (heat map). Arrow indicates dendritic spine. Scale bar 5 μm. Bottom: Single-trial detection of back-propagating APs in a single dendritic spine. Scale bar 1 μm. Top traces: ten single-trial recordings from the spine (red) and their average (blue). Bottom traces: ten single-trial recordings from the parent dendrite. (**d**) Synaptic transmission. Optical stimulation of one soma (highlighted in blue; 488 nm, 140 mW/cm², 10 ms pulses, repeated every 15 s) induced single APs in the stimulated cell (i) and EPSPs in the neighboring cell (ii). Synaptic blockers suppressed the response in the postsynaptic cell but not in the presynaptic cell. (**e**) Sub-frame interpolation of AP propagation in a neuron expressing Optopatch1 (**Supplementary Movie 4.7.4**). Excitation targeted to dendrites (488 nm, 100 mW/cm², 50 ms pulses, repeated at 5 Hz). Movie constructed from an average of 203 temporally registered APs. Scale bar 50 μm. Bottom right: Immunostaining of the same cell with anti-eGFP and anti-AnkyrinG. Scale bar 25 μm. Magenta arrows: site of action potential initiation, distal end of the AIS. (**f**) Parallel optical recording under increasingly strong 0.5 s optical step-stimuli (488 nm, 0 to 10 mW/cm², 500 ms pulses, repeated at 6 s intervals). Asterisk indicates a cell that showed periodic bursts of 3-4 APs under weak stimulation. Synaptic blockers were added to suppress network activity. Scale bar 500 μm. Image is of eGFP fluorescence. Data in (**a, c, f**) acquired on an sCMOS detector; data in (**b, d, e**) acquired on an EMCCD.

Figure 4.3: (continued)

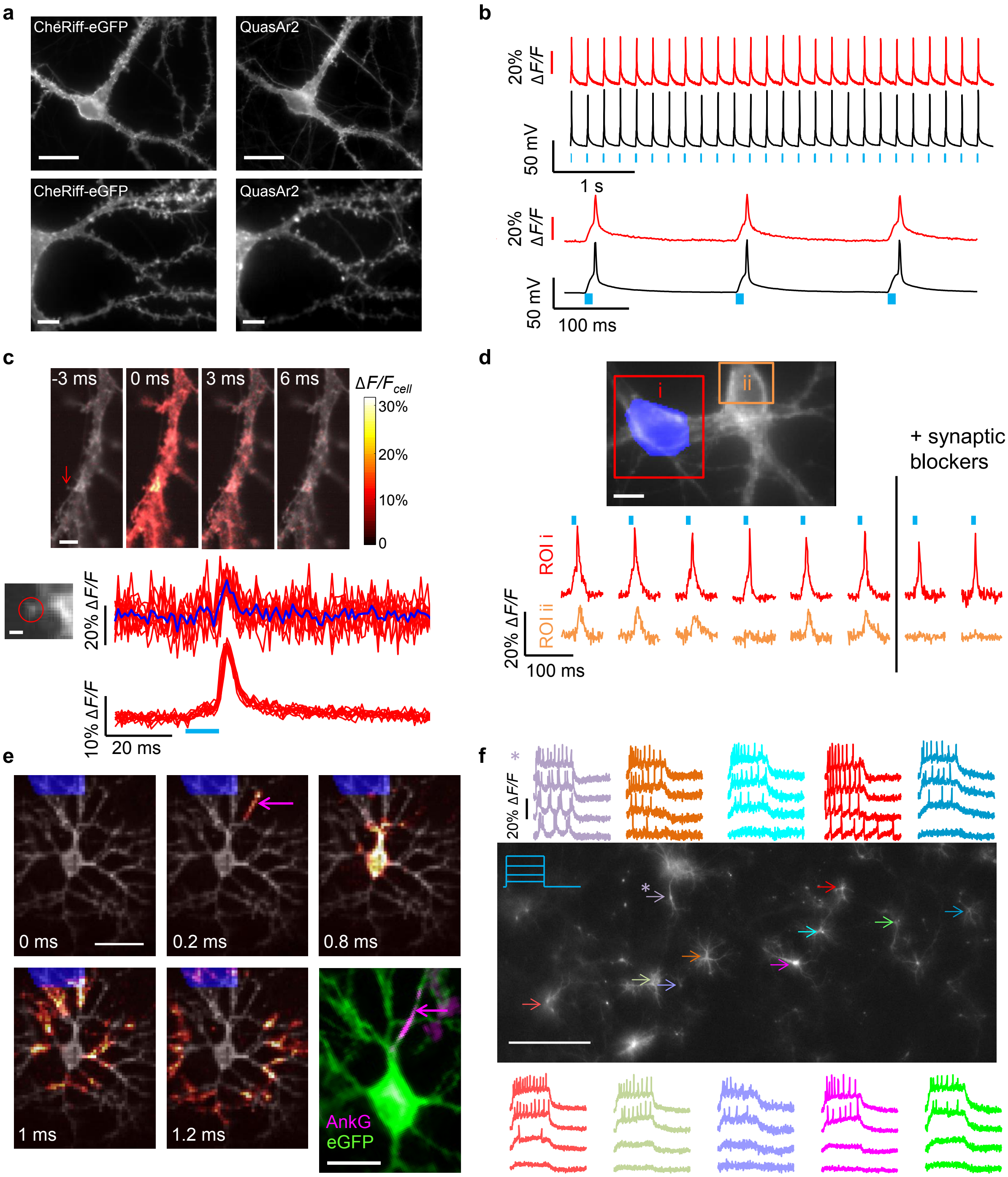

agation.

To probe microsecond-level dynamics, we adapted the sub-frame interpolation approach of Foust [39] and Popovic [129] (**Supplementary Fig. 4.18, Methods Section 4.4**). By interpolating a smoothly varying spline to the fluorescence intensity time-trace at each pixel, we inferred the timing with which the fluorescence crossed a user-selected threshold (e.g. 50% maximum deviation) with a precision better than the exposure time of the camera. Mean deviation between optically inferred and electrically recorded AP timing at the soma was 40 – 70 μs (**Supplementary Fig. 4.18**). We then constructed a higher time-resolution movie highlighting each pixel at the sub-frame time of its wavefront crossing. This interpolation technique does not rely on an assumed AP waveform, nor does it assume wavelike propagation; it is compatible with APs that change shape within or between cells.

The visually striking propagation movies clearly showed AP initiation 30 – 50 µm from the soma in a single thin neurite, presumed to be the axon, in n = 8 of 8 measured cells (**Fig. 4.3e, Supplementary Movies 4.7.4- 4.7.6**), regardless of stimulus location. The AP then propagated down the putative axon and back into the soma and dendrites. Latencies between AP initiation and arrival in the soma were 320 ± 220 μs (n = 8 cells, mean ± s.d).

After acquiring Optopatch data, we fixed the cells and stained for ankyrin-G, a marker of the axon initial segment (AIS, **Fig. 4.3e**). The optically detected zones of AP initiation coincided with the distal end of the AIS, consistent with previous experiments using voltage-sensitive dyes [84]. Thus Optopatch can resolve functionally significant sub-cellular and microsecond timescale details of AP dynamics.

4.2.6 PARALLEL MEASUREMENTS IN NEURONAL CULTURES

To achieve high-throughput functional characterization in neurons, one would like to apply the technique to many cells in parallel. We constructed a low-magnification, high-speed microscope (**Supplementary Fig. 4.19, Methods Section 4.4**) which robustly reported APs and subthreshold dynamics in up to ~50 cells simultaneously (**Supplementary Movie 4.7.7**). We used a DMD to pattern the blue illumination for targeted CheRiff excitation in user-selected regions. Optical stimulation of a segment of a synaptically connected culture induced network activity which manifested as action potentials and sub-threshold dynamics in the cells not directly stimulated (**Supplementary Fig. 4.20**).

We developed an all-optical protocol to measure neuronal excitability. Synaptic blockers were added to suppress network activity. Cells were stimulated with pulses of blue light (500 ms at 6 s intervals) of increasing intensity (0 to 14 mW/cm^2), while firing patterns were recorded under continuous red illumination (100 W/cm^2). In wide-field measurements on n = 169 neurons expressing Optopatch2, we observed several distinct firing patterns, including fast-adapting and slow-adapting spike trains (**Fig. 4.3f** and **Supplementary Movie 4.7.8**). Two neurons showed intermittent bursting (one of these is indicated by a star in **Fig. 4.3f**). The comparatively high throughput of Optopatch measurements enables detection of rare electrophysiological phenotypes that might be missed in a manual patch clamp measurement on a smaller number of cells.

To test whether high-throughput Optopatch could quantify subtle electrophysiological shifts, we applied the all-optical excitability protocol to a model of homeostatic plasticity of intrinsic excitability (HPIE) [161], in which neurons adapt their excitability to maintain an approximately constant level of activity. Observation of HPIE in culture [33, 53] and *in vivo* [90] has traditionally required laborious patch clamp measurements on many cells.

Neurons expressing Optopatch2 were incubated in tetrodotoxin (TTX, 1 μM) for 48 h and then measured in TTX-free medium in the presence of synaptic blockers [33]. Paired control cultures were incubated without TTX. Cells that had been treated with TTX (n = 94) subsequently showed significantly lower illumination threshold for spiking ($P = 5\times10^{-6}$), shorter interval between first and second spike ($P < 0.001$), and more total spikes ($P < 0.01$) than control cells (n = 75), but only a small change in time from light onset to first spike (**Supplementary Fig. 4.21**), consistent with previous reports [33]. Total data acquisition time was less than 1 h, a fraction of the time that would be required for manual measurements.

Although the HPIE measurements showed population-level changes in excitability, a unique promise of Optopatch is the ability to measure the same cell over several days. In 8 of 10 trials, neurons measured with a 1 min Optopatch protocol were identified and re-recorded 48 hrs later (**Supplementary Fig. 4.22**). This capability could be important in studying neuronal maturation or long-term effects of pharmacological, genetic, or environmental perturbations.

4.2.7 PROBING EXCITABILITY IN HIPSC-DERIVED NEURONS

Human-derived neurons show promise as a platform for studying human neurophysiology in health and disease [158]. However, variability arises at multiple levels in this approach [18]. Each patient's genetic background modifies neuronal function, even for nominally monogenic diseases. Additional variability arises between iPSC clones from a single patient, between differentiations, and between cells cultured within a single well. Differing degrees of maturation are a particularly large source of cell-to-cell variability within a dish [145]. Furthermore, for disease-modeling efforts, one may wish to test many differentiation protocols or pharmacological perturbations. Together, these factors motivate a need for accurate functional characterization with robust statistics. The low throughput and selection bias of manual electrophysiology present a serious bottleneck.

We first assessed whether Optopatch expression perturbed electrophysiology in hiPSC-derived neurons. Cells were transfected with Optopatch2 and cultured on a rat glial monolayer. The CamKIIα promoter genetically targeted the measurement to mature neurons within this highly heterogeneous culture **REF**. Patch clamp measurements on cells transfected with Optopatch2 (n = 11) or with GFP (n = 11) showed no significant difference in membrane resistance (P = 0.82, two-tailed student's *t*-test), membrane capacitance (P = 0.88), resting potential (P = 0.34), or action potential activation threshold (P = 0.78) (**Supplementary Fig. 4.23**). Optically evoked and optically monitored trains of APs showed the expected changes upon addition of ion-channel blockers lidocaine and tetraethylamine (**Supplementary Fig. 4.24**).

We then applied Optopatch to test for HPIE in hiPSC-derived neurons. This subtle electrophysiological effect is one of several forms of neural plasticity which have not previously been reported in human-derived neurons. HiPSC-derived neurons were incubated in 1 μM TTX for 48 h. Upon return to TTX-free medium, treated cells showed a substantial increase in subsequent optically measured excitability (n = 31 cells) relative to controls (n = 32 cells) (**Fig. 4.4a-e**), demonstrating positive HPIE.

We next tested for negative HPIE: conditions that depolarize cells (e.g. high

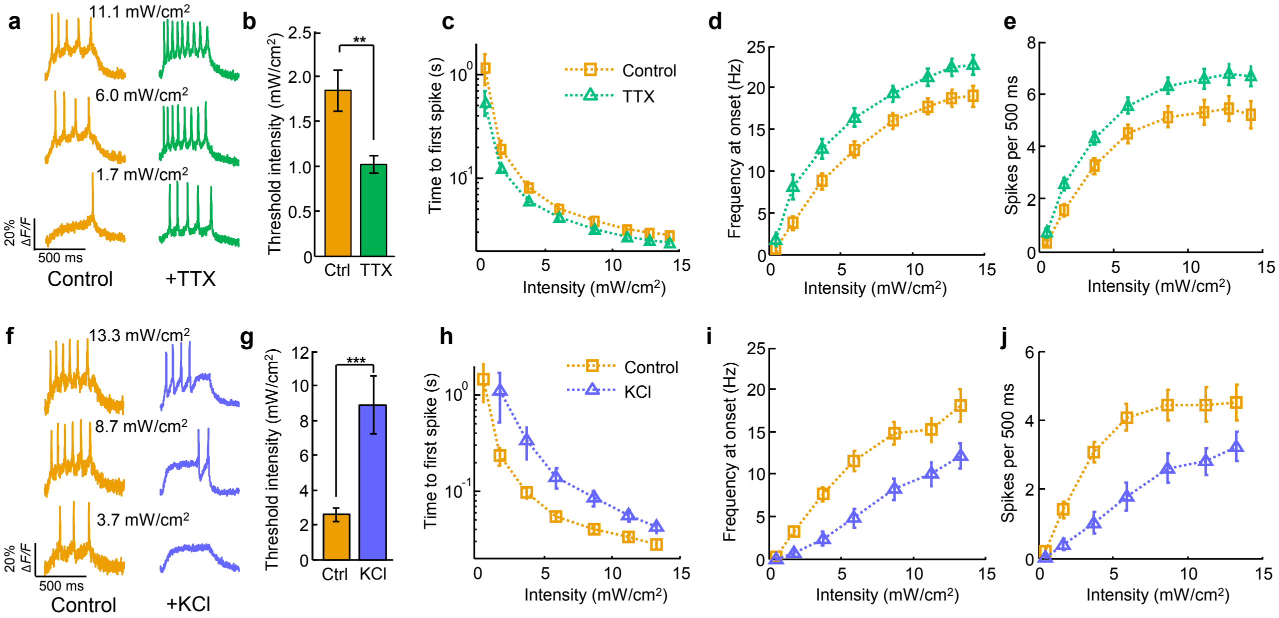

Figure 4.4: Homeostatic plasticity of intrinsic excitability in human iPSC-derived neurons probed via Optopatch2. (**a-e**) Positive HPIE. Data from $n = 32$ control cells and $n = 31$ TTX-treated cells. (**a**) Representative optical recordings from single neurons after incubation in TTX and matched control cells. (**b**) Threshold stimulation intensity (488 nm) to induce at least one spike in 500 ms. TTX treated cells had a significantly lower threshold than controls ($P = 0.004$). (**c**) Time from onset of illumination to first spike. (**d**) Spike frequency at onset (inverse time between first and second spike). (**e**) Total spikes per 500 ms stimulus. Measures in (**d**) and (**e**) showed significantly increased excitability in TTX-treated cells relative to control cells ($P < 0.05$ for each stimulation intensity 1.7 mW/cm²). (**f-j**) Negative HPIE. Data from $n = 25$ control cells and $n = 28$ KCl-treated cells. Panels are the same as (**a-e**). KCl treated cells had a significantly higher stimulation intensity threshold than controls ($P = 7\times10^{-6}$). Measures in (**h-j**) showed significantly decreased excitability in KCl-treated cells relative to control cells ((**h**): $P < 0.01$ for all stimulus intensities; (**i**): $P < 0.05$ for stimulus intensities 1.7 mW/cm²; **j**: $P < 0.05$ for stimulus intensities 11.2 mW/cm²). For all experiments fluorescence was excited at 300 W/cm², and collected at a 1 kHz frame rate on an EMCCD. All error bars represent s.e.m. Statistical significance determined by two-tailed student's t-test or Mann–Whitney U test. ** $P < 0.01$; *** $P < 0.001$.

KCl) induce a gradual decrease in intrinsic excitability [53]. HiPSC-derived neurons were incubated in 15 mM KCl for 60 hrs. Upon return to baseline conditions (2.5 mM KCl), treated cells showed a substantial decrease in subsequent optically measured excitability (n = 28 cells) relative to controls (n = 25 cells) (**Fig. 4.4f-j**).

Post-measurement immunostaining with anti-human nuclear antigen 1 and anti-GFP antibodies confirmed that all neurons tested were of human origin (**Supplementary Fig. 4.25**). Validation measurements with manual patch clamp confirmed that the HPIE protocols did not change CheRiff photocurrents (**Supplementary Fig. 4.26**).

These experiments demonstrate that human iPSC-derived neurons undergo bidirectional HPIE, and that Optopatch measurements can non-perturbatively report subtle differences in electrophysiology in these cells. High-throughput Optopatch measurements promise to be a powerful tool for functional characterization of neuronal populations in hiPSC-based disease modeling efforts.

4.2.8 IMAGING IN ORGANOTYPIC SLICE CULTURE

Voltage imaging with GEVIs in intact tissue would enable functional mapping of sub-cellular and circuit-level signal processing. Application of GEVIs to recording of APs in mammalian brain tissue has been limited by the low voltage sensitivity and slow response of existing indicators [3, 23]. No GEVI has been shown to report single-trial APs in tissue with high fidelity.

We expressed Optopatch2 in organotypic brain slice using biolistic gene delivery. Neurons that had taken up the gene were clearly visible via fluorescence of eGFP (indicating CheRiff) and QuasAr2 under wide-field epifluorescence imaging (20× N.A. 1.0 water immersion objective) (**Fig. 4.5a**). Upon illumination with pulses of blue light (10 ms, repeated at 5 Hz, 7.5 mW/cm^2), the fluorescence under red excitation (1,200 W/cm^2 nominal incident intensity, not corrected for light scatter) showed clearly resolved single-trial APs in the soma (**Fig. 4.5b**) and in dendrites (**Supplementary Fig. 4.27**). These traces represent raw fluorescence, without background subtraction or correction for photobleaching.

We performed Optopatch measurements on n = 7 separately prepared organotypic brain slices (**Supplementary Fig. 4.28**). AP amplitudes ranged from $\Delta F/F$ = 7.2 to 26.1% (mean 15.9%, n = 7 cells), calculated without subtraction

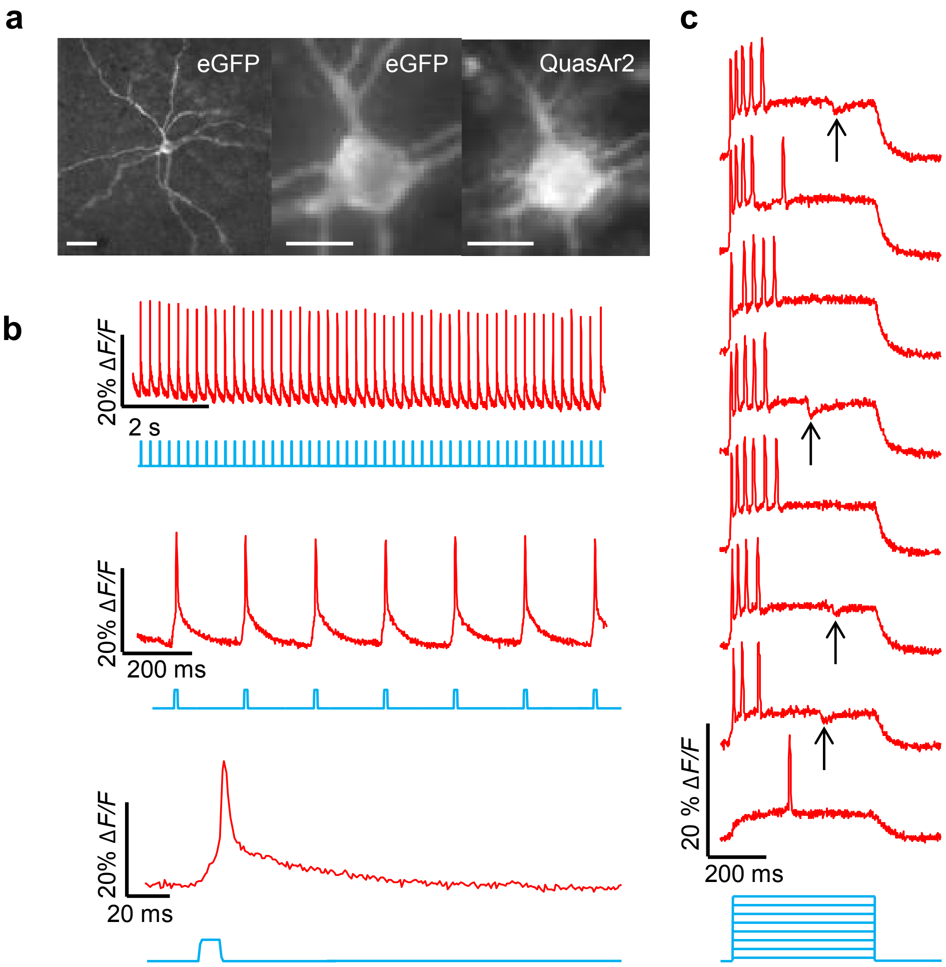

Figure 4.5: Optopatch2 in organotypic brain slice. (**a**) Left and middle: eGFP fluorescence, indicating CheRiff distribution. Right: QuasAr2 fluorescence. Scale bars from left to right: 50 μm, 20 μm, 20 μm. (**b**) Single-trial optical recordings of APs initiated by pulses of blue illumination (10 ms, 7.5 mW/cm²). Signal represents whole-soma fluorescence without photobleaching correction or background subtraction. (**c**) Bursts of APs triggered by steps of blue illumination (500 ms, 1-10 mW/cm²). Inhibitory potentials (arrows) were sometimes observed during the stimulation intervals, but not during rest intervals, suggesting inhibitory feedback arising from optically induced network activity. For (**b**) and (**c**), red illumination was 1,200 W/cm² nominal incident intensity, not corrected for light scatter. Fluorescence collected at a frame rate of 1 kHz on an EMCCD camera.

of background autofluorescence. Whole cell-body fluorescence reported APs with SNRs ranging from 7.8 to 65.6 (mean 31.9) in a 1 kHz bandwidth. At lower red excitation intensity (400 W/cm^2 nominal incident intensity, not corrected for light scatter), whole cell-body fluorescence reported APs with SNRs ranging from 7.2 to 35.7 (mean 16.5) in a 1 kHz bandwidth.

We further tested the response of neurons in tissue to extended pulses of blue illumination (0.5 s, 1 to 10 mW/cm^2). This stimulus elicited a variety of firing patterns, including single spikes, bursts (**Fig. 4.5c**) and sustained activation (**Supplementary Fig. 4.28**). Optically induced spike trains were often interrupted by hyperpolarizing fluorescence transients, which we provisionally ascribe to inhibitory feedback in the local micro-circuit. We did not observe these inhibitory potentials in the absence of optical stimulation. These results demonstrate the feasibility of optically measuring single-cell, single-trial AP waveforms, excitability, and subthreshold dynamics in tissue with high SNR.

Finally, we compared Optopatch to ArcLight in organotypic slice (**Supplementary Fig. 4.28, Methods Section 4.4**). Under manual patch clamp stimulation, ArcLight fluorescence resolved single action potentials with a mean value of $\Delta F/F = -1.5 \pm 0.4\%$ and an SNR of 7.1 ± 2.8 ($n = 6$ cells) (excitation at 488 nm, 50 W/cm^2). The ArcLight fluorescence transients had a mean width (at 70% maximum deviation) of 21.5 ± 3.0 ms. Thus QuasAr2 reports action potentials in tissue with greater sensitivity, higher SNR, and better temporal resolution than ArcLight.

4.3 DISCUSSION

The combination of improved reporter and improved actuator in the Optopatch constructs facilitates rapid, non-invasive characterization of genetically defined cells across spatial scales from microns to millimeters, and temporal scales from microseconds to days. Optopatch has not yet been implemented with real-time feedback on the illumination, so it is not suited for voltage-clamp experiments. Nonetheless, with the assistance of computational modeling, open-loop voltage measurements can probe ionic conductances and membrane electrical properties [69, 167]. Absolute voltage measurements with GEVIs are challenging due to variations in expression level and membrane trafficking. A recent report demonstrated measurements of absolute voltage through its effect on photocycle dynamics in an Archaerhodopsin mutant [66]. A similar strategy may apply to the QuasArs.

Our discovery of homeostatic plasticity in intrinsic excitability of hiPSC-derived neurons serves as a paradigm for other Optopatch assays of neuronal excitability. Such assays may probe cell-autonomous functional phenotypes in hiPSC-based models of diseases such as ALS [166], epilepsy [60], and Parkinson's disease [6]. Other neurodevelopmental and neuropsychiatric diseases arise primarily through synaptic dysfunction. These include Rett syndrome [104], Fragile X [5], and Phelan-McDermid syndrome [145]. Development of robust assays of synaptic function will likely benefit from incorporation of cell patterning techniques to control the type and location of synaptic connections. A merit of optical electrophysiology for disease modeling and drug screening is that it does not require mechanical access; thus it is compatible with microfluidic compound delivery and high throughput experimental formats. Optopatch measurements preserve the sterility of the sample and the integrity of the cell membrane, and thus are compatible with studies of long-term responses to chronic pharmacological perturbations.

We demonstrated that Optopatch functions in intact mammalian tissue. With extension to multiple genetically specified cells, Optopatch measurements in tissue may provide a useful tool for functional circuit mapping [128]. With improved optical sectioning capability, sub-cellular Optopatch measurements could enable inference of electrophysiological parameters in multi-compartment neural models of single-cell information processing.

For applications *in vivo*, the new QuasAr reporters are likely to be appropriate for measurements on a few cells or small networks. The required laser power scales with the field of view, so tissue heating may be a concern for fields of view > ~200 μm on a side. Applications to larger circuits will likely benefit from further improvements to the indicator, primarily increased brightness, and exploration of two-photon excitability or other contrast modalities. Small transparent organisms, e.g. zebrafish and C. elegans, are likely early targets as most illumination passes through the body without depositing heat.

4.4 METHODS

4.4.1 ENGINEERING OF ARCH

We adopted a hierarchical approach to screening that prioritized brightness over multiple secondary selection criteria. The brightness screen was conducted by examining the fluorescence of large libraries of variants expressed in bacterial colonies. Subsequent screens for trafficking, speed, and voltage sensitivity were performed in HeLa cells subjected to field stimulation and induced transmembrane voltages, and then in HEK cells with patch clamp.

Molecular biology procedure. Synthetic DNA oligonucleotides used for cloning and library construction were purchased from Integrated DNA Technologies. Pfu polymerase (Fermentas) or AccuPrime Pfx SuperMix (Invitrogen) were used for high fidelity non-mutagenic PCR amplifications in the buffer supplied by the respective manufacturer. Taq polymerase (New England Biolabs) in the presence of $MnCl_2$ (0.1 mM) was used for error-prone PCR. PCR products and products of restriction digests were routinely purified using preparative agarose gel electrophoresis followed by DNA isolation using the GeneJET gel extraction kit (Fermentas). Restriction endonucleases were purchased from Fermentas and used according to the manufacturer's recommended protocol. Ligations were performed using T4 ligase (Invitrogen) or Gibson Assembly (New England Biolabs). Small-scale isolation of plasmid DNA was performed by GeneJET miniprep kit (Fermentas). The cDNA sequences for all Arch variants and fusion constructs were confirmed by dye terminator cycle sequencing using the BigDye Terminator Cycle Sequencing kit (Applied Biosystems). Site-directed mutagenesis and randomization of targeted codons was performed with either the QuikChange Lightning Single or Multi kit (Agilent Technologies).

Construction of Arch mutant libraries. A library of $> 10^4$ mutants was generated by error-prone PCR of the gene encoding Arch D95N. These variants were then joined with the gene encoding mOrange2 by a two-part overlap extension PCR. The 5' piece used in the overlap extension was prepared by error-prone PCR of Arch D95N as template with a mixture of the forward and reverse primer. The 3' piece for use in the overlap extension was prepared by high fidelity PCR amplification of mOrange2. The full-length Arch-mOrange2 gene library was assembled by overlap extension PCR using an equimolar mixture of primers together with a mixture of the 5' and 3' PCR fragments described above (50 ng each) as the template. In later rounds of directed evolution, error-prone PCR and StEP PCR DNA shuffling [169] were both used for construction of Arch-mOrange2 gene libraries.

The full-length PCR product (approximately 1,500 b.p.) was purified by agarose gel electrophoresis, doubly digested, and ligated between the XbaI and HindIII sites of a modified pBAD vector which was generated by deleting the ETorA tag between the NcoI and XbaI sites of the pTorPE vector [170] using Quikchange Lightning kit.

Following ligation, electrocompetent E. coli strain DH10B was transformed with the library of gene variants and cultured overnight at 37 °C on 10-cm Petri dishes of LB-agar supplemented with 100 µL of 4 mM retinal (Sigma), 100 µg/mL ampicillin (Sigma), and up to 0.0020% (wt/vol) L-arabinose (Alfa Aesar). The retinal solution was added on the surface of LB-agar plates evenly and air-dried prior to plating the cell suspension. At concentrations of L-arabinose higher than 0.0020% (wt/vol) we observed abnormal colony morphologies and reduced fluorescent brightness, presumably due to cytotoxicity caused by overexpression.

Screening of Arch mutants in E. coli. The imaging system used for library screening has previously been described in detail [26]. We screened 10,000–20,000 colonies (10–20 plates of bacterial colonies) per round of random mutagenesis. For libraries generated by randomization of one or more codons, we screened approximately 3-fold more colonies than the expected library diversity (e.g. 3,000 colonies for a 1,000-member library).

We acquired two images of colonies using filter sets for mOrange2 (exc. 540 - 580 nm, em. 600 - 660 nm) and Arch (exc. 604-640 nm and em. 660 - 700 nm). An image of the ratio of Arch: mOrange2 fluorescence was calculated, and the colonies with the top 0.01% to 0.1% highest ratios were manually picked. Picked clones were individually cultured in 2 mL liquid LB medium (200 µg/mL ampicillin) shaken (250 rpm) overnight at 37 °C.

Protein expression was induced by adding 2 mL of liquid LB medium containing 120 μM retinal, 200 µg/mL ampicillin and 0.2% L-arabinose to the overnight culture, followed by incubation at 37 °C for 3 hours. The cell pellets were collected by centrifugation, washed and resuspended in buffered M9 salt solution containing 7 g/L Na_2HPO_4, 3 g/L KH_2PO_4, 0.5 g/L NaCl and 1 g/L NH_4Cl. The suspension was then diluted 5-fold prior to acquisition of its fluorescence spectrum in a Safire 2 fluorescence microplate reader (Tecan).

The emission profiles of each variant under excitation at 525 nm and 600 nm were acquired and normalized by the absorbance at 600 nm. The cell pellets of the three variants with the highest ratios of Arch to mOrange2 and the two variants with the brightest absolute Arch fluorescence were treated for plasmid DNA extraction, and the pooled genes were used as templates for construction of gene libraries in the next round of directed evolution. After five iterations we arrived at a non-pumping variant of Arch with five mutations relative to wild-type (P60S, T80S, D95N, D106Y, and F161V) and substantially improved brightness under excitation with low illumination intensity. This variant, designated Arch 3.5, was used as the template for subsequent efforts to address the secondary selection criteria.

Random mutagenesis at positions Asp95 and Asp106. We next focused on tuning other properties of Arch including voltage sensitivity, response kinetics, membrane trafficking and the undesirable dependence of brightness on illumination intensity. Positions Asp95 and Asp106 of Arch are structurally aligned with positions Asp85 and Asp96 of bacteriorhodopsin, and have been reported to play key roles in proton translocation during the photocycle [91, 92]. The voltage sensing mechanism of Arch is likely due to electric-field-dependent protonation of the retinal Schiff base [85, 88], so we reasoned that perturbations of the proton translocation network around the Schiff base could potentially affect the voltage sensitivity, response kinetics, or complex photophysics [103].

We constructed libraries in which Asp95 and Asp106 were randomized to a subset of all possible amino acid substitutions. First, we randomized position 95 using codon HVS (where H = A, C or T; V= A, C, or G; S = C or G), which encodes for all amino acids except Ala, Gly, Asp, Glu and Val. This library was screened by fluorescence imaging of E. coli colonies. Variants that retained a high ratio of Arch to mOrange2 fluorescence were picked and expressed in HeLa cells for screening via induced transmembrane voltage (see below).

The mutation N95H emerged as the best from the first round of screening in HeLa cells. We then constructed a second library by randomizing position 106 to a subset of amino acids with polar or charged side chains (codon NRC, where N = A, C, G, or T; R = A or G), and screened these in HeLa cells. The variant with histidine at position 106 proved most promising and was designated QuasAr1.

Solubilization and spectroscopic characterization of QuasAr1 and QuasAr2. *E. coli* expressing QuasAr1 and QuasAr2 were grown in 12 mL liquid LB medium with 200 µg/ml ampicillin overnight. The next day, 12 mL of liquid LB medium containing 50 µM retinal, 200 µg/ml ampicillin and 0.1% arabinose was added into the overnight culture, followed by additional incubation at 37 °C for 4 hours. The cell pellets were collected by centrifugation and lysed by suspension in B-PER solution (Pierce). The cytoplasmic fraction was discarded after centrifugation and the colored insoluble fraction was resuspended in phosphate buffered saline (PBS) containing 1.5% n-dodecyl-β-D-maltopyranoside (Affymetrix, Inc.). The suspension was homogenized by an ultrasonic homogenizer and centrifuged (17,000 g for 15 mins, 4 °C). The solubilized protein in the supernatant was used for *in vitro* spectroscopic characterization.

Absorption spectra were recorded on a DU-800 UV-visible spectrophotometer (Beckman) and fluorescence spectra were recorded on a Safire2 plate reader (Tecan). Cy5 carboxylic acid (Cyandye) was used as the reference for quantum yield measurement. Quantum yield measurements were performed on a series of dilutions of each protein solution and standard, with absorbance values ranging from 0.01 to 0.05 at 600 nm. The fluorescence emission spectra of each dilution were recorded with excitation at 600 nm and the total fluorescence intensities obtained by integration. Integrated fluorescence intensity vs. absorbance was plotted for each protein and each standard. Quantum yields, Φ, were determined from the slopes (S) of each line using the equation: $\Phi_{protein} = \Phi_{standard}(S_{protein}/S_{standard})$.

Expression vectors for HeLa cells. To express Arch-mOrange2 variants in HeLa cells, the gene in the pBAD vector was first amplified by PCR using primers that introduced cut sites BamHI and XbaI before and after Arch-mOrange2 variants. The reverse primer encoded the endoplasmic reticulum (ER) export sequence from the inward-rectifier potassium channel Kir2.1 (FCYENE) [102], which has been reported to be effective for improving the membrane trafficking of Arch in mammalian cells [46].

The purified DNA was digested with BamHI and XbaI restriction enzymes and ligated into a purified pcDNA3.1 plasmid that had been digested with the same two enzymes. The ligation reaction was used for transformation of electrocompetent *E. coli* strain DH10B cells. Cells were plated on LB/agar supplemented with ampicillin and individual colonies were picked into 4 mL of LB/ampicillin following overnight incubation at 37 °C. Liquid cultures were shaken at 250 rpm and 37 °C for 12-15 h and then a small scale isolation of plasmid DNA was performed. Each gene in pcDNA3.1 was fully sequenced. Plasmids were then used for cell transfection as described below.

Induced transmembrane voltage (ITV) in HeLa cells. We co-expressed prospective Arch variants in HeLa cells with the inward rectifier potassium channel, Kir2.1. Expression of Kir2.1 lowered the resting potential to approximately -60 mV, close to the resting potential of neurons [81, 124]. We reasoned that this effect would center the ITV close to the physiologically relevant range.

HeLa cells were grown to 40-60% confluence on home-made 35 mm glass bottom dishes or 24-well glass bottom plates. Cells were transfected with 1 μg of plasmid DNA comprising a 1:1 mixture of Arch variant and Kir2.1, using either 2 μL Turbofect (Thermo Scientific) or 2 μL Lipofectamine 2000 (Invitrogen) according to the manufacturer's instructions. After 3 h incubation, the medium was exchanged to DMEM with 10% fetal bovine serum. Cells were incubated for an additional 24 h at 37 °C in a CO2 incubator. Immediately prior to imaging, cells were washed twice with Hanks balanced salt solution (HBSS) and then 1 mL of 20 mM HEPES buffered HBSS was added.

Cell imaging was performed with an inverted Eclipse Ti-E (Nikon) equipped with a Photometrics QuantEM 512SC camera, a 150 W mercury-xenon lamp (Hamamatsu), and a 10 mW 638 nm semiconductor diode laser (56ICS/S2669, Melles Griot CleanBeam) aligned just above the angle for total internal reflection. The filters were: 590-650 nm (excitation), 668-738 nm (emission), and 666 nm (dichroic). Movies were acquired at 10 ms/frame. The NIS-Elements Advanced Research software (Nikon) was used for microscope and camera control and data acquisition. A schematic of the setup is shown in **Supplementary Fig. 4.6**.

To probe the response kinetics and voltage sensitivity, we used a pair of parallel platinum electrodes to apply a reproducible electric field across the cell culture and induce transient asymmetries in the membrane voltage [132]. Platinum electrodes with a gap of 0.5 cm were mounted in a custom plastic support. The electrode pair was placed in the imaging dish or well, and voltage pulses from a 6824A 40V/25A DC Power Supply (HP / Agilent) were applied using waveforms generated by a pulse generator PG 58A (Gould Advance Ltd). The typical waveform had square-wave pulses lasting 20 ms, and pulse amplitudes from 25 – 35 V. Fluorescence was imaged at 100 Hz frame rate in 4×4 binning mode for 10 seconds. During each voltage pulse, opposite sides of the cell showed opposite fluorescence transients. Typical fluorescence traces are shown in **Supplementary Fig. 4.6**.

Raw fluorescence traces were corrected for background autofluorescence and photobleaching. The average voltage sensitivity ($\Delta F/F_{min}$) and signal-to-noise ratio of each Arch variant were compared to the best variant of the previous generation, and only the variants with equal or improved performance were chosen as templates for the next round of screening.

Expression vectors for HEK cells and neurons. To enable more accurate electrophysiological characterization via patch clamp in HEK cells and primary neuron cultures, we cloned QuasAr1 into the BamHI/EcoRI sites of lentivirus vector FCK-Arch-GFP (Addgene: 22217). This vector contains a CaMKIIα promoter and a Woodchuck Hepatitis Virus Posttranscriptional Regulatory Element (WPRE) after the 3' end of the open reading frame. The primers used introduced a trafficking signal (TS) motif and ER export signal peptide sequence at the C-terminus of the protein.

Simultaneous electrophysiology and fluorescence in HEK cells. HEK293T cells (ATCC CRL-11268) were cultured and transfected following standard protocols [88]. Cells tested negative for mycoplasma. Briefly, HEK-293 cells were grown at 37 °C, 5% CO2, in DMEM supplemented with 10% FBS and penicillin-streptomycin. 400 ng of plasmid DNA was transfected using Transit 293T (Mirus) following the manufacturer's instructions, and assayed 48 hours later. The day before recording, cells were re-plated onto glass-bottom dishes (In Vitro Scientific) at a density of 10,000 cells/cm^2.

Cells were supplemented with retinal by diluting stock retinal solutions (40 mM, DMSO) in growth medium to a final concentration of 5 μM, and then returning the cells to the incubator for 0.5 - 1 hr. All imaging and electrophysiology were performed in Tyrode buffer (containing, in mM: 125 NaCl, 2.5 KCl, 3 $CaCl_2$, 1 $MgCl_2$, 10 HEPES, 30 glucose pH 7.3, and adjusted to 305-310 mOsm with sucrose). A gap junction blocker, 2-aminoethoxydiphenyl borate (50 μM, Sigma), was added to eliminate electrical coupling between cells.

Filamented glass micropipettes (WPI) were pulled to a tip resistance of 5–10 MΩ, and filled with internal solution containing 125 mM potassium gluconate, 8 mM NaCl, 0.6 mM $MgCl_2$, 0.1 mM $CaCl_2$, 1 mM EGTA, 10 mM HEPES, 4 mM Mg-ATP, 0.4 mM Na-GTP (pH 7.3); adjusted to 295 mOsm with sucrose. Pipettes were positioned with a Sutter MP285 manipulator. Whole-cell, voltage and current clamp recordings were acquired using an Axopatch 700B amplifier (Molecular Devices), filtered at 2 kHz with the internal Bessel filter and digitized with a National Instruments PCIE-6323 acquisition board at 5-10 kHz. Data was only acquired from HEK cells having reversal potentials between -10 and -40 mV, access resistance < 25 MΩ and membrane resistance > 0.5 GΩ.

Simultaneous whole-cell patch clamp recordings and fluorescence recordings were acquired on a home-built, inverted epifluorescence microscope, described previously [88] and described below in "Optopatch Apparatus". For step response measurements, voltage clamp electronics were compensated 90-95%. We examined variants of QuasAr1 with mutations at position 95 (Asn, Cys, Gln, His and Tyr) and position 106 (Arg, Asp, Asn, Cys, Glu, His, Lys and Tyr). These experiments confirmed that histidine at position 106 provided the best combination of improved voltage sensitivity, and fast kinetics. Mutants with Gln, Cys, or Asn at position 95 exhibited better voltage sensitivity compared to QuasAr1, while retaining fast kinetics. We designated the H95Q mutant QuasAr2.

Analysis of mutations in QuasAr1 and QuasAr2. We developed a structural model of Quasar1 (**Supplementary Fig. 4.7**) based on homologous protein Arch-2 (PDB: 2EI4, ref. [36]). Mutations T80S and F161V are located in the periphery of the protein, while P60S is close to the Schiff base of the retinal chromophore. Given their location, we suspect that the T80S and F161V substitutions are unlikely to have a direct impact on the photophysical properties of the protein, and are more likely to have a role in improving the folding efficiency. In contrast, the close proximity of the P60S substitution to the Schiff base suggests that this mutation has a more direct influence on the photophysical properties.

We compared the Arch double mutants Arch(D95H, D106H) (termed "HH") and Arch(D95Q, D106H) (termed "QH") to the corresponding QuasAr1 and QuasAr2 mutants do determine whether the mutations in the proton-transport chain were sufficient to induce the improved sensor performance. QuasAr1 and QuasAr2 were both substantially brighter than the corresponding double mutants (**Supplementary Fig 4.8**). Furthermore, the voltage sensitivity of the HH, QH, QuasAr1 and wild-type protein were comparable, and three-fold less than the sensitivity of QuasAr2. The QuasArs were faster than their corresponding double mutants. Thus one or more of the three mutations outside the proton transport chain (P60S, T80S, F161V) plays an important role in the brightness, sensitivity, and speed of the QuasAr mutants.

The constructs described in this chapter are available on Addgene.

4.4.2 ENGINEERING OF CHERIFF

The gene for Scherffelia dubia Channelrhodopsin (sdChR) was synthesized with mouse codon optimization. This gene was selected from a screen of channelrhodopsins for its blue excitation peak (474 nm) and its large photocurrent relative to ChR2. However, the trafficking in neurons was poor (**Supplementary Fig. 4.13**). Addition of a trafficking sequence from Kir2.1 improved trafficking greatly [46]. Addition of the ER2 export motif did not appear to further improve trafficking, so this motif was not included in the final construct.

The improved membrane trafficking led to large photocurrents in neurons under blue excitation (2470 ± 170 pA peak, 488 nm, 500 mW/cm^2, n = 3 cells) but also led to unacceptably large photocurrents from the red laser used to illuminate the QuasArs (38 ± 4 pA, steady state, 640 nm, 300 W/cm^2). Furthermore the off-time was undesirably slow ($\tau_{off} = 26.0 \pm 2.9$ ms). Based on experience with mutations in other rhodopsins, we introduced the mutation E154A, which only slightly decreased the peak photocurrent under blue illumination (to 2030 ± 100 pA, n = 10), but decreased the crosstalk from red illumination (to 10.5 ± 2.8 pA) and shortened τ_{off} to 16.0 ± 0.8 ms. This variant, termed CheRiff, showed excellent trafficking and neural activation at low illumination intensities.

The action spectrum of CheRiff was measured in HEK293 (n = 6 cells) with a monochromator (Till-Photonics Polychrome IV). 10 ms pulses of nearly equal photon fluxes (~ 2.5×10^{21} photons/s/m^2) were used across wavelengths. Small deviations in photon flux between wavelengths were corrected by dividing the recorded opsin response by the measured photon dose. For each cell, wavelengths were swept from blue-to-red and red-to-blue, and the responses were averaged.

4.4.3 DESIGN OF OPTOPATCH

We used 2A peptide ribosomal skip sequences as a means to achieve approximately stoichiometric co-expression. The porcine teschovirus-1 (P2A) sequence performed better than the Thosea asigna virus (T2A) sequence. Due to the greater need for high expression of the voltage indicator than the actuator, we placed the QuasAr gene before the P2A sequence and the CheRiff gene after (**Supplementary Fig. 4.15**).

In some applications one might wish to use the visible spectrum for other imaging modalities, e.g. for a reporter of Ca^{2+} or a GFP expression marker. In such cases, it is inconvenient to have GFP and mOrange2 fused to CheRiff and QuasArs, respectively. Removal of the eGFP tag from QuasArs resulted in poor membrane localization in neurons. To maintain the beneficial trafficking properties of the eGFP tag while eliminating the eGFP fluorescence, we mutated the eGFP chromophore from TYG to GGG using site-directed mutagenesis (Agilent). This mutation has been reported to preserve folding of eGFP [10]. We also made versions of Optopatch in which the mOrange2 was mutated to a non-fluorescent form by the mutation TYG to TAG.

Optopatch constructs were incorporated into lentiviral vectors under the CaMKIIα promoter, adapted from Addgene plasmid 22217.

4.4.4 NEURONAL CULTURE AND GENE DELIVERY

All procedures involving animals were in accordance with the National Institutes of Health Guide for the care and use of laboratory animals and were approved by the Institutional Animal Care and Use Committee at the institution at which they were carried out.

Primary neurons. Rat glial monolayers were prepared similarly to ref. [109]. Briefly, 10^6 dissociated hippocampal cells from P0 rat pups (Sprague Dawley, Tocris) [9] were plated on a 10 cm culture dish in glial medium GM, comprised of 15% FBS (Life), 0.4% (w/v) D-glucose, 1% glutamax (Life), 1% penicillin/streptomycin (Life) in MEM (Life). When the dish reached confluence (1-2 weeks), cells were split using trypsin onto glass-bottomed dishes (In Vitro Scientific, D35-20-1.5-N) coated with poly-D-lysine and matrigel (BD biosciences) at a density of (3500 cells/cm^2). After 3-6 days, glial monolayers were at or near confluence and the medium was replaced by GM with 2 μM cytarabine (cytosine-β-arabinofuranoside, Sigma). Dishes were maintained in GM with 2 μM cytarabine until use. Dishes were discarded if microglia or neurons were identified on the monolayers.

Hippocampal neurons from postnatal day zero rat pups were dissected and cultured in neurobasal-based medium (NBActiv4, Brainbits llc.) at a density of 30,000-40,000 cm^{-2} on the pre-established glial monolayers [9]. At one day *in vitro* (DIV), cytarabine was added to the neuronal culture medium at a final concentration of 2 μM to inhibit further glial growth [24].

Neurons were transfected on DIV 7 with the QuasArs or Optopatch plasmids via the calcium phosphate transfection method. Procedures closely followed ref. [74]. Measurements on neurons were taken between DIV 13-18.

For comparisons between CheRiff, ChR2 H134R and ChIEF, neurons were plated on glass-bottom dishes coated with poly-d-lysine (Sigma P7205) and matrigel (BD biosciences 356234) without pre-established glial monolayers. On DIV 3 cytarabine (2 μM) was added. Cells were transfected on DIV 7 with channelrhodopsin-eGFP fusions, in identical lentiviral plasmids with a CaMKIIα promoter. All comparison measurements were taken between DIV14-15 at room temperature (23 °C).

For TTX-induced homeostatic plasticity, primary neurons were transfected via the calcium phosphate method on DIV7. TTX (1 μM) was added on DIV 16. Excitability was measured on DIV 18 in Tyrodes medium with synaptic blockers (10 μM NBQX, 25 μM AP-V, 20 μM Gabazine).

hiPSC-derived neurons. Human iPSC-derived iCell neurons were purchased from Cellular Dynamics Inc. Neurons were tested negative for mycoplasma by the manufacturer. Neurons were thawed and resuspended in complete iCell Neuron Maintenance Medium (CM) following manufacturer protocols. Cells were then plated at a density 125,000/cm^2 on pre-established rat glial monolayers grown on glass-bottomed dishes. Medium was replaced 24 hours post plating with CM supplemented with 10 ng/mL BDNF (Peprotech). Thereafter, 50% media exchanges with CM were done every 5 days.

For TTX-induced homeostatic plasticity, hiPSC-derived neurons were transfected via the calcium phosphate method on DIV17. TTX (1 μM) was added on DIV 26. Excitability was measured on DIV 28 in Tyrodes medium with synaptic blockers (10 μM NBQX, 25 μM AP-V, 20 μM Gabazine).

For KCl-induced homeostatic plasticity, hiPSC-derived neurons were transfected on DIV 10. KCl (15 mM) was added from DIV 18 to DIV 21 (60 h). Excitability was measured on DIV 21 in Tyrodes medium with synaptic blockers (10 μM NBQX, 25 μM AP-V, 20 μM Gabazine).

Organotypic brain slice culture. Organotypic hippocampal slices cultures were prepared from postnatal day 6-8 Sprague-Dawley rats as described previously [153]. The brain was taken out and immediately placed in chilled dissection media. Transverse hippocampal slices were cut with 400 μm thickness and 4 to 6 slices were placed in a sterile culture plate insert (Millicell-CM, Millipore) in 6-well plates containing prewarmed media. Slices were biolistically transfected with a Helios Gene Gun (BioRad) at 2 days in vitro (DIV 2). Bullets were prepared using 12.5 μg of 1.6 μm gold particles and 80 – 100 μg of plasmid DNA. Slices were maintained until imaging at DIV 12-16.

Immediately prior to inverted imaging, slices were affixed to a nylon mesh weight and mounted upside down in a delta T brainslice adapter for inverted microscope imaging (Bioptechs). Artificial cerebrospinal fluid (ACSF) was bubbled with carbogen (95% O2, 5% CO2) and flowed over the slice at 1 mL/min at 23 °C.

4.4.5 Electrophysiology in neurons

Measurements were performed on primary cultures at 13 - 15 DIV. Experiments were conducted in Tyrode's solution containing 125 mM NaCl, 2.5 mM KCl, 3 mM $CaCl^2$, 1 mM $MgCl^2$, 10 mM HEPES, 30 mM glucose (pH 7.3) and adjusted to 305–310 mOsm with sucrose. Prior to imaging, neurons were incubated with 5 μM all-trans retinal for 30 minutes and then washed with Tyrode's solution.

Synaptic blockers were added to the imaging medium for measurements of single-cell electrophysiology. The blockers comprised NBQX (10 μM, Tocris), D(–)-2-amino-5-phosphonovaleric acid (AP5; 25 μM, Tocris), and gabazine (SR-95531, 20 μM, Tocris). For measurements of channelrhodopsin photocurrents in neurons, TTX (1 μM, Tocris) was included along with the synaptic blockers to prevent recruitment of voltage gated sodium channels. Patch clamp data was used if and only if access resistance was < 25 MΩ, and did not vary over the experiment. Recordings were terminated if membrane resistance changed by $> 10\%$. Experiments were performed at 23 ° C under ambient atmosphere unless otherwise noted.

Comparison of QuasArs to ArcLight A242. ArcLight A242 was prepared in an identical lentiviral plasmid driven by a CaMKIIα promoter and was transfected (DIV 7) in parallel with the QuasAr plasmids in paired cultures. We used a standard ArcLight imaging intensity of 10 W/cm^2 at 488 nm. QuasAr expressing neurons were imaged at two intensities (300 and 800 W/cm^2). All recordings were made on the setup described below ("Optopatch apparatus") at a 1 kHz frame rate and 60x magnification. Due to its slow kinetics at room temperature (**Supplementary Fig. 4.11**), ArcLight recordings were made at 34 °C to enhance SNR and to match previously published conditions [75]. For comparisons in organotypic brain slice, ArcLight was imaged at 50 W/cm^2 on an upright microscope to enable simultaneous patch clamp stimulation and recordings. Recordings were made at a 1 kHz frame rate as described below (**Section 4.4.7**) and were acquired at 34 °C.

4.4.6 IMMUNOSTAINING

Cultures were fixed immediately following data acquisition in a solution of 4% paraformaldehyde and 4% sucrose (w/v) in PBS, pH 7.4 at room temperature for 8 minutes. Fixed cultures were then washed three times in Dulbecco's PBS supplemented with Ca^{2+} and Mg^{2+} (DPBS), pH 7.4, prior to permeabilization and blocking in a solution of 0.1% (w/v) gelatin and 0.3% Triton-X-100 (v/v) in PBS, pH 7.4 (GTB) for 12-48 hours at 4 ° C.

For experiments using the sub-frame interpolation algorithm, primary cultures were fixed and stained using primary mouse monoclonal anti-ankyrin G (NeuroMab clone N106/36; 1:500), primary rabbit monoclonal anti-GFP (Abcam ab32146, lot YK011702CS, 1:1000), secondary goat anti-rabbit AlexaFluor 488 conjugated (Abcam ab150077, 1:500), and secondary goat anti-mouse AlexaFluor 647 conjugated (Abcam ab150115, 1:500) antibodies.

For experiments on human iPSC derived neurons, cultures were incubated with primary mouse anti-human nuclear antigen antibody (Millipore MAB1281 clone 235-1,1:500) in GTB overnight at 4 °C, then washed three times in DPBS, and incubated with rabbit anti-GFP AlexaFluor 488 conjugated (polyclonal, Life A21311, 1:300) and secondary antibody donkey anti-mouse AlexaFluor 647 (Life A31571, 1:300) in GTB overnight at 4 ° C. Cultures were washed three times in DPBS prior to mounting in DAPI Fluoromount-G (Southern Biotech).

4.4.7 OPTOPATCH MEASUREMENTS

Experiments were conducted on a home-built inverted fluorescence microscope, similar to the one described in the Supplementary Material to ref. [88]. Briefly, illumination from a red laser 640 nm, 140 mW (Coherent Obis 637-140 LX), was expanded and focused onto the back-focal plane of a 60× oil immersion objective, numerical aperture 1.45 (Olympus 1-U2B616). Imaging of brain slices was performed with a 20× water-immersion objective, numerical aperture 1.0 (Zeiss W Plan-Apo).

Illumination from a blue laser 488 nm 50 mW (Omicron PhoxX) was sent through an acousto-optic modulator (AOM; Gooch and Housego 48058-2.5-.55-5W) for rapid control over the blue intensity. The beam was then expanded and modulated by a digital micromirror device (DMD) with 608×684 pixels (Texas Instruments LightCrafter). The DMD was controlled via custom software (Matlab) through a TCP/IP protocol. The DMD chip was re-imaged through the objective onto the sample, with the blue and red beams merging via a dichroic mirror. Each pixel of the DMD corresponded to 0.65 μm in the sample plane. A 532 nm laser was combined with the red and blue beams for imaging of mOrange2. We wrote software to map DMD coordinates to camera coordinates, enabling precise optical targeting of any point in the sample.

To achieve precise optical stimulation of user-defined regions of a neuron, it was necessary to determine the mapping from pixels on the DMD to pixels on the camera. A uniform fluorescent film (exc. 488 nm, em. 515 nm) was loaded into the microscope. The DMD projected an array of dots of known dimensions onto the sample. The camera acquired an image of the fluorescence. Custom software located the centers of the dots in the image, and created an affine transformation to map DMD coordinates onto camera pixel coordinates.

A dual-band dichroic (Chroma zt532/635rpc) separated fluorescence of mOrange2 and Arch from excitation light. A 531/40 nm bandpass filter (Semrock FF01-531/40-25) and 495 nm longpass dichroic (Semrock FF495-Di03) was used for eGFP imaging, a 710/100 nm bandpass filter (Chroma, HHQ710/100) was used for Arch imaging, and a quad-band emission filter (Chroma ZET 405/488/532/642 nm) was used for mOrange2 imaging and pre-measurement calibrations. A variable-zoom camera lens (Sigma 18-200 mm f/3.5-6.3 II DC) was used to image the sample onto an EMCCD camera (Andor iXon+ DU-860), with 128 × 128 pixels. The variable zoom enabled imaging at a range of magnifications while maintaining the high light collection efficiency of the oil or water immersion objectives.

In a typical experimental run, images of mOrange2 and QuasAr fluorescence were first acquired at full resolution (128 × 128 pixels). Data was then acquired with 2 × 2 pixel binning to achieve a frame rate of 1,000 frames/s. For experiments with infrequent stimulation (once every 5 s), the red illumination was only on from 1 s before stimulation to 50 ms after stimulation to minimize photobleaching. Cumulative red light exposure was typically limited to < 5 min. per neuron, although continuous red light exposure for 30 minutes was well tolerated (**Supplementary Fig. 4.10**). Full resolution eGFP images were taken after functional recordings to prevent CheRiff excitation prior to the experiment.

Low magnification wide-field imaging was performed with a custom microscope system based around a 2×, NA 0.5 objective (Olympus MVX-2). Illumination was provided by six lasers 640 nm, 500 mW (Dragon Lasers 635M500), combined in three groups of two. Illumination was coupled into the sample using a custom fused silica prism, without passing through the objective. Fluorescence was collected by the objective, passed through an emission filter, and imaged onto a scientific CMOS camera (Hamamatsu Orca Flash 4.0). This microscope imaged a 1.2 × 3.3 mm field of view with 3.25 μm spatial resolution and 2 ms temporal resolution, or a 4 × 4 mm field of view with 10 ms temporal resolution. Blue illumination for channelrhodopsin stimulation was provided by a 473 nm, 1 W laser (Dragon Lasers), modulated in intensity by an AOM and spatially by a DMD (Digital Light Innovations DLi4130 – ALP HS). The DMD was re-imaged onto the sample via the 2× objective. The DMD provided targeted stimulation with excitation with 3.5 μm spatial resolution and 0.1 ms temporal resolution.

During an experimental run, we first acquired an image of a neuron using wide-field illumination at 640 nm to probe Arch fluorescence, and/or 532 nm to probe mOrange2 fluorescence. A user then selected one or more regions of interest on the image of the neuron, and specified a timecourse for the illumination in each region. The software mapped the user-selected pixels onto DMD coordinates and delivered the illumination instructions to the DMD.

4.4.8 DATA ANALYSIS

Statistics. All error ranges represent standard error of the mean, unless otherwise specified. For two-sample comparisons of a single variable, data was tested for normality using the Shapiro-Wilks test. If the data was detectably non-Gaussian, we performed a nonparametric Mann-Whitney U test. Otherwise we performed a two-tailed student's t-test. Channelrhodopsin multi-way comparisons of a single variable were made using a one-way ANOVA with Dunnett's post-hoc test, using CheRiff as a reference. No channelrhodopsin dataset was detectably non-Gaussian (Shapiro-Wilks). Probabilities of the null hypothesis $P < 0.05$ were judged to be statistically significant.

Extracting fluorescence from movies. Fluorescence values were extracted from raw movies in one of two ways. One approach used the maximum likelihood pixel weighting algorithm described in ref. [88]. Briefly, the fluorescence at each pixel was correlated with the whole-field average fluorescence. Pixels that showed stronger correlation to the mean were preferentially weighted. This algorithm automatically found the pixels carrying the most information, and de-emphasized background pixels. This approach was used for all experiments in cultured neurons. In images containing multiple neurons, the segmentation was performed semi-automatically using the independent components-based approach of ref. [114].

Alternatively, a user defined a region comprising the cell body and adjacent processes, and calculated fluorescence from the unweighted mean of pixel values within this region. With the improved trafficking of the QuasAr mutants compared to Arch, the maximum likelihood pixel-weighting algorithm was only marginally superior to manual definition of an ROI (**Supplementary Fig. 4.9**). For calculations of $\Delta F/F$ in culture, background fluorescence from a cell-free region was subtracted from the baseline fluorescence of the cell. In measurements in brain slice, fluorescence was calculated from manually defined ROIs with equal pixel weighting and no background subtraction or correction for photobleaching.

Precision of optically recorded AP timing. To determine the temporal precision of the QuasAr indicators, we used the sub-frame interpolation algorithm of refs. [39, 129] to infer the timing with which the fluorescence reached 70% of maximum at each AP, and compared to simultaneously acquired high time-resolution patch clamp recordings. Root-mean-square (r.m.s.) temporal jitter was 44 μs for QuasAr1 (n = 97 APs) and 61 μs for QuasAr2 (n = 99 APs). This jitter reflects the combined errors in timing intrinsic to the optical measurement (shot-noise and distortion of the waveform by the reporter) and errors introduced by temporal discretization of the camera frames and the sub-frame interpolation. Thus optical recordings with QuasArs can determine spike timing with precision much greater than the camera exposure time.

Fitting channelrhodopsin photocurrents. Photocurrents of the channelrhodopsins were characterized following the protocols in ref. [108]. Briefly, peak photocurrents in response to a light pulse (488 nm, 0.5W/cm^2, 1 s duration) were identified by first smoothing the traces using robust Loess method with a filter width of 2 ms, and then finding the extremum of the filtered trace after laser onset and subtracting the baseline current. Time to peak (t_{on}) was defined as the time between light onset and peak photocurrent of the filtered trace. The steady-state photocurrent was found by fitting a monoexponential curve to the filtered trace from 2 ms after the peak until laser offset. The offset of this fit was defined as the steady-state photocurrent. The time constant of this fit was defined as the desensitization rate (τ_{des}).The channel closure rate (τ_{off}) in response to a light pulse (488 nm, 0.5W/cm^2, 5 ms duration) was measured by fitting a monoexponential to the decay of the photocurrent after light offset.

Illumination intensities for 50% effective light power density [108] (EPD50, **Supplementary Table 4.4**) values were determined from measurements of peak photocurrents versus a series of whole field illumination intensities. For each cell, peak photocurrents at each intensity were first normalized by the maximum peak photocurrent. The resulting curves were then fit with a simple binding model ($Y = B_{max} \times X / (EPD50 + X)$). The reported EPD50s are the average of the fit parameters from n = 5 cells.

4.4.9 SUB-FRAME INTERPOLATION OF AP TIMING

The sub-frame interpolation algorithm consists of a series of computational image-processing steps (**Supplementary Fig. 4.18**). Each step may be modified to account for experiment-specific attributes of the data.

A neuron was induced to fire through repeated optical stimulation of a user-selected subcellular compartment (typically soma or dendrite). We typically observed 5% photobleaching over a 40 s acquisition. Photobleaching was typically dominated by non-specific background fluorescence, rather than by photobleaching of QuasAr, and often photobleaching did not follow a simple single-exponential decay. The photobleaching baseline was constructed from the whole-field intensity by a sliding minimum filter, followed by a sliding mean filter. Each frame of the movie was then corrected by dividing by this baseline.

QuasAr fluorescence intensity $F(t)$ was determined either by the regression algorithm described before [88] or by whole-field average intensity. Both procedures gave similar results, with slightly better signal-to-noise ratio returned by the regression algorithm (**Supplementary Fig. 4.9**).

Determination of spike times was performed iteratively. A simple threshold-and-maximum procedure was applied to $F(t)$ to determine approximate spike times, $\{T_0\}$. Waveforms in a brief window bracketing each spike were averaged together to produce a preliminary spike kernel $K_0(t)$. We then calculated the cross-correlation of $K_0(t)$ with the original intensity trace $F(t)$. Whereas the timing of maxima in $F(t)$ was subject to errors from single-frame noise, the peaks in the cross-correlation, located at times $\{T\}$, were a robust measure of spike timing. A movie showing the mean AP propagation was constructed by averaging movies in brief windows bracketing spike times $\{T\}$. Typically 100 – 400 APs were included in this average. The AP movie had high signal-to-noise ratio, but did not clearly show signal propagation.

We applied spatial and temporal linear filters to further decrease the noise in AP movie. The spatial filter consisted of convolution with a Gaussian kernel, typically with a standard deviation of 1 pixel. The temporal filter was based upon Principal Components Analysis (PCA) of the set of single-pixel time traces. The time trace at each pixel was expressed in the basis of PCA eigenvectors. Typically the first 5 eigenvectors were sufficient to account for >99% of the pixel-to-pixel variability in

AP waveforms, and thus the PCA eigendecomposition was truncated after 5 terms. The remaining eigenvectors represented uncorrelated shot noise (**Supplementary Fig. 4.18b**). Projections of the movie onto the PCA eigenvectors only showed spatial features above noise for the first 5 eigenvectors (**Supplementary Fig. 4.18c** inset). To verify that the spatial and PCA filtering did not distort the underlying AP waveforms, we compared mean AP waveforms in subcellular compartments before and after the smoothing steps (**Supplementary Fig. 4.18d**). We observed no systematic deviations in the AP waveforms in the axon, soma, or dendrites.

The user then set a threshold depolarization to track (represented as a fraction of the maximum fluorescence transient), and a sign for dV/dt (indicating rising or falling edge). We chose 50% maximal depolarization on the rising edge. The filtered data was fit with a quadratic spline interpolation and the time of threshold crossing was calculated for each pixel to create a map of the AP delay (**Supplementary Fig. 4.18e**).

The sub-frame timing precision of the algorithm was calibrated by patch clamp measurements. Optically induced APs were recorded simultaneously via QuasAr1 fluorescence in the soma and by conventional patch clamp, also in the soma (**Supplementary Fig. 4.18f**). The r.m.s. error in timing was 54 μs in this instance, and did not show systematic bias at the frame boundaries.

The fits were converted into movies showing AP propagation as follows. Each pixel was kept dark except for a brief flash timed to coincide with the timing of the user-selected AP feature at that pixel. The flash followed a Gaussian timecourse, with amplitude equal to the local AP amplitude, and duration equal to the cell-average time resolution, σ. Frame times in the sub-frame interpolation movies were selected to be 2-fold shorter than σ.

Occasionally it was possible to enhance the spatial resolution of the high temporal resolution movies by mapping the timing data onto a higher spatial resolution static image of fluorescence of eGFP (from the CheRiff-eGFP fusion, **Supplementary Fig. 4.18g**) or of QuasAr1. The pixel matrix of the sub-frame interpolated movie was expanded to match the dimensions of the high resolution image and the amplitude at each pixel was then set equal to the mean brightness at that pixel. Selected frames from the resulting movie showed AP initiation at the axon initial segment in the first two frames (**Supplementary Fig. 4.18h, Supplementary Movie 4.7.4**). To assemble the color movies (**Fig. 4.3e**, **Supplementary**

Fig. 4.18, Supplementary Movies 4.7.4- 4.7.6), the timing signal was assigned to a colormap which was overlayed on a gray-scale image of mean QuasAr fluorescence. Optionally, the optically stimulated region of the cell was highlighted in blue.

4.5 Supplementary Figures

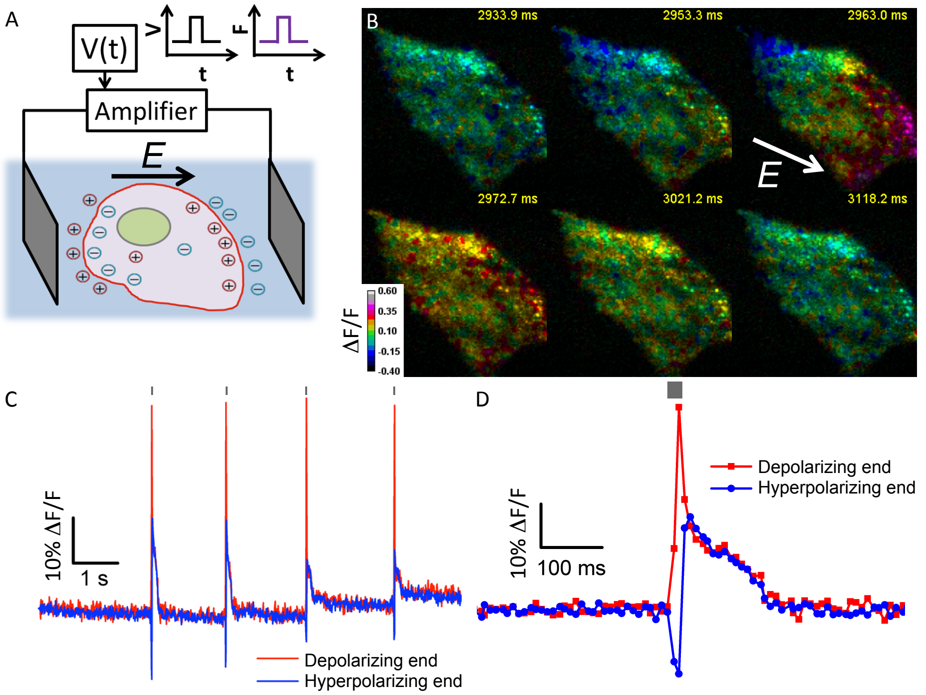

Figure 4.6: Induced transmembrane voltage (ITV) in Arch-expressing HeLa cells. A) Experimental setup, showing two platinum electrodes placed on either side of a transfected cell. V(t) represents the pulse generator and high-voltage amplifier. B) Frames from a movie of a HeLa cell expressing QuasAr1. The cell was stimulated with an electrical pulse (20 ms, 50 V/cm). The images show the fluorescence response (ΔF/F). The arrow labeled 'E' indicates the direction of the electric field. C) Fluorescence of the cell poles during the ITV experiment shown in (B). Gray marks above the fluorescence traces indicate timing and duration of the ITV pulses. D) Expanded view of one fluorescence intensity peak from (C).

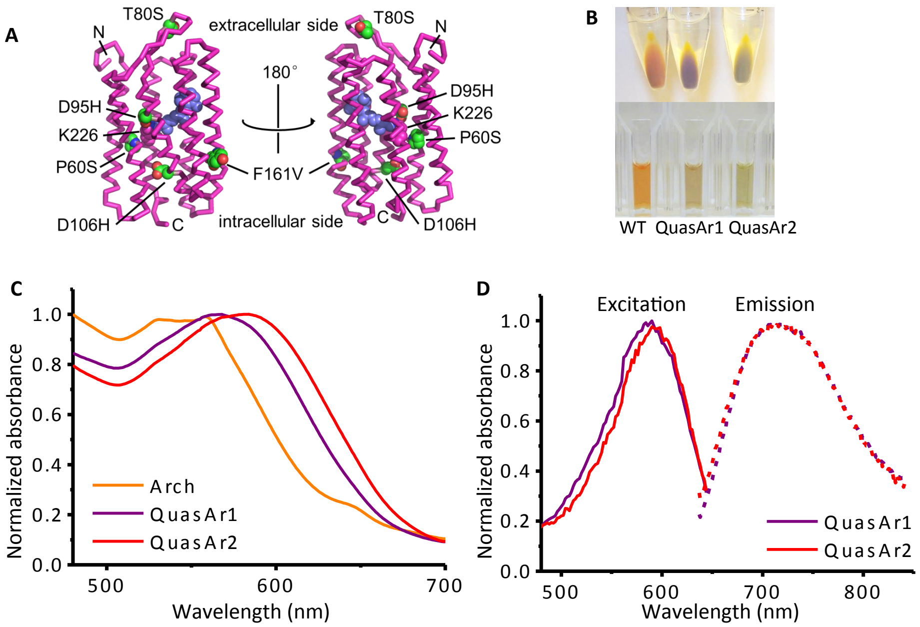

Figure 4.7: Structural and spectroscopic properties of QuasArs. A) Locations of mutations in QuasAr1, modeled on the crystal structure of Arch-2 (PDB: 2EI4) [36]. Arch-2 has 90% amino acid identity with Arch-3. The retinal chromophore is colored blue and mutations are colored green. B) Top: Images of *E. coli* pellets expressing Arch, QuasAr1, and QuasAr2. Bottom: Images of solubilized protein. C) Absorption spectra of Arch, QuasAr1 and QuasAr2, measured on solubilized protein. D) Excitation and emission spectra measured on QuasAr1 and QuasAr2. Arch was too dim to measure in the fluorimeter. Emission spectra were recorded with $\lambda_{exc} = 600$ nm. Excitation spectra were measured with $\lambda_{em} = 750$ nm.

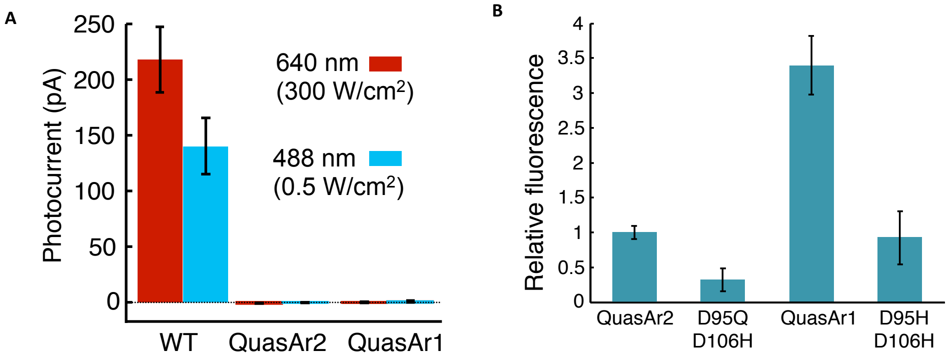

Figure 4.8: Photophysics of QuasArs in mammalian cells. A) In cultured rat hippocampal neurons, wild-type Arch generated photocurrents of 220 ± 30 pA (n = 6 cells) under red illumination (1 s, 640 nm, 300 W/cm^2) and 140 ± 25 pA under blue light (1 s, 488 nm, 500 mW/cm^2). Steady-state photocurrents were calculated by averaging the current over the last 0.25 seconds of light exposure and subtracting the holding current (cells held at -65 mV) in the dark. These photocurrents hyperpolarized cells by 25 ± 4 mV and 19 ± 3 mV, respectively. Neither QuasAr1 (n = 9 cells) nor QuasAr2 (n = 7 cells) generated detectable steady-state photocurrents under either illumination condition, nor under red illumination at up to 900 W/cm^2. B) Comparison of fluorescence between QuasAr mutants and Arch double mutants, expressed as eGFP fusions in HEK cells. The double mutants had mutations at the locations of the proton acceptor (Asp95) and proton donor (Asp106) to the Schiff base. QuasAr1 includes mutations D95H, D106H, and QuasAr2 includes mutations D95Q, D106H. The three additional backbone mutations in the QuasArs (P60S, T80S, F161V) increased brightness relative to the double mutants. Fluorescence of each Arch mutant was measured with excitation at 640 nm and emission from 660 – 760 nm. To control for variation in expression level, fluorescence was normalized by eGFP fluorescence (λ_{exc} = 488 nm, λ_{em} = 510 – 550 nm). Error bars represent s.e.m. for measurements on n = 5 - 10 cells.

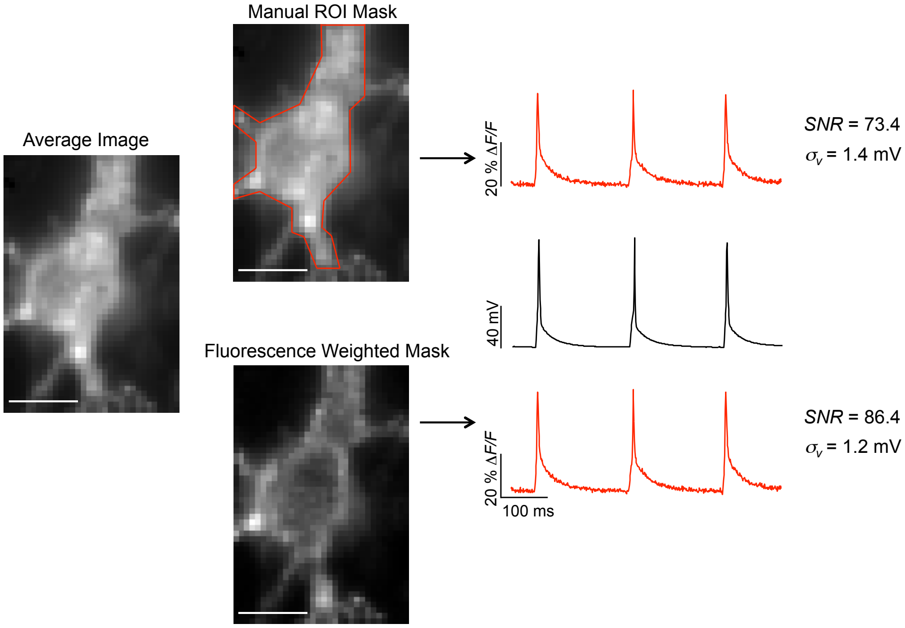

Figure 4.9: Extraction of fluorescence traces from QuasAr movies. Fluorescence can either be calculated by manually defining a region of interest (ROI; top row), or by preferentially weighting the pixels whose intensity co-varies with the whole-field average (bottom row) [88]. The noise in the fluorescence trace when scaled to match the electrical recording is denoted σ_v. With the improved trafficking of the QuasAr mutants compared to Arch, the automated technique gave only slightly higher SNR than manual definition of the ROI. The technique makes no use of the electrode readout. Cell shown is the source of the data in **Fig. 4.1g**. All comparisons of SNR in culture were made on measurements taken with the same 60x objective, collected on the same EMCCD (**Methods Section 4.4**), and extracted using this automated technique. For recordings on cultured neurons, values of ΔF/F were calculated after subtracting background autofluorescence from a cell-free region of the field of view. This background subtraction was not performed on recordings in tissue.

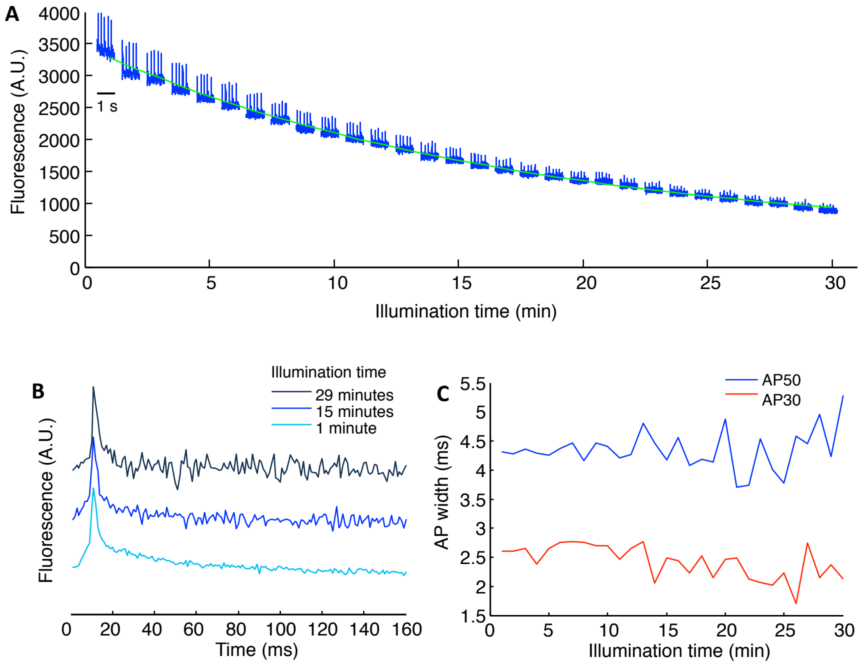

Figure 4.10: Photobleaching of QuasAr2 and test for red light induced phototoxicity. A) Fluorescence traces from a neuron expressing QuasAr2 and CheRiff (Optopatch2, described below), with APs induced via blue light activation of the CheRiff. Optogenetic stimulation was preferable to manual patch clamp due to the poor stability of patch connections over long-term measurements. The cell was illuminated for 30 minutes continuously at 640 nm, 300 W/cm² and probed at 60 s intervals with blue light to induce a burst of APs (5 pulses of 10 ms, 5 Hz, 20 mW/cm²). The cell fired APs with 100% fidelity over the recording period, though the signal-to-noise ratio decreased as the QuasAr2 fluorescence dropped. B) Fluorescence traces of APs at the beginning, middle, and end of the recording in (A). Each trace in (B) is an average of the 5 APs elicited during that time point. C) AP widths measured at 30% and 50% recovery from peak fluorescence deviation. APs did not show a detectable change in width over the 30-minute recording.

Figure 4.11 ***(following page)*****: Comparison of voltage-indicating properties of QuasArs and ArcLight A242 in culture.** A) Fluorescence as a function of membrane voltage in HEK293T cells. ArcLight showed voltage sensitivity of -32 ± 3% ΔF/F per 100 mV (n = 7 cells), comparable in magnitude to QuasAr1 and 2.8-fold smaller than QuasAr2. B) Response of ArcLight to steps in membrane voltage. ArcLight showed bi-exponential kinetics in response to rising or falling voltage steps (**Supplementary Table 4.2**). Mean half-response times were 42 ± 8 ms and 76 ± 5 ms on rising and falling edges at 23 °C (n = 6 cells) and 11 ± 1 and 17 ± 2 ms on rising and falling edges at 34 °C (n = 7 cells). C) Step responses of ArcLight and QuasArs overlaid on the same time axis at 23 °C (top) and 34 °C (bottom). D) Continuous illumination of a neuron expressing ArcLight (488 nm, 10 W/cm²) led to photobleaching with a time constant of 70 s. Inset: Low-magnification image of the neuron. Scale bar 20 μm. Cyan box shows field of view used for high-speed (1 kHz frame rate) movies of fluorescence dynamics. Fluorescence was calculated using the same pixel weighting algorithm used for QuasAr data (**Supplementary Fig. 4.9**).

E) Single-trial fluorescence response of ArcLight (blue) and QuasAr2 (red) to a single AP (black), recorded at 34 °C and a 1 kHz frame rate. ArcLight reported action potentials with an amplitude of ΔF/F = -2.7 ± 0.5% (n = 5 cells) and a single-trial signal-to-noise ratio (SNR) of 8.8 ± 1.6 (488 nm, 10 W/cm²). ArcLight distorted the AP waveforms to have a width of 14.5 ± 3.0 ms at 70% maximal fluorescence deviation, compared to the true width of 1.3 ± 0.1 ms simultaneously recorded with a patch pipette. QuasAr2 reported APs at 34 °C and 23 °C with comparable single-trial SNR (SNR at 34 °C: 41 ± 3, 300 W/cm², n = 8 cells).

Figure 4.11: (continued)

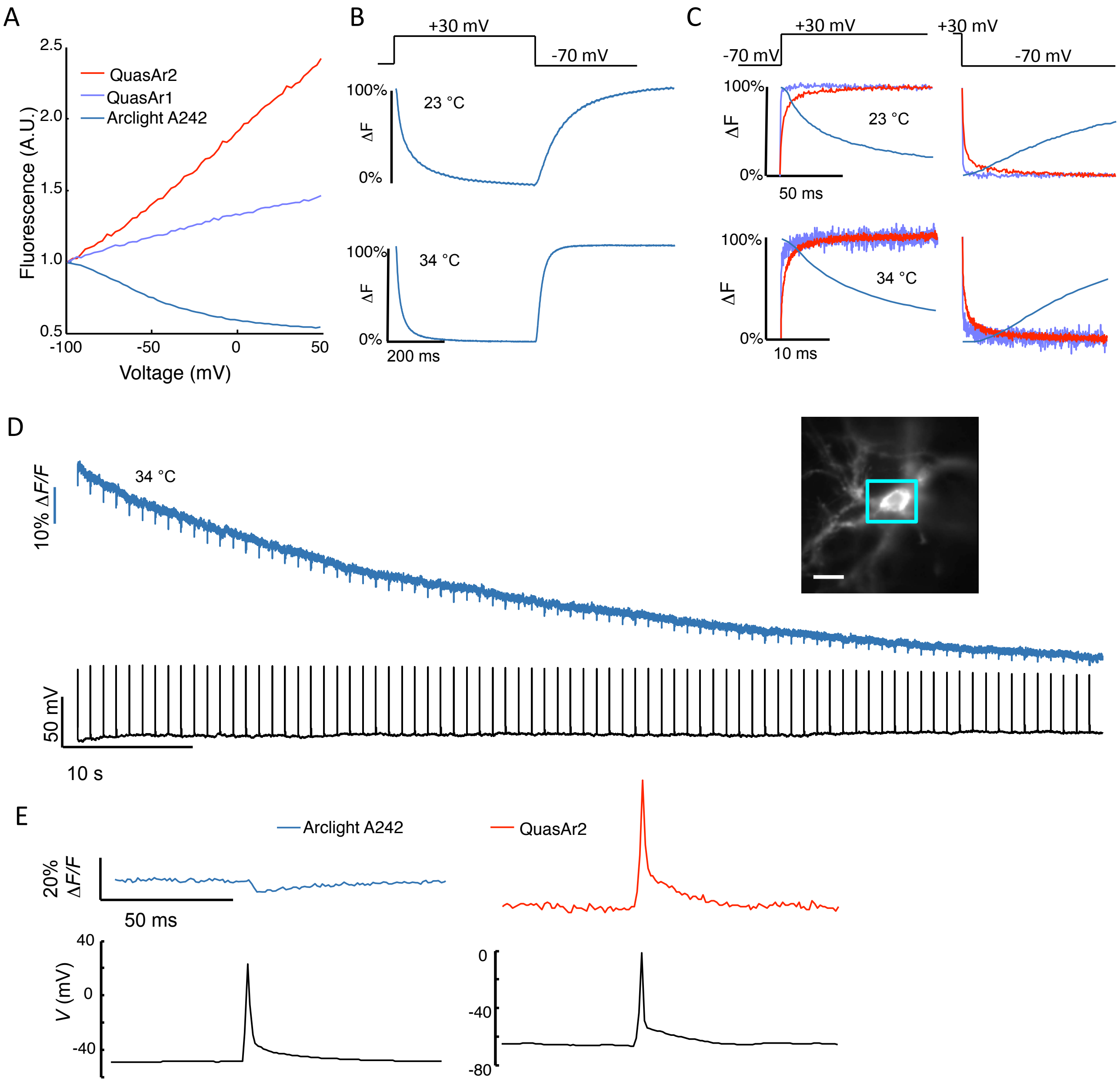

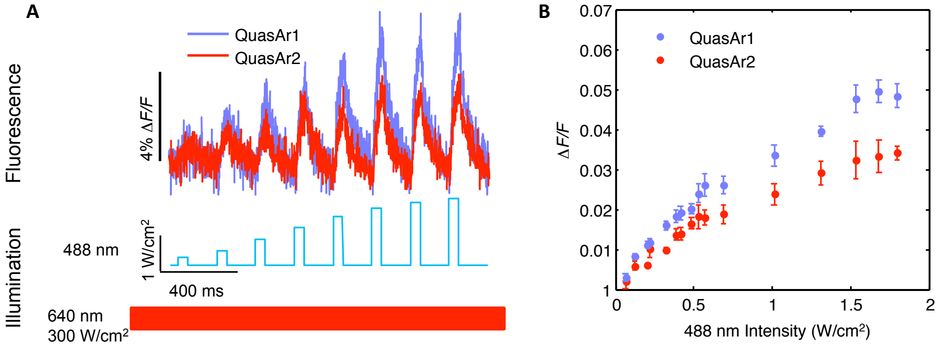

Figure 4.12: Quantification of optical crosstalk of blue illumination into QuasAr fluorescence. A) Effect of blue illumination on QuasAr fluorescence. HEK293T cells expressing QuasAr1 or QuasAr2 (with dark mOrange2, see **Methods Section 4.4**) were exposed to continuous excitation at 640 nm (300 W/cm²) and pulses of illumination at 488 nm (50 ms, 5 Hz). The intensity of the blue pulses increased from 0.06 to 1.8 W/cm². B) Quantification of crosstalk. Illumination with blue light at maximum intensity used to excite CheRiff (0.2 W/cm²) increased QuasAr1 fluorescence by 1.1% and QuasAr2 fluorescence by 0.6%. Initiation of precisely timed APs with existing channelrhodopsins required whole-cell illumination at 0.5 to 2 W/cm² (ref. [108]). Blue illumination at 1 W/cm2 increased QuasAr1 fluorescence by 3.4% and QuasAr2 fluorescence by 2.4%, unacceptably high levels of optical crosstalk. Error bars represent s.e.m. for n = 5 cells for each QuasAr. Quantification is given in **Supplementary Table 4.5**.

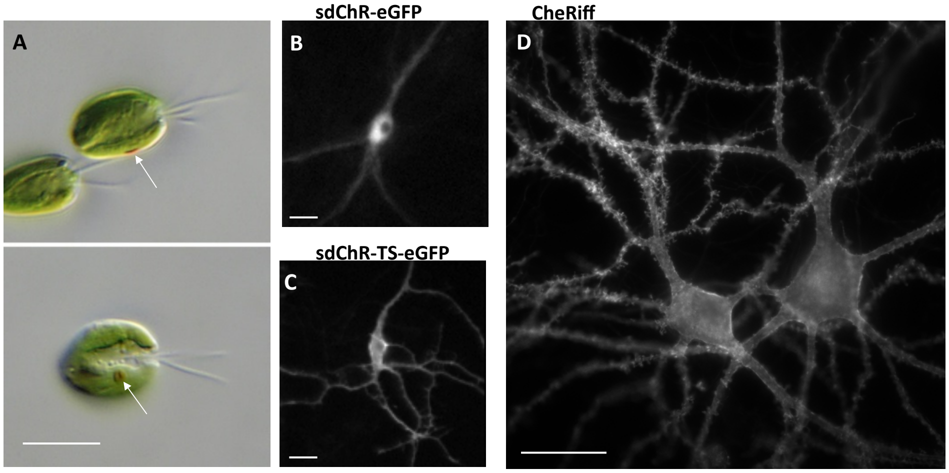

Figure 4.13: Improvements in trafficking leading to CheRiff. A) Light micrographs (DIC) of *Scherffelia dubia* (strain CCAC 0053) in side view (top) and face view (bottom). Arrows mark eyespots (red). Scale bar 10 μm. Strain and micrographs courtesy of CCAC [`http://www.ccac.uni-koeln.de/`] and Sebastian Hess (Cologne Biocenter), respectively. B) Image of a cultured neuron expressing wild-type *Scherffelia dubia* Channelrhodopsin (sdChR). SdChR typically aggregated and formed puncta in the soma. Scale bar 25 μm. C) Image of a neuron expressing sdChR with an additional trafficking sequence from Kir2.1 between the C-terminus of sdChR and the N-terminus of eGFP (**Methods Section 4.4**). This trafficking sequence substantially reduced intracellular puncta. Scale bar 25 μm. D) Two neurons expressing CheRiff. Inclusion of the E154A mutation reduced red light sensitivity and reduced τ_{off} while maintaining excellent membrane trafficking and blue light sensitivity. Scale bar 25 μm.

Figure 4.14 *(following page)*: Spectroscopic and kinetic properties of CheRiff. A) Photocurrents measured in response to a 1 second 488 nm light pulse with intensity 500 mW/cm², sufficient to open all the channels. Comparisons were made on matched rat hippocampal cultures, DIV 14-15. Expression was driven by a CaMKIIα promoter in identical plasmid backbones. See **Methods Section 4.4** for details on cell culture. B) Components of channelrhodopsin current elicited by a step in blue light. I_{pk} is the difference between baseline current and peak current. t_{on} is the time between light onset and peak current. τ_{des} is the desensitization time constant determined by a single-exponential fit to the current decay after the peak. I_{ss} is steady-state photocurrent. τ_{off} is the channel closing time constant determined by a single-exponential fit to the current decay after the illumination ceases. C) Peak (I_{pk}) and steady-state (I_{ss}) photocurrents in neurons expressing CheRiff ($n = 10$ cells), ChR2 H134R ($n = 8$ cells), and ChIEF ($n = 6$ cells). CheRiff generated peak photocurrent of 2.0 ± 0.1 nA, approximately 2-fold larger than the peak photocurrents of ChR2 H134R (1.1 ± 0.1 nA, $P < 0.001$) or ChIEF [95] (0.9 ± 0.1 nA, $P < 0.001$). CheRiff also generated significantly larger steady-state photocurrents (1.3 ± 0.08 nA) than ChR2 H134R (0.68 ± 0.07 nA, $P < 0.001$) or ChIEF (0.81 ± 0.10 nA, $P < 0.001$).
We further compared the kinetics of CheRiff to ChR2 H134R and to ChIEF under standard channelrhodopsin illumination conditions (488 nm, 500 mW/cm²) at 23 °C in cultured neurons. D) In response to a step in illumination, CheRiff reached peak photocurrent in 4.5 ± 0.3 ms ($n = 10$ cells), significantly faster than ChR2 H134R (8.9 ± 0.5 ms, $n = 8$ cells, $P < 0.001$) or ChiEF (18 ± 1.5 ms, $n = 6$ cells, $P < 0.001$). E) Under continuous illumination CheRiff partially desensitized with a time constant of 400 ms. ChR2 H134R and ChIEF desensitized significantly faster (39 ± 4 ms, $n = 8$ cells, $P < 0.001$, and 49 ± 8 ms, $n = 5$ cells, $P < 0.001$, respectively). F) τ_{off} was measured in response to a 5 ms illumination pulse (500 mW/cm²) as in ref. **REF**. Channel closing time constant was comparable between CheRiff and ChIEF (16 ± 0.8 ms, $n = 9$ cells, and 15 ± 2 ms, $n = 6$ cells, respectively, $P = 0.94$), and faster than ChR2 H134R (25 ± 4 ms, $n = 6$ cells, $P < 0.05$). Error bars represent s.e.m. Statistical significance determined by one way ANOVA with Dunnett's post hoc test using CheRiff as the reference. * $P < 0.05$; ** $P < 0.01$; *** $P < 0.001$. **Supplementary Table 4.4** contains a summary of the comparisons between CheRiff, ChR2 H134R, and ChIEF. G) Activation of CheRiff by red light used for imaging QuasArs (640 nm, 900 W/cm²). Top: Under current-clamp ($i = 0$) in a neuron expressing CheRiff, pulses of red light led to a small steady depolarization of 3.1 ± 0.2 mV ($n = 5$ cells). Bottom. Under voltage-clamp ($V = -65$ mV), pulses of red light led to a small inward photocurrent of 14.3 ± 3.1 pA ($n = 5$ cells).

Figure 4.14: (continued)

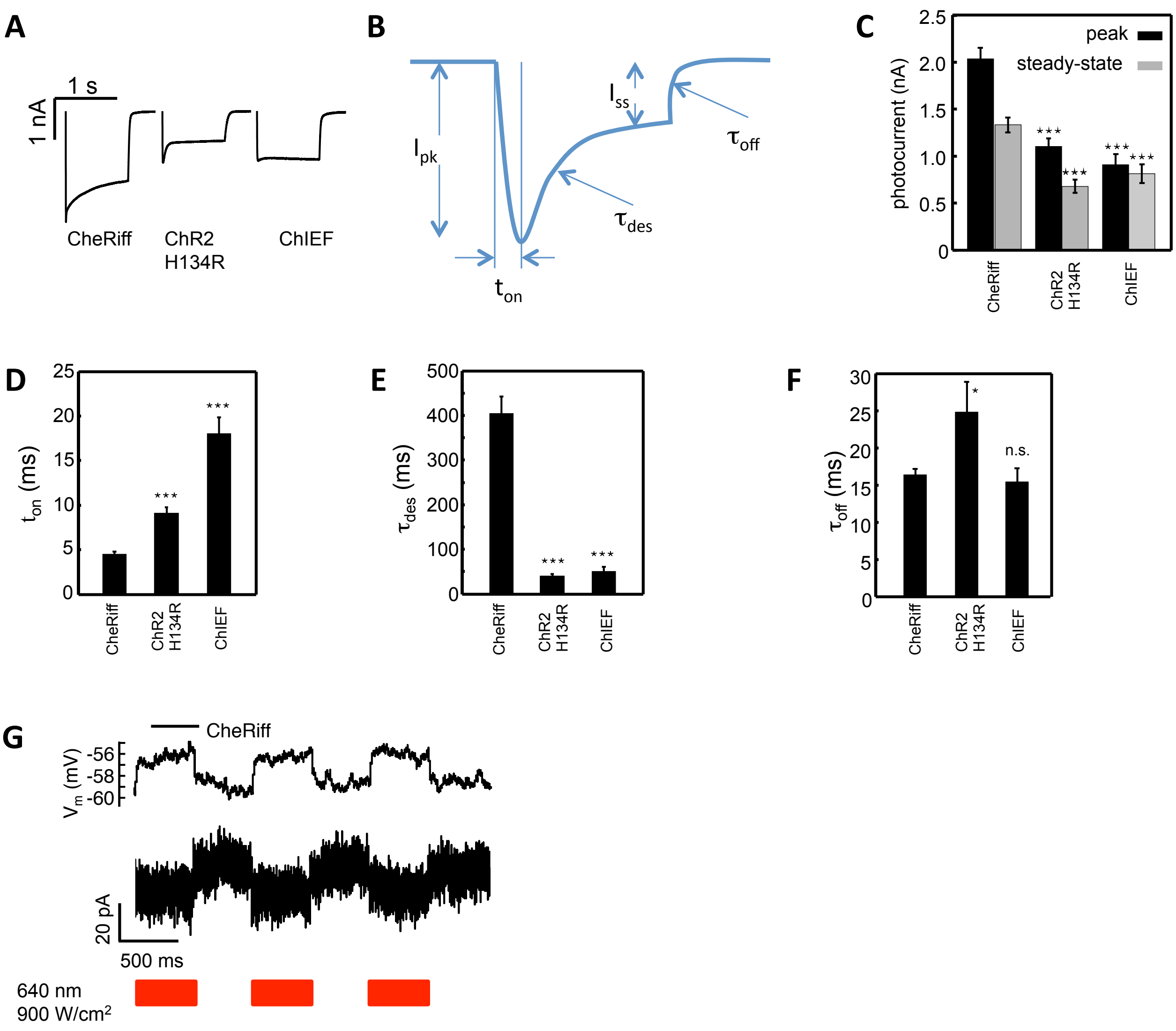

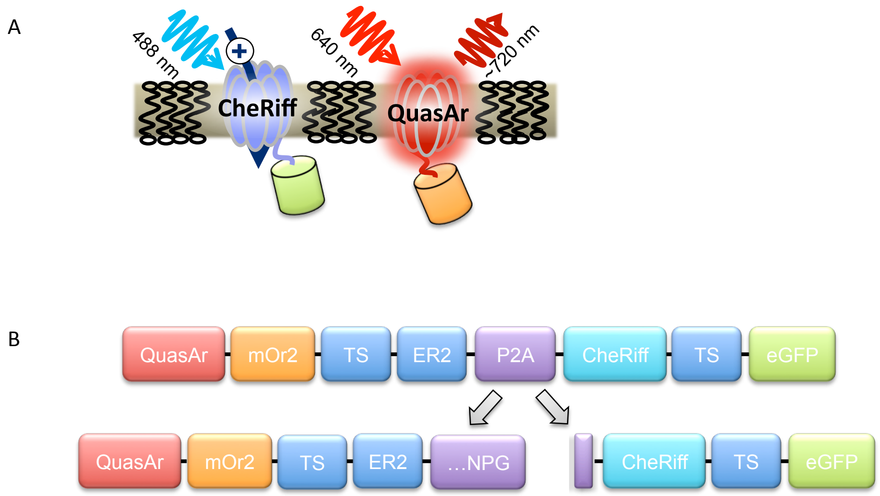

Figure 4.15: Optopatch construct. A) The optopatch constructs led to co-expression of CheRiff and QuasAr in the cell plasma membrane. CheRiff mediates blue light-induced depolarization. QuasAr reports voltage fluctuations under 640 nm excitation with emission between 660 nm and 760 nm. B) The bicistronic vector consists of a QuasAr fused to mOrange2 with the TS and ER2 trafficking motifs followed by a porcine teschovirus-1 (P2A) sequence, and ending with CheRiff fused to eGFP. The P2A peptide causes a ribosomal skip, leading to approximately stoichiometric co-expression of the actuator and reporter.

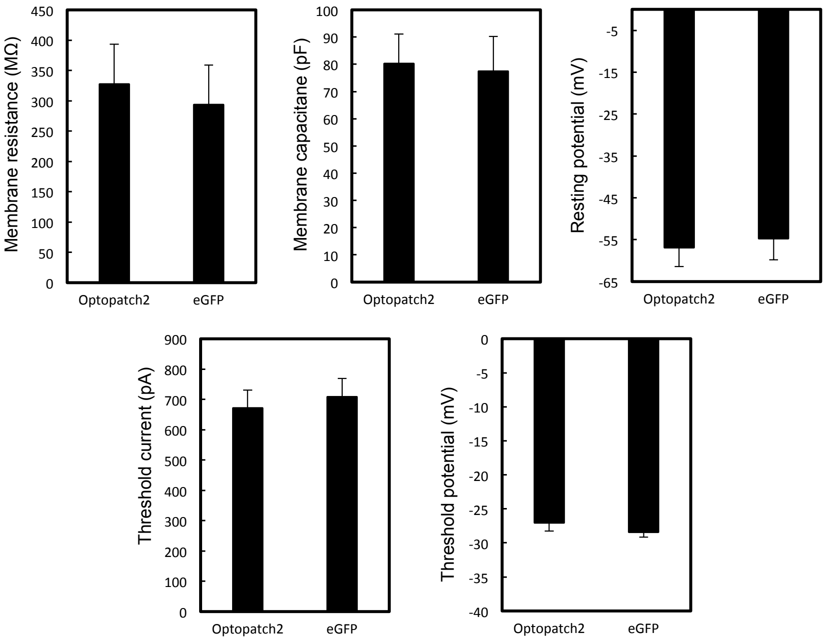

Figure 4.16: Effect of Optopatch expression on membrane electrical properties. Matched cultures were transfected via calcium phosphate on DIV 7 with either cytoplasmic eGFP or Optopatch2 in identical plasmids with a CaMKII promoter. Expressing cells (n = 8 Optopatch2, n = 7 eGFP, DIV 15) were measured via whole-cell patch clamp. There was no significant difference in membrane resistance (P = 0.72), membrane capacitance (P = 0.87), or resting potential (P = 0.31) between Optopatch2 and eGFP expressing cells. Threshold current and potential for action potential initiation were determined by applying increasing steps in current (400-850 pA, 5 ms duration, repeated at 5 Hz). There was no significant difference in threshold current (P = 0.67) or potential (P = 0.38) between Optopatch2 and eGFP expressing cells. Error bars represent s.e.m. Statistical significance determined by two-tailed student's t-test or Mann–Whitney U test.

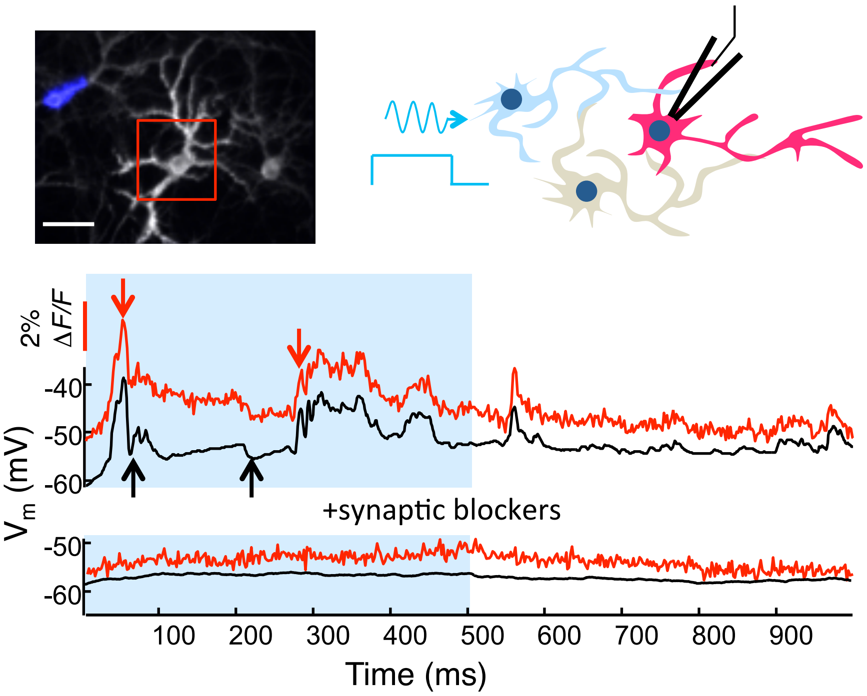

Figure 4.17: Optopatch measurements of post-synaptic responses. Top: Three cells expressing Optopatch2 were imaged via eGFP fluorescence (after conclusion of the experiment). The blue shading shows the region optically stimulated in the leftmost cell (488 nm, 35 mW/cm², 500 ms pulses) to stimulate network activity. The red square shows the camera field of view used for imaging QuasAr2 fluorescence. The membrane voltage of the cell within this region was simultaneously monitored via QuasAr2 fluorescence and via whole-cell patch clamp. Middle: Simultaneous patch clamp (black line) and fluorescence (red line) recording of subthreshold activity in the postsynaptic cell (640 nm exc., 1200 W/cm²). The presence of optically induced EPSPs (red arrows) and IPSPs (black arrows) in the same cell indicates recruitment of other cells in the network. Bottom: Synaptic blockers (10 μM NBQX, 20 μM gabazine, 25 μM AP-V) eliminated the response in the postsynaptic cell.

Figure 4.18 ***(following page)*****: Sub-frame interpolation highlights subcellular timing differences in AP initiation.** A) Patterned optical excitation (blue region) was used to induce between 100 and 400 APs. Fluorescence movies of individual APs were acquired at 1,000 frames/s, temporally registered and averaged. The sub-threshold depolarization is greatest at the location of the optical stimulus, and propagates passively through the cell until it crosses the AP initiation threshold. B) The movie of a mean AP was passed through a mild spatial filter, and then Principal Components Analysis (PCA) was applied to AP waveforms at individual pixels. The first 5 PCA eigenvectors accounted for $> 99\%$ of the pixel-to-pixel variation in AP waveforms; the remaining eigenvectors were noise. C) Cumulative variance of the fluorescence signal accounted for by the first n eigenvectors. In this example the cumulative variances explained by the first five eigenvectors were: 97.8%, 98.8%, 98.9%, 99.0%, and 99.1%. Inset shows projection of the spike movie onto each of the first eight eigenvectors. D) Comparison of AP waveforms before and after the spatial and PCA smoothing operations. Black lines represent original movie, colored lines represent filtered data recorded in the axon (cyan), soma (green), and dendrites (red). E) Map of AP timing, calculated for the cell shown in (A) and (D). Here the timing was defined as the time to reach 50% of maximum intensity on the rising edge of the AP. Note the early timing in the axon initial segment on the left. F) Absolute accuracy of timing extracted by the sub-frame interpolation algorithm for voltage at the soma, compared to a simultaneously acquired patch clamp recording. The r.m.s. error between optically inferred and electrically recorded timing was 54 s in this example. Note the absence of systematic offsets at the frame boundaries. G) High-resolution image of eGFP fluorescence, indicating CheRiff distribution. H) Frames from a sub-frame interpolated movie formed by mapping the timing information in (E) onto the high spatial resolution image in (G). White arrows mark zone of AP initiation in the presumed axon initial segment. Data is from the same cell as in **Fig. 4.3e**, with images rotated 90 °.

Figure 4.18: (continued)

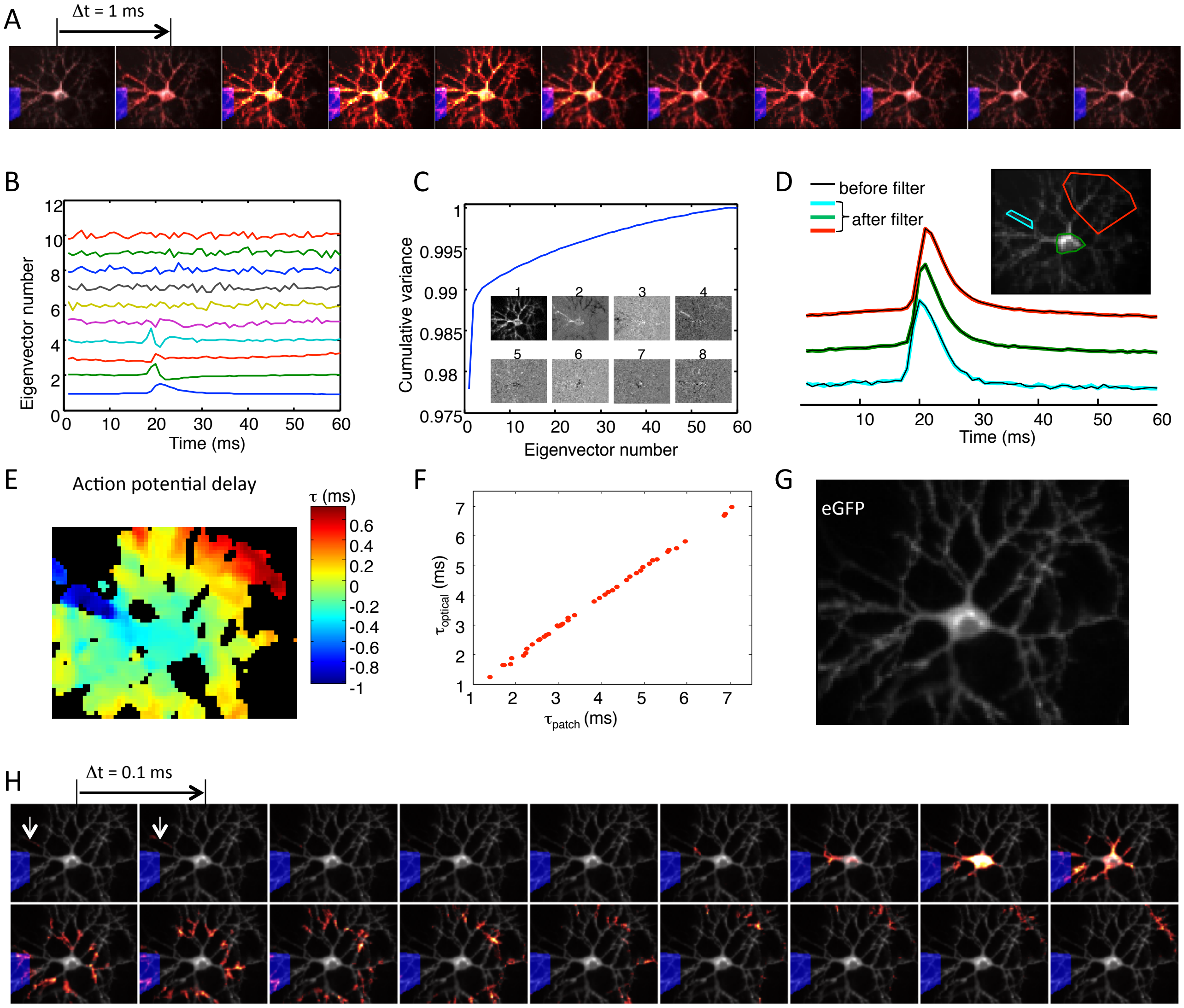

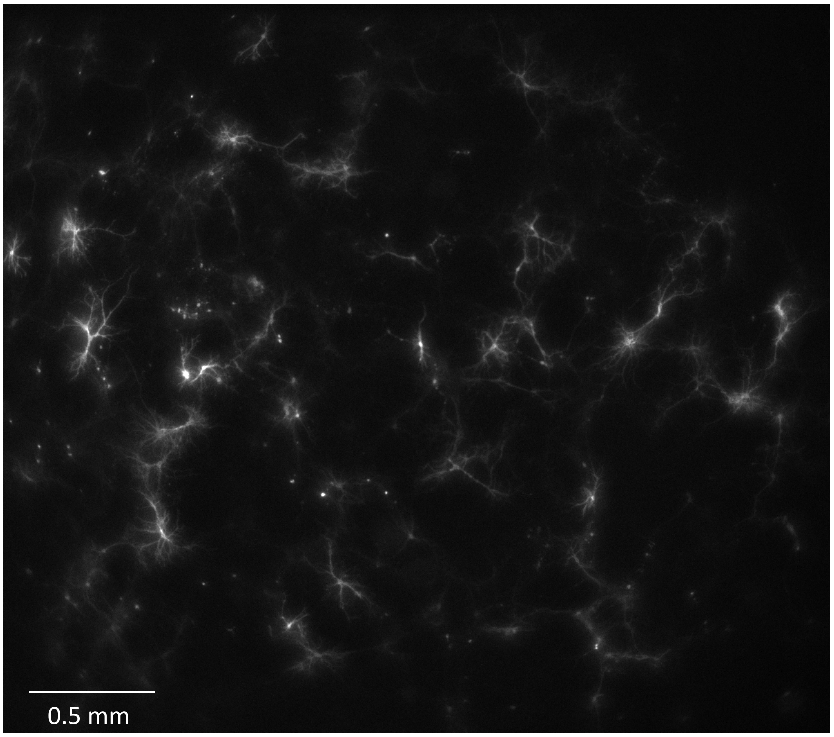

Figure 4.19: Low magnification optical system enables simultaneous imaging of many neurons. Neurons expressing Optopatch2, imaged via eGFP fluorescence. More than 50 cells are visible in this field of view. Limitations on data-rate from the camera required that the field of view be compressed in the vertical direction to 0.6 mm for optical recordings at 1 kHz, or to 1.2 mm for optical recordings at 500 Hz.

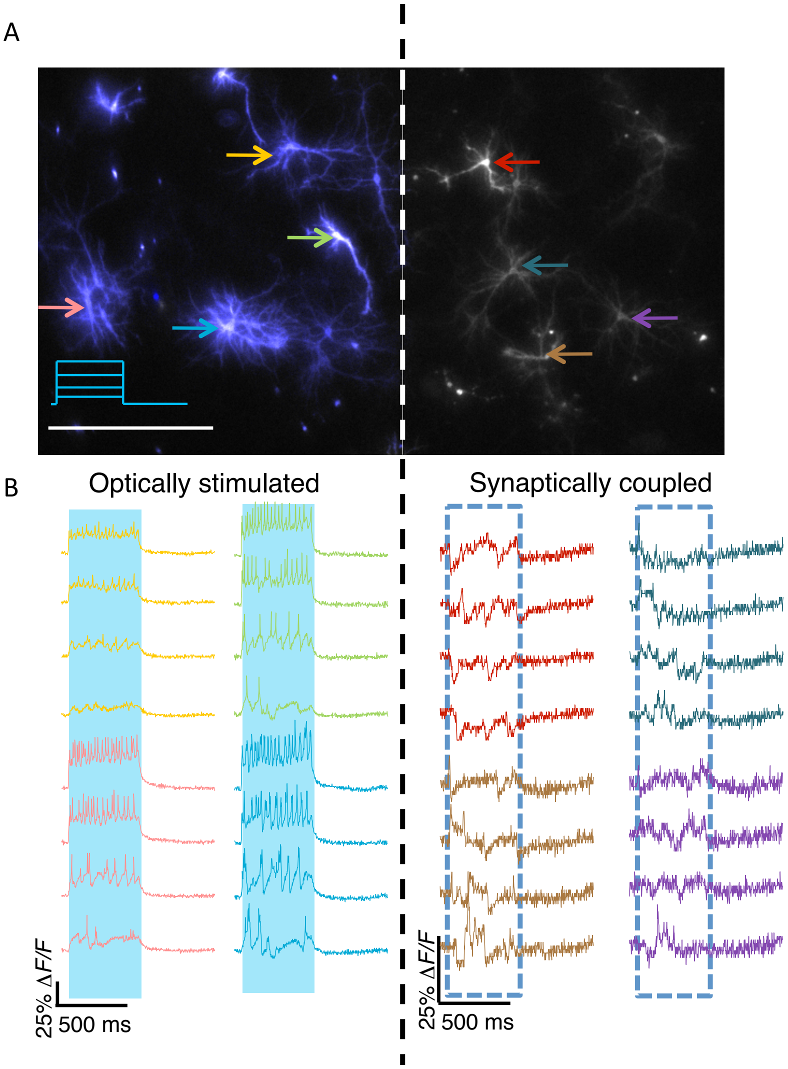

Figure 4.20: Optopatch measurements of network activity. A) Image of eGFP fluorescence in a culture of neurons expressing Optopatch2. The left half of the field (colored blue) was stimulated with blue light of increasing intensity (0.5 s, 1 to 10 mW/cm²) and the whole field was illuminated with red light (100 W/cm²). B) Left: fluorescence traces showing APs in the neurons indicated in (A) with correspondingly colored arrows. Right: synaptically induced activity in the indicated neurons which did not receive direct optical stimulation. Scale bar 500 μm.

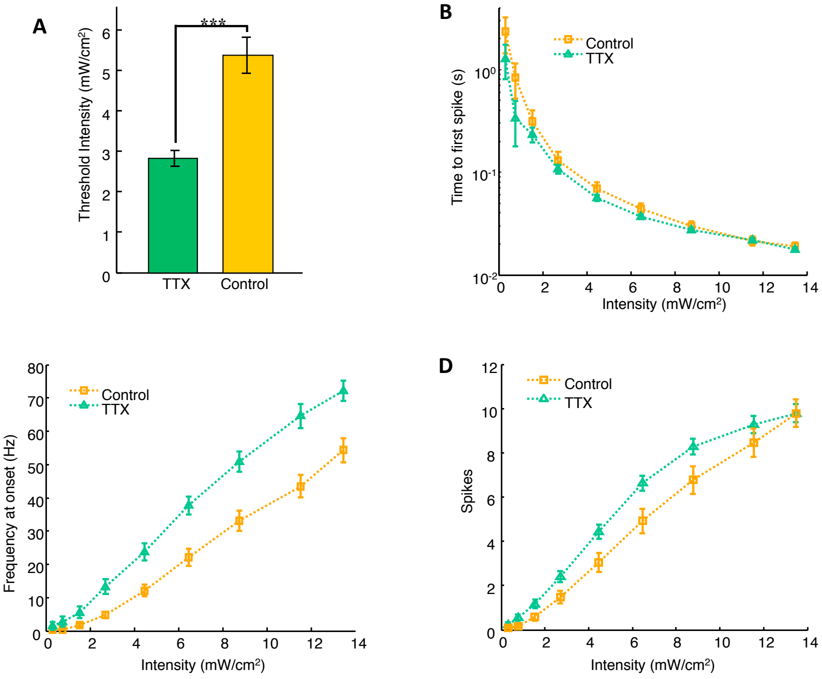

Figure 4.21: Homeostasis of intrinsic excitability in primary neurons induced by chronic exposure to TTX. Neurons expressing Optopatch2 were incubated in 1 μM TTX for 48 hours starting at 16 days post plating, and then tested in TTX-free imaging medium. Paired control dishes from the same culture were incubated with vehicle alone. Data from $n = 75$ control cells and $n = 94$ TTX-treated cells. QuasAr2 fluorescence was monitored (640 nm, 100 W/cm^2) while cells were illuminated with pulses of blue light (500 ms) of increasing intensity (0 to 14 mW/cm^2, repeated twice). A) Threshold blue light stimulation intensity to induce at least one AP in 500 ms. TTX treated cells had a significantly lower threshold than controls ($P = 5\times10^{-6}$). B) Time from onset of illumination to first spike. TTX-treated and control cells did not differ substantially by this measure. C) Spike frequency at onset (inverse time between first and second spike). TTX-treated cells fired faster than control cells ($P < 0.001$ for each stimulation intensity 2.7 mW/cm^2). D) Number of spikes during 500 ms stimulus window. TTX-treated cells had more spikes than control cells ($P < 0.01$ for stimulus intensities between 0.8 and 8.8 mW/cm^2). Error bars represent s.e.m. *** $P < 0.001$. Statistical significance determined by two-tailed student's t-test or Mann–Whitney U test.

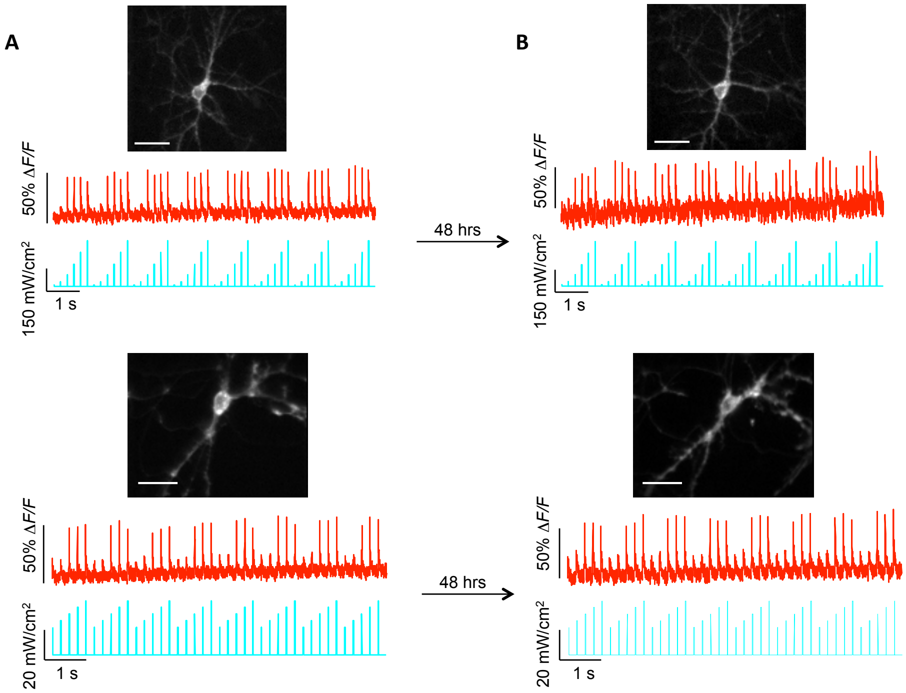

Figure 4.22: Repeated Optopatch recordings from neurons expressing Optopatch2. Images show mOrange2 fluorescence. Scale bar 40 μm. A) Primary rat hippocampal neurons were stimulated with pulses of blue light of increasing intensity, targeted to the soma (blue). Cells produced optically detected APs under the stronger stimuli. The stimulus and imaging protocol lasted 1 min. After the recording, the imaging medium was replaced with culture medium and the cells were returned to the incubator. B) 48 hrs later, the same cells were located in the microscope and the stimulus protocol was repeated. The cells responded similarly in the first and second trial. Paired recordings separated by 48 hrs were successful in n = 8 of 10 cells.

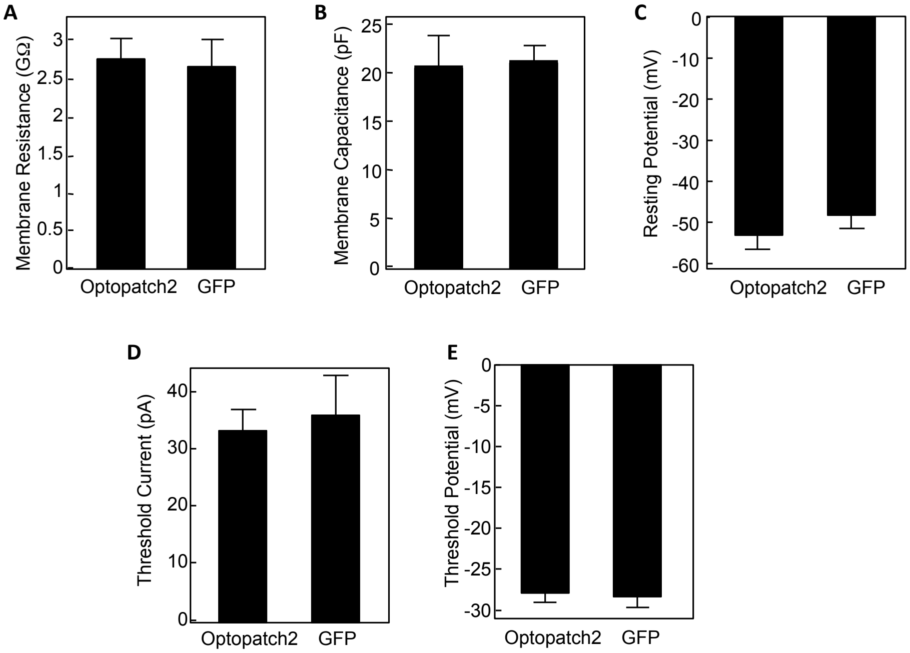

Figure 4.23: Effect of Optopatch expression on membrane electrical properties of hiPSC-derived neurons. Matched cultures were transfected via calcium phosphate on DIV 10 with either cytoplasmic eGFP or Optopatch2 in identical plasmids with a CaMKIIα promoter. Expressing cells (n = 11 Optopatch2, n = 11 eGFP, DIV 20) were measured via whole-cell patch clamp. There was no significant difference in A) membrane resistance (P = 0.82), B) membrane capacitance (P = 0.88), or C) resting potential (P = 0.34) between Optopatch2 and eGFP expressing cells. Threshold current and potential for action potential initiation were determined by applying increasing steps in current (20-120 pA, 100 ms duration, repeated at 1 Hz). There was no significant difference in D) threshold current (P = 0.78) or E) potential (P = 0.43) between Optopatch2 and eGFP expressing cells. Error bars represent s.e.m. Statistical significance determined by two-tailed student's t-test or Mann–Whitney U test.

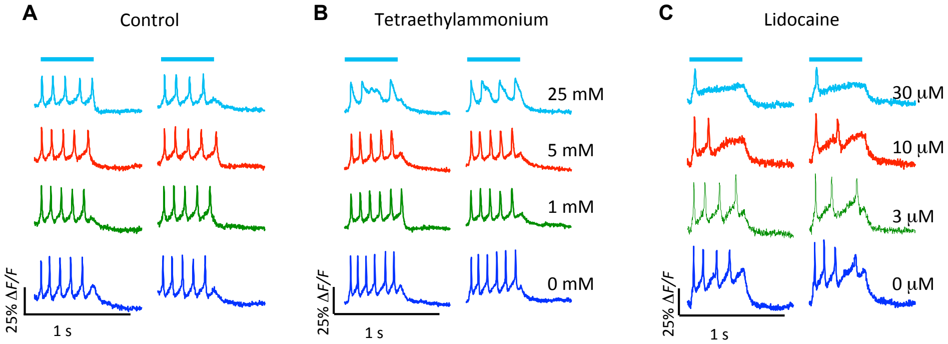

Figure 4.24: Influence of channel blockers on excitability of hiPSC-derived neurons. A) Human iPSC-derived neurons were excited with 500 ms pulses of blue light to initiate a train of APs. Repeated stimulation with blue light led to repeatable trains of APs. B) Representative AP trains with increasing concentrations of tetraethylammonium (TEA), a voltage-gated potassium channel blocker. TEA blocked repolarization after AP initiation. C) Representative AP trains with increasing concentrations of lidocaine, an activity-dependent sodium channel blocker. Lidocaine prevented repetitive firing.

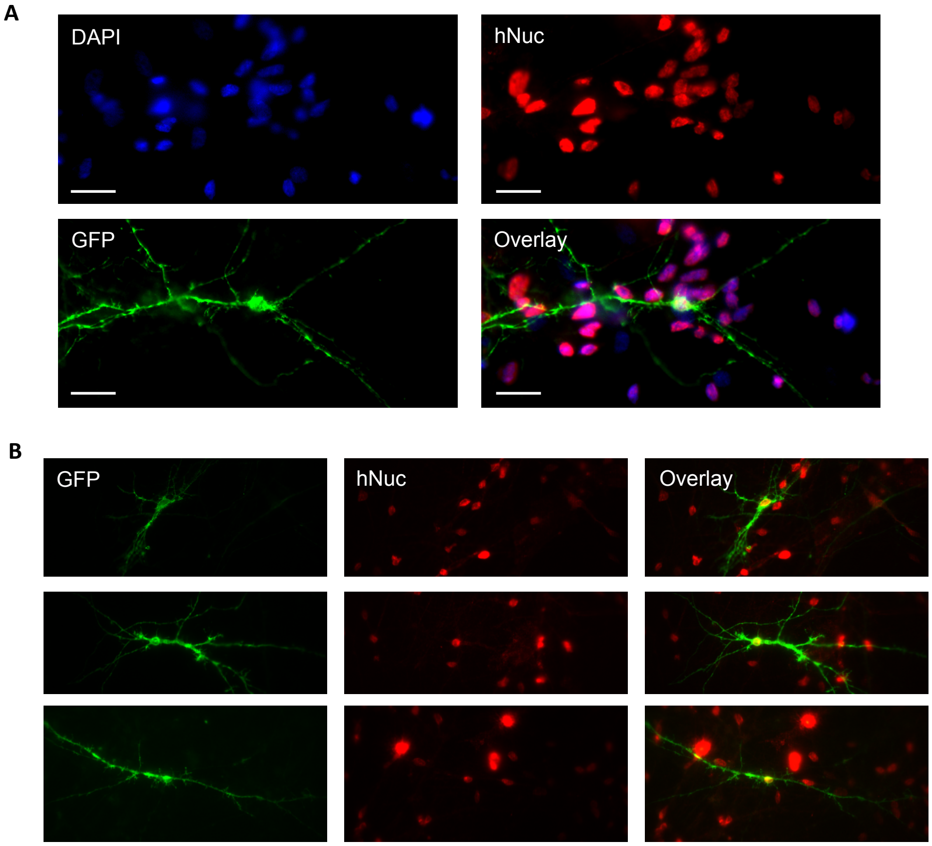

Figure 4.25: Immunostaining to validate human origin of hiPSC-derived neurons. A) Measurement of specificity of anti-human nuclear antigen 1 (*hNuc*) antibody for human cells. In a culture of hiPSC-derived neurons on rat glia, all nuclei were stained with DAPI (blue). A subset of these stained with *hNuc*, indicating two antigenically different populations. A subset of the hNuc-positive cells stained for GFP. These were hiPSC-derived neurons that had taken up and expressed the Optopatch construct. Scale bars 20 μm. B) Human iPSC-derived neurons used in experiments on homeostatic plasticity were fixed immediately after data acquisition and immunostained against eGFP to label transfected neurons and *hNuc* to label human nuclei. All eGFP expressing cells (277 of 277) showed colocalization of the *hNuc* with GFP.

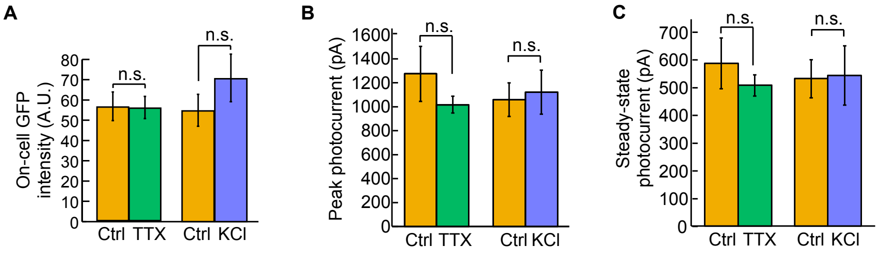

Figure 4.26: Tests of TTX or KCl chronic treatment on CheRiff expression and function in hiPSC-derived neurons. A) Fluorescence of eGFP can be used as a proxy for the expression level of CheRiff. Images of eGFP fluorescence were acquired for all cells used in HPIE measurements. The mean eGFP fluorescence intensity was quantified for each cell. There was no significant difference in intensity levels between TTX treated cells (n = 31 cells) and their untreated controls (n = 32 cells, P = 0.59). There was also no significant difference in intensity levels between KCl treated cells (n = 28 cells) and their untreated controls (n = 25 cells, P = 0.29). B) & C) Characterization of photocurrents in treated and untreated cells. Cells were transfected and treated identically to the optical HPIE experiments. Membrane voltage was held at V = -65 mV via manual patch clamp. Photocurrents were elicited by a blue light pulse (1 s, 488 nm, 500 mW/cm^2). There was no significant difference in peak or steady state photocurrents between TTX treated cells and untreated controls (n = 8 TTX treated cells, n = 10 untreated control cells, P = 0.31 for peak photocurrents, P = 0.44 for steady-state photocurrents). There was also no significant difference in peak or steady-state photocurrents between KCl treated cells and untreated controls (n = 7 KCl treated cells, n = 7 untreated control cells, P = 0.69 for peak photocurrents, P = 0.78 for steady-state photocurrents). Error bars represent s.e.m. Statistical significance determined by two-tailed student's t-test or Mann–Whitney U test.

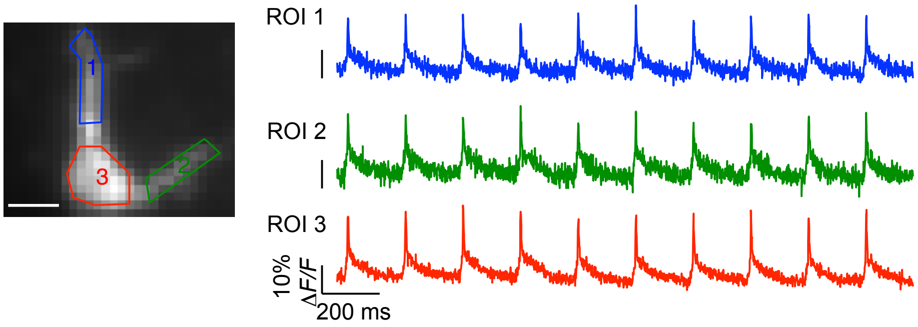

Figure 4.27: Subcellular optopatch measurements in organotypic brain slice. Optical recordings (640 nm, 1,200 W/cm² nominal incident intensity; 1 kHz frame rate on an EMCCD) of optically evoked action potentials (10 ms, 7.5 mW/cm², repeated at 5 Hz) in a neuron expressing Optopatch2 in a brain slice. Subcellular fluorescence was extracted by selecting regions of interest (ROIs) around two proximal dendrites and the cell body. Single-trial APs were seen clearly with high SNR in the dendrites, as well as the cell body. Scale bar 15 μm.

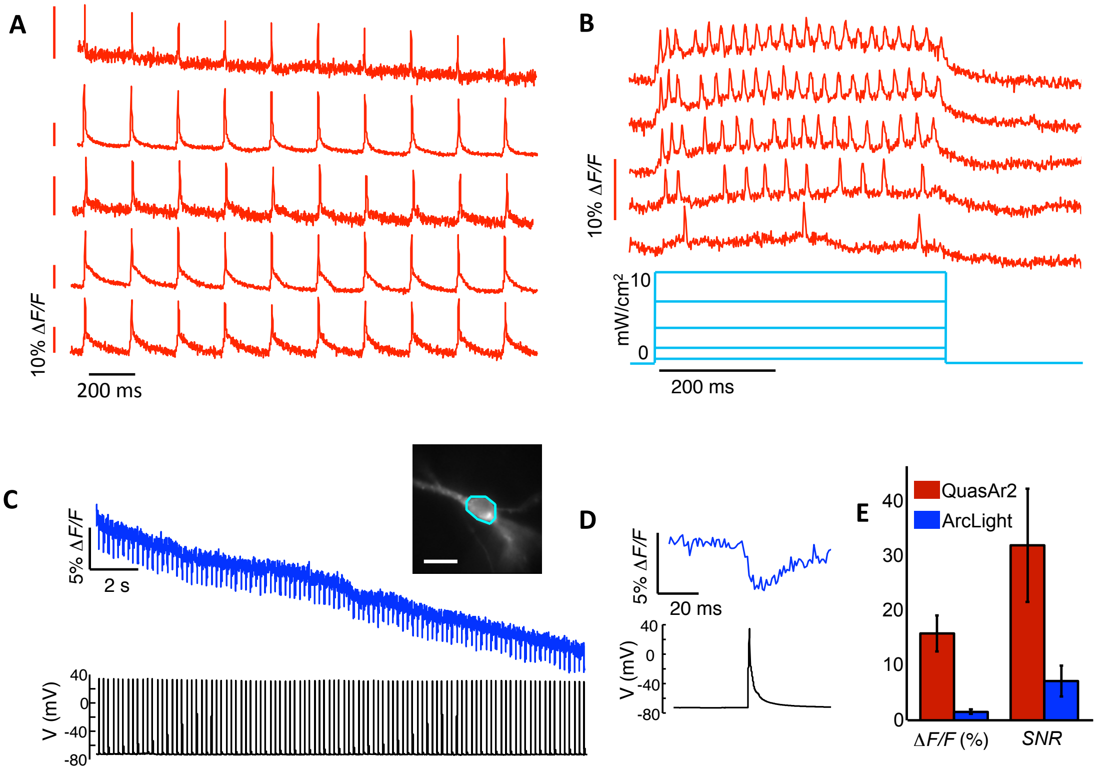

Figure 4.28: Optopatch and ArcLight measurements in organotypic brain slice. A) Optical recordings of optically evoked action potentials in five cells from separately prepared brain slices expressing QuasAr2. Differences in signal-to-noise ratio reflect differences in cell depth and in expression level. Action potentials were induced with blue light (10 ms, 7.5-15 mW/cm^2, repeated at 5 Hz) and whole-soma fluorescence was recorded at a frame rate of 1 kHz on an EMCCD camera (640 nm illumination 1,200 W/cm^2 nominal incident intensity, not corrected for light scatter). B) Sustained spiking in response to steps in blue light intensity (488 nm, 500 ms, increasing intensity from 1 to 10 mW/cm^2). QuasAr2 fluorescence was excited with illumination at 640 nm, 400 W/cm^2 incident on the sample, not corrected for scattering. C) Trace of fluorescence transients in a neuron expressing ArcLight A242 (488 nm, 50 W/cm^2) in response to a train of APs. Inset: Image of the neuron. Scale bar 20 μm. Cyan box shows ROI used to extract fluorescence from a high-speed (1 kHz frame rate) movie. D) Single-trial fluorescence response of ArcLight (blue) to a single AP (black). E) Comparison of QuasAr2 and ArcLight in brain slice. For detection of a single AP, QuasAr2 $\Delta F/F$ was 15.9 ± 3.0% ($n = 7$ cells), 10-fold larger than ArcLight $\Delta F/F$ (1.5 ± 0.4%, $n = 6$ cells). QuasAr2 SNR was 31.9 ± 9.5, over 4-fold larger than ArcLight SNR of 7.1 ± 2.8. Illumination conditions for E) were: ArcLight, 488 nm, 50 W/cm^2; QuasAr2, 640 nm, 1200 W/cm^2. Fluorescence was extracted by manual ROI selection of the soma for both ArcLight and QuasAr2. All fluorescent traces and $\Delta F/F$ calculations are presented without background subtraction or correction for photobleaching.

4.6 SUPPLEMENTARY TABLES

Table 4.1: Quantum yields (QYs) of Arch variants measured in solubilized protein. Fluorescence emission spectra were recorded with excitation at 600 nm. Details of sample preparation and measurement are given in **Methods Section 4.4**. *Due to the low light intensities used to determine QYs, fluorescence from Arch was not detected above baseline.

Protein Name	Quantum yield	Quantum yield relative to Arch D95N
Arch	N/A*	N/A*
Arch D95N	4×10^{-4}	1
QuasAr1	8×10^{-3}	19
QuasAr2	4×10^{-3}	10
Arch D95H/D106H	2×10^{-3}	4.2
Arch D95H/D106H/P60S	5×10^{-3}	12
Arch D95H/D106H/F161V	5×10^{-3}	13

Table 4.2: Spectroscopic and kinetic properties of Arch mutants and ArcLight. Brightness, response speed, and sensitivity were measured in HEK293 cells. Brightness and voltage sensitivity were comparable at 34 °C and 23 °C.

Mutant	**Brightness (λ_{exc} = 640 nm)**		**τ_{up} (ms, -70 mV to +30 mV)**			**τ_{down} (ms, +30 mV to -70 mV)**			**Sensitivity (ΔF/F per 100 mV)**
	0.7 W/cm^2	800 W/cm^2	τ_1	τ_2	% τ_1	τ_1	τ_2	% τ_1	
23 °C									
Arch(WT)	1	4.0	0.6	NA	NA	0.25	1.9	67%	40%
QuasAr1	15.2	10.3	0.05	3.2	94%	0.07	1.9	88%	32%
QuasAr2	3.4	3.4	1.2	11.8	68%	1.0	15.9	80%	90%
Arclight A242			17.4	123	39%	68	121	24%	-32%
34 °C									
QuasAr2			0.3	3.2	62%	0.3	4.0	73%	
Arclight A242			12	72	78%	21.5	NA	100%	

Table 4.3: Spectroscopic and kinetic properties of *Scherffelia dubia* mutants. Photocurrents were measured in cultured rat hippocampal neurons under voltage-clamp at Vm = -65 mV. All quantities are represented as mean ± s.e.m. for n = 5 to 7 cells.

Mutant	**Trafficking**	**Blue photocurrent (pA; peak, 0.5 W/cm^2)**	**Red photocurrent (pA; 640 nm, 300 W/cm^2)**	**t_{off} (ms)**
sdChR-eGFP	×			
sdChR-TS-eGFP	✓	2470±170 ✓	38±4 ×	26±2.9 ×
CheRiff (sdChR-E154A-TS-eGFP)	✓	2030 ± 100 ✓	10.5±2.8 ✓	16±0.5 ✓

Table 4.4: Comparison of CheRiff, ChIEF, and ChR2 H134R. All parameters were measured in cultured rat hippocampal neurons. Photocurrents were measured under voltage-clamp at Vm = -65 mV. All quantities are represented as mean ± s.e.m. for n = 5 to 7 cells. EPD50 = intensity for 50% maximal photocurrent.

ChR variant	I_{max} (nA; 488 nm, 0.5 W/cm^2)		t_{on} (ms)	τ_{des} (ms)	τ_{off} (ms)	EPD50 (mW/cm^2)	Red photocurrent (pA; 640 nm, 300 W/cm^2)	Red light depolarization (mV), 300 W/cm^2
	Peak	Steady state						
CheRiff	2.0±0.1	1.33±0.08	4.5±0.3	400±40	16±0.8	22±4	10.5 ± 2.8	2.3 ± 0.3
ChIEF	0.9±0.1	0.81±0.10	18±1.8	51±10	15±2		15.0 ± 2.5	2.1 ± 0.15
ChR2 H134R	1.1±0.1	0.65±0.09	9.1±0.7	40±5	25±4	43±4	2.2 ± 0.9	1.0

Table 4.5: Crosstalk between CheRiff and QuasAr channels in Optopatch constructs. Photocurrents were measured in cultured rat hippocampal neurons under voltage-clamp at Vm = -65 mV. Photocurrents are represented as mean ± s.e.m. for n = 5 to 7 cells. Fluorescence values were measured in HEK293 cells. Fluorescence of QuasAr constructs is normalized to the value for QuasAr2 illuminated at 640 nm, 300 W/cm^2.

	Peak CheRiff photocurrent (pA)	**Fluorescence**	
		QuasAr1	**QuasAr2**
Blue (500 mW/cm^2)	2030±100	0.02	0.017
Red (300 W/cm^2)	10.5±2.8	3	1

4.7 Supplementary Movies

4.7.1 Supplementary Movie

`http://www.nature.com/nmeth/journal/v11/n8/fig_tab/nmeth.3000_SV1.html`

Raw QuasAr2 fluorescence from a neuron expressing Optopatch2, imaged at 1 kHz frame rate. Fluorescence was excited by whole-field red illumination (640 nm, 300 W/cm^2). Activity was induced via whole-field blue light illumination (488 nm, 20 mW/cm^2, 10 ms pulses, repeated at 5 Hz). Portions of the intervals between action potentials have been elided to maintain manageable movie size. Movie acquired on an sCMOS camera.

4.7.2 Supplementary Movie

`http://www.nature.com/nmeth/journal/v11/n8/fig_tab/nmeth.3000_SV2.html`

Same data as in **Supplementary Movie 4.7.1**, averaged over 98 temporally registered action potentials. The average fluorescence intensity is shown in grayscale in the background, and the change in fluorescence is shown as a colormap. Movie acquired on an sCMOS camera.

4.7.3 SUPPLEMENTARY MOVIE

`http://www.nature.com/nmeth/journal/v11/n8/fig_tab/nmeth.3000_SV3.html`

Movie of an action potential (averaged over n = 203 optically evoked action potentials) in a neuron expressing Optopatch1. Region receiving blue light stimulus is shown in blue. The subthreshold voltage spreads during stimulation, followed by a spike in cell-wide fluorescence which peaked within two frames. Movie acquired on an EMCCD camera.

4.7.4 SUPPLEMENTARY MOVIE

`http://www.nature.com/nmeth/journal/v11/n8/fig_tab/nmeth.3000_SV4.html`

Sub-frame interpolated movie showing action potential initiation and propagation in the neuron shown in **Supplementary Movie 4.7.3**. Region receiving blue light stimulus is shown in blue. Action potential initiation occurs at the distal end of the axon initial segment. The movie was constructed from an average of n = 203 optically evoked action potentials. Movie acquired on an EMCCD camera.

4.7.5 SUPPLEMENTARY MOVIE

`http://www.nature.com/nmeth/journal/v11/n8/fig_tab/nmeth.3000_SV5.html`

Sub-frame interpolated movie showing action potential initiation and propagation in a neuron expressing Optopatch1, with blue light stimulation targeted to the soma. The movie was acquired using the same parameters as in **Supplementary Movie 4.7.3**. The movie was constructed from an average of n = 383 optically evoked action potentials. Movie acquired on an EMCCD camera.

4.7.6 SUPPLEMENTARY MOVIE

`http://www.nature.com/nmeth/journal/v11/n8/fig_tab/nmeth.3000_SV6.html`

Sub-frame interpolated movie showing action potential initiation and propagation in a neuron expressing Optopatch1, with blue light stimulation targeted to a small group of dendrites. The movie was acquired using the same parameters as in **Supplementary Movie 4.7.3**. The movie was constructed from an average of n = 338 optically evoked action potentials. Movie acquired on an EMCCD camera.

4.7.7 Supplementary Movie

`http://www.nature.com/nmeth/journal/v11/n8/fig_tab/nmeth.3000_SV7.html`

Spontaneous network activity in neurons expressing Optopatch2, monitored with red illumination (640 nm, 100 W/cm^2) in a field of view 1 mm × 3 mm. The movie was acquired at a 500 Hz frame rate. Movie acquired on an sCMOS camera.

4.7.8 Supplementary Movie

`http://www.nature.com/nmeth/journal/v11/n8/fig_tab/nmeth.3000_SV8.html`

Simultaneous excitation and recording of action potentials in many neurons expressing Optopatch2. A pulse of blue light (500 ms, 5 mW/cm^2) was applied to stimulate neural activity via excitation of CheRiff, and activity was monitored with red illumination (640 nm, 100 W/cm^2) in a field of view 1 mm × 3 mm. The blue dot next to the time stamp indicates when the blue light is on. Synaptic blockers were added to prevent network activity. The movie was acquired at a 500 Hz frame rate. Movie acquired on an sCMOS camera.

4.8 MANUSCRIPT INFORMATION

4.8.1 PREVIOUSLY PUBLISHED AS

A version of this chapter appeared in [62]:

D. R. Hochbaum*, Y. Zhao*, S. Farhi, et al. All-optical electrophysiology in mammalian neurons using engineered microbial rhodopsins. *Nature Methods*, 11(8): 825–833, 2014.

4.8.2 ACKNOWLEDGEMENTS

We thank N. Anand, L. Rosenbaum, T. Shen, and V. Nathan for technical assistance, Y. Cho, A. Douglass, A. Ting, F. Zhang, L. Looger, and D. Kim for helpful discussions. We thank Cellular Dynamics Inc. for technical assistance with hiPSC neurons. This work was supported by the Harvard Center for Brain Science, PECASE award N00014-11-1-0549, US National Institutes of Health grants 1-R01-EB012498 and New Innovator grant 1-DP2-OD007428, the Harvard–Massachusetts Institute of Technology Joint Research Grants Program in Basic Neuroscience, a National Science Foundation Graduate Fellowship (D.R.H., S.L.F), the Natural Sciences and Engineering Research Council of Canada (Discovery grants to R.E.C. and D.J.H), the Canadian Institutes of Health Research (R.E.C.), and graduate scholarships from the University of Alberta and Alberta Innovates (Y.Z.). R.E.C. holds a Tier II Canada Research Chair. ESB was supported by DARPA Living Foundries HR0011-12-C-0068, the MIT Media Lab, McGovern Institute, and Synthetic Intelligence projects, NYSCF Robertson Neuroscience Investigator Award, IET A. F. Harvey Prize, Skolkovo Institute of Science and Technology, NIH grants 1R01NS075421, 1R01NS067199, 1DP2OD002002, and 1R01DA029639, Human Frontiers Science Program, and NSF CAREER Award CBET 1053233 and EFRI 0835878. Work in VNM's lab was supported by NIH grants R01DC011291 and R01DC013329. The 1000 Plants (1KP) initiative, led by GKSW, is funded by the Alberta Ministry of Enterprise and Advanced Education, Alberta Innovates Technology Futures (AITF) Innovates Centre of Research Excellence (iCORE), Musea Ventures, and BGI-Shenzhen.

4.8.3 The Author's Contribution

Daniel R. Hochbaum designed the Optopatch construct and system. Yongxin Zhao and Daniel R. Hochbaum engineered the QuasArs. Daniel R. Hochbaum, Nathan Klapoetke, and Yong Ku Cho engineered CheRiff. Daniel R. Hochbaum and Sami L. Farhi acquired the optical electrophysiology data. Christopher A. Werley developed the low-magnification imaging system. Vikrant Kapoor and Jessica Saulnier assisted with the slice experiments. Peng Zou assisted with measurements of rhodopsin photophysics. Joel Kralj screened ion-channel blockers on hiPSC-derived neurons. Niklas Smedmark-Margulies assisted with cell culture. Gabriella L. Boulting performed immunostaining in hiPSC-derived neurons. Christoph Straub assisted with measurements of ArcLight in slice. Michael Melkonian and Gane Wong provided the transcriptomic data from which SdChR was mined and phenotyped. Daniel R. Hochbaum, Dougal Maclaurin, and Adam E. Cohen analyzed the data. Daniel R. Hochbaum and Adam E. Cohen wrote the paper with input from Sami L. Farhi, Yongxin Zhao and Robert Campbell. Jed Harrison, Venkatesh Murthy, Bernardo Sabatini, Ed Boyden, and Robert Campbell supervised aspects of the research. Adam E. Cohen oversaw the project.

5

Conclusion

After years of development, the goal of a genetically-defined, direct and robust readout of membrane potential appears to be within reach. The past two years have seen an explosion of new and improved probes based on fusions of fluorescent proteins (FPs) to voltage sensitive domains [75, 152]; and probes based on microbial rhodopsin scaffolds whose readouts include direct endogenous fluorescence [62] and fluorescence modulation of fused FPs via FRET-coupling to the voltage-dependent rhodopsin absorption spectrum [171]. All the viable sensors require improvements to become ubiquitous tools for neuroscience, and it is unclear which, if any, of the existing GEVI scaffolds offer an ideal solution. The QuasAr proteins would benefit from further engineering to improve their (one- and two-photon) brightness, while maintaining their high sensitivity and rapid kinetics. However, many exciting questions and applications are ready to be tackled with currently available or soon-to-be available tools. Below I discuss two directions.

APPLICATIONS TO HIPSC MODELS OF DISEASE

The networks formed by cells in a culture dish are random, and are unlikely to recapitulate disease phenotypes associated with network level mis-wiring and disorder (although *in vitro* assays, such as 3D cell culture, are under development [54]). However, iPSC-derived neurons do provide a model system for understanding cell-autonomous changes in the context of human neurological disease. The Optopatch protocols developed in **Chapter 4** are a starting point for high-throughput studies of diseases that affect intrinsic excitability of the cell. Optopatch measurements on many cells provide immense amounts of information and statistics which can be gleaned in higher-level analyses than we initially pursued. For example, parameterizing features of the electrical waveforms may reveal subtle phenotypes which might be missed by lower-throughput manual patch clamp techniques where far fewer cells are measured.

New protocols must be developed for diseases that perturb the function of synapses. When studying synaptic disorders in a dish, it may be more informative to characterize single connections rather than monitoring network activity. Carefully designing high-throughput protocols to uncover and disambiguate pre- and post-synaptic deficits will generate a more complete picture of cellular physiology in disease states.

Finally, neurological disorders differentially affect different cell-types. Expanding the palette of available iPSC-derived neuronal cell-types [105] will expand the predictive power of this model system.

IN VIVO ALL-OPTICAL ELECTROPHYSIOLOGY

Many exciting challenges lie ahead for *in vivo* all-optical electrophysiology. Apart from GEVI optimization, there remains a need for improved hardware in order to record the activity of large ensembles of neurons simultaneously. While techniques have been reported for wide-field imaging with single cell resolution in small model organisms such as *C. elegans* [131] and zebrafish [1], further development is required for larger rodent model systems. Scanning two-photon microscopy is suitable for monitoring many individual neurons when looking at slow activity-dependent calcium transients (with GECIs), however faster techniques will be required for voltage imaging [30, 64]. An alternative approach to speeding up hardware is to engineer memory storage into the indicator, which can be accessed after the epoch of interest. Light-gated integrators of neuronal activity are now being actively developed [162].

Presently, neuronal cell-types are largely characterized by transcriptional and molecular fingerprints, and single-cell electrophysiology. Brain regions are identified by their cell-type composition, anatomical organization, and functional connectivity. Optical electrophysiology promises to generate an orthogonal approach to understanding the brain by allowing experimenters to directly observe the electrical dynamics of neurons within a circuit during stimulation or behavior. In doing so, one can define functional and computational roles for individual cells, and identify distinctive neuronal dynamics for different brain regions.

My hope is that the tools presented here will add to the growing arsenal of technologies used to dissect brain circuitry and understand the electrophysiology underlying neurodegenerative and psychiatric disease.

Bibliography

[1] M. B. Ahrens, M. B. Orger, D. N. Robson, J. M. Li, and P. J. Keller. Whole-brain functional imaging at cellular resolution using light-sheet microscopy. *Nature methods*, 10(5):413–420, 2013.

[2] W. Akemann, H. Mutoh, A. Perron, J. Rossier, and T. Knopfel. Imaging brain electric signals with genetically targeted voltage-sensitive fluorescent proteins. *Nature methods*, 7(8):643–649, Aug 2010.

[3] W. Akemann, H. Mutoh, A. Perron, et al. Imaging neural circuit dynamics with a voltage-sensitive fluorescent protein. *Journal of neurophysiology*, 108 (8):2323–2337, Oct 2012.

[4] K. Ataka and V. A. Pieribone. A genetically targetable fluorescent probe of channel gating with rapid kinetics. *Biophysical journal*, 82(1):509–516, 2002.

[5] B. D. Auerbach, E. K. Osterweil, and M. F. Bear. Mutations causing syndromic autism define an axis of synaptic pathophysiology. *Nature*, 480 (7375):63–68, 2011.

[6] J. Badger, O. Cordero-Llana, E. Hartfield, and R. Wade-Martins. Parkinson's disease in a dish-using stem cells as a molecular tool. *Neuropharmacology*, 76:88–96, 2014.

[7] B. J. Baker, H. Lee, V. A. Pieribone, et al. Three fluorescent protein voltage sensors exhibit low plasma membrane expression in mammalian cells. *Journal of neuroscience methods*, 161(1):32–38, MAR 30 2007.

[8] B. J. Baker, H. Mutoh, D. Dimitrov, et al. Genetically encoded fluorescent sensors of membrane potential. *Brain Cell Biology*, 36(1-4):53–67, AUG 2008.

[9] G. Banker and K. Goslin. *Culturing nerve cells*. The MIT Press, Cambridge, MA, 1998.

[10] D. P. Barondeau, C. D. Putnam, C. J. Kassmann, J. A. Tainer, and E. D. Getzoff. Mechanism and energetics of green fluorescent protein chromophore synthesis revealed by trapped intermediate structures. *Proceedings of the National Academy of Sciences*, 100(21):12111–12116, 2003.

[11] B. P. Bean. The action potential in mammalian central neurons. *Nature Reviews Neuroscience*, 8(6):451–465, 2007.

[12] O. Beja, L. Aravind, E. V. Koonin, et al. Bacterial rhodopsin: Evidence for a new type of phototrophy in the sea. *Science*, 289(5486):1902–1906, 2000.

[13] O. Beja, E. N. Spudich, J. L. Spudich, M. Leclerc, and E. F. Delong. Proteorhodopsin phototrophy in the ocean. *Nature*, 411(6839):786–789, 2001.

[14] V. Bergo, E. N. Spudich, J. L. Spudich, and K. J. Rothschild. Conformational changes detected in a sensory rhodopsin ii-transducer complex. *The Journal of biological chemistry*, 278(38):36556–36562, Sep 19 2003.

[15] G. G. Blasdel and G. Salama. Voltage-sensitive dyes reveal a modular organization in monkey striate cortex. *Nature*, 321(6070):579–585, 1986.

[16] J. A. Bohnert, B. Karamian, and H. Nikaido. Optimized nile red efflux assay of acrab-tolc multidrug efflux system shows competition between substrates. *Antimicrobial Agents and Chemotherapy*, 54(9):3770–3775, 2010.

[17] A. Borst, D. Heck, and M. Thomann. Voltage signals of individual purkinje cell dendrites in rat cerebellar slices. *Neuroscience letters*, 238(1-2):29–32, 1997.

[18] G. L. Boulting, E. Kiskinis, G. F. Croft, et al. A functionally characterized test set of human induced pluripotent stem cells. *Nature biotechnology*, 29 (3):279–286, 2011.

[19] E. S. Boyden, F. Zhang, E. Bamberg, G. Nagel, and K. Deisseroth. Millisecond-timescale, genetically targeted optical control of neural activity. *Nature neuroscience*, 8(9):1263–1268, 2005.

[20] J. Bradley, R. Luo, T. S. Otis, and D. A. DiGregorio. Submillisecond optical reporting of membrane potential in situ using a neuronal tracer dye. *Journal of Neuroscience*, 29(29):9197–9209, 2009.

[21] T. Branco, B. A. Clark, and M. Hausser. Dendritic discrimination of temporal input sequences in cortical neurons. *Science*, 329(5999):1671–1675, 2010.

[22] M. D. Cahalan, H. Wulff, and K. G. Chandy. Molecular properties and physiological roles of ion channels in the immune system. *Journal of clinical immunology*, 21(4):235–252, 2001.

[23] G. Cao, J. Platisa, V. A. Pieribone, et al. Genetically targeted optical electrophysiology in intact neural circuits. *Cell*, 154:904–913, 2013.

[24] G. Chen, N. C. Harata, and R. W. Tsien. Paired-pulse depression of unitary quantal amplitude at single hippocampal synapses. *Proceedings of the National Academy of Sciences of the United States of America*, 101(4):1063–1068, 2004.

[25] T.-W. Chen, T. J. Wardill, Y. Sun, et al. Ultrasensitive fluorescent proteins for imaging neuronal activity. *Nature*, 499(7458):295–300, 2013.

[26] Z. Cheng and R. E. Campbell. Assessing the structural stability of designed beta-hairpin peptides in the cytoplasm of live cells. *ChemBioChem*, 7(8): 1147–1150, 2006.

[27] B. Y. Chow, X. Han, A. S. Dobry, et al. High-performance genetically targetable optical neural silencing by light-driven proton pumps. *Nature*, 463: 98–102, 2010.

[28] M. M. Churchland, B. M. Yu, M. Sahani, and K. V. Shenoy. Techniques for extracting single-trial activity patterns from large-scale neural recordings. *Curr. Op. Neurobio.*, 17:609–618, 2007.

[29] L. B. Cohen, R. D. Keynes, and B. Hille. Light scattering and birefringence changes during nerve activity. *Nature*, 218:438–441, 1968.

[30] H. Dana, A. Marom, S. Paluch, et al. Hybrid multiphoton volumetric functional imaging of large-scale bioengineered neuronal networks. *Nature Communications*, 5, 2014.

[31] J. T. Davie, M. H. P. Kole, J. J. Letzkus, et al. Dendritic patch-clamp recording. *Nature Protocols*, 1(3):1235–1247, 2006.

[32] A. H. Delcour, B. Martinac, J. Adler, and C. Kung. Modified reconstitution method used in patch-clamp studies of escherichia coli ion channels. *Biophysical journal*, 56(3):631–636, 1989.

[33] N. S. Desai, L. C. Rutherford, and G. G. Turrigiano. Plasticity in the intrinsic excitability of cortical pyramidal neurons. *Nature neuroscience*, 2(6):515–520, 1999.

[34] A. K. Dioumaev, J. M. Wang, Z. Balint, G. Varo, and J. K. Lanyi. Proton transport by proteorhodopsin requires that the retinal schiff base counterion asp-97 be anionic. *Biochemistry*, 42(21):6582–6587, 2003.

[35] D. A. Dombeck, C. D. Harvey, L. Tian, L. L. Looger, and D. W. Tank. Functional imaging of hippocampal place cells at cellular resolution during virtual navigation. *Nature neuroscience*, 13(11):1433–1440, 2010.

[36] N. Enami, K. Yoshimura, M. Murakami, et al. Crystal structures of archaerhodopsin-1 and-2: Common structural motif in archaeal light-driven proton pumps. *Journal of Molecular Biology*, 358(3):675–685, 2006.

[37] L. Fenno, O. Yizhar, and K. Deisseroth. The development and application of optogenetics. *Annual Review of Neuroscience*, 34:389–412, 2011.

[38] R. M. Fitzsimonds, H. jun Song, and M. ming Poo. Propagation of activity-dependent synaptic depression in simple neural networks. *Nature*, 388 (6641):439–448, 1997.

[39] A. Foust, M. Popovic, D. Zecevic, and D. A. McCormick. Action potentials initiate in the axon initial segment and propagate through axon collaterals

reliably in cerebellar purkinje neurons. *The Journal of Neuroscience*, 30(20): 6891–6902, 2010.

[40] T. Friedrich, S. Geibel, R. Kalmbach, et al. Proteorhodopsin is a light-driven proton pump with variable vectoriality. *Journal of Molecular Biology*, 321(5): 821–838, Aug 30 2002.

[41] P. Fromherz and C. O. Muller. Voltage-sensitive fluorescence of amphiphilic hemicyanine dyes in neuron membrane. *Biochimica et Biophysica Acta (BBA)-Biomembranes*, 1150(2):111–122, 1993.

[42] P. Fromherz, G. Hubener, B. Kuhn, and M. J. Hinner. Annine-6plus, a voltage-sensitive dye with good solubility, strong membrane binding and high sensitivity. *European Biophysics Journal*, 37(4):509–514, 2008.

[43] D. C. Fung and H. C. Berg. Powering the flagellar motor of escherichia coli with an external voltage source. *Nature*, 375:809–812, 1995.

[44] T. Furuta, S. S. H. Wang, J. L. Dantzker, et al. Brominated 7-hydroxycoumarin-4-ylmethyls: photolabile protecting groups with biologically useful cross-sections for two photon photolysis. *Proceedings of the National Academy of Sciences*, 96(4):1193–1200, 1999.

[45] Y. Gong, J. Z. Li, and M. J. Schnitzer. Enhanced archaerhodopsin fluorescent protein voltage indicators. *PLOS ONE*, 8(6):e66959, 2013.

[46] V. Gradinaru, F. Zhang, C. Ramakrishnan, et al. Molecular and cellular approaches for diversifying and extending optogenetics. *Cell*, 141:154–165, 2010.

[47] A. Grinvald and R. Hildesheim. Vsdi: a new era in functional imaging of cortical dynamics. *Nat Rev Neurosci*, 5(11):874–885, 2004.

[48] A. Grinvald, B. Salzberg, and L. Cohen. Simultaneous recording from several neurones in an invertebrate central nervous system. *Nature*, 268 (5616):140–142, 1977.

[49] A. Grinvald, A. Fine, I. C. Farber, and R. Hildesheim. Fluorescence monitoring of electrical responses from small neurons and their processes. *Biophysical journal*, 42(2):195–198, 1983.

[50] A. Grinvald, E. Lieke, R. D. Frostig, C. D. Gilbert, and T. N. Wiesel. Functional architecture of cortex revealed by optical imaging of intrinsic signals. *Nature*, 324:361–364, 1986.

[51] A. Grinvald, B. Salzberg, V. Lev-Ram, and R. Hildesheim. Optical recording of synaptic potentials from processes of single neurons using intracellular potentiometric dyes. *Biophysical Journal*, 51(4):643 – 651, 1987.

[52] E. Gross, R. S. B. Jr, and L. M. Loew. Dual-wavelength ratiometric fluorescence measurement of the membrane dipole potential. *Biophysical journal*, 67(1):208–216, 1994.

[53] M. S. Grubb and J. Burrone. Activity-dependent relocation of the axon initial segment fine-tunes neuronal excitability. *Nature*, 465(7301):1070–1074, 2010.

[54] U. A. Gurkan, Y. Fan, F. Xu, et al. Simple precision creation of digitally specified, spatially heterogeneous, engineered tissue architectures. *Advanced Materials*, 25(8):1192–1198, 2013.

[55] M. C. Gustin, B. Martinac, Y. Saimi, M. R. Culbertson, and C. Kung. Ion channels in yeast. *Science*, 233(4769):1195–1197, 1986.

[56] M. T. Harnett, J. K. Makara, N. Spruston, W. L. Kath, and J. C. Magee. Synaptic amplification by dendritic spines enhances input cooperativity. *Nature*, 491(7425):599–602, Nov 22 2012.

[57] C. Harvey, P. Coen, and D. Tank. Choice-specific sequences in parietal cortex during a virtual-navigation decision task. *Nature*, 484:62–68, 2012.

[58] U. Haupts, J. Tittor, E. Bamberg, and D. Oesterhelt. General concept for ion translocation by halobacterial retinal proteins: the isomerization/switch/transfer (ist) model. *Biochemistry*, 36(1):2–7, 1997.

[59] A. J. Heron, J. R. Thompson, B. Cronin, H. Bayley, and M. I. Wallace. Simultaneous measurement of ionic current and fluorescence from single protein pores. *Journal of the American Chemical Society*, 131(5):1652–1653, 2009.

[60] N. Higurashi, T. Uchida, C. Lossin, et al. A human dravet syndrome model from patient induced pluripotent stem cells. *Molecular brain*, 6(1):19, 2013.

[61] D. Hill and R. Keynes. Opacity changes in stimulated nerve. *The Journal of physiology*, 108(3):278–281, 1949.

[62] D. R. Hochbaum*, Y. Zhao*, S. Farhi, et al. All-optical electrophysiology in mammalian neurons using engineered microbial rhodopsins. *Nature Methods*, 11(8):825–833, 2014.

[63] M. A. Holden, D. Needham, and H. Bayley. Functional bionetworks from nanoliter water droplets. *Journal of the American Chemical Society*, 129(27): 8650–8655, 2007.

[64] T. F. Holekamp, D. Turaga, and T. E. Holy. Fast three-dimensional fluorescence imaging of activity in neural populations by objective-coupled planar illumination microscopy. *Neuron*, 57(5):661–672, 2008.

[65] R. Homma, B. J. Baker, L. Jin, et al. Wide-field and two-photon imaging of brain activity with voltage-and calcium-sensitive dyes. *Philosophical Transactions of the Royal Society B: Biological Sciences*, 364(1529):2453, 2009.

[66] J. H. Hou, V. Venkatachalam, and A. E. Cohen. Temporal dynamics of microbial rhodopsin fluorescence reports absolute membrane voltage. *Biophysical journal*, 106(3):639–648, 2014.

[67] D. Huber, D. Gutnisky, S. Peron, et al. Multiple dynamic representations in the motor cortex during sensorimotor learning. *Nature*, 484(7395):473–478, 2012.

[68] W. Humphrey, E. Bamberg, and K. Schulten. Photoproducts of bacteriorhodopsin mutants: a molecular dynamics study. *Biophysical journal*, 72 (3):1347–1356, 1997.

[69] Q. J. Huys, M. B. Ahrens, and L. Paninski. Efficient estimation of detailed single-neuron models. *Journal of neurophysiology*, 96(2):872–890, 2006.

[70] K. Ihara, T. Umemura, I. Katagiri, et al. Evolution of the archaeal rhodopsins: evolution rate changes by gene duplication and functional differentiation. *Journal of Molecular Biology*, 285(1):163–174, 1999.

[71] E. S. Imasheva, K. Shimono, S. P. Balashov, et al. Formation of a long-lived photoproduct with a deprotonated schiff base in proteorhodopsin, and its enhancement by mutation of asp 227. *Biochemistry*, 44(32):10828–10838, 2005.

[72] W. J. Ingledew and R. K. Poole. The respiratory chains of escherichia coli. *Microbiology and Molecular Biology Reviews*, 48(3):222–222–271, 1984.

[73] J. Jiang and R. Yuste. Second-harmonic generation imaging of membrane potential with photon counting. *Microscopy and Microanalysis*, 14(6):526–531, DEC 2008.

[74] M. Jiang and G. Chen. High ca2+ -phosphate transfection efficiency in low-density neuronal cultures. *Nature protocols*, 1(2):695–700, 2006.

[75] L. Jin, Z. Han, J. Platisa, et al. Single action potentials and subthreshold electrical events imaged in neurons with a fluorescent protein voltage probe. *Neuron*, 75(5):779–785, 2012.

[76] M. T. J. Johnson, E. J. Carpenter, Z. Tian, et al. Evaluating methods for isolating total rna and predicting the success of sequencing phylogenetically diverse plant transcriptomes. *PloS one*, 7(11):e50226, 2012.

[77] A. K. Joshi, S. Ahmed, and G. F.-L. Ames. Energy coupling in bacterial periplasmic transport systems. studies in intact escherichia coli cells. *Journal of Biological Chemistry*, 264(4):2126–2126–2133, 1989.

[78] J. S. Kauer. Real-time imaging of evoked activity in local circuits of the salamander olfactory bulb. *Nature*, 331(6152):166–168, 1988.

[79] Y. Kirichok, G. Krapivinsky, and D. E. Clapham. The mitochondrial calcium uniporter is a highly selective ion channel. *Nature*, 427(6972):360–364, 2004.

[80] Y. Kirichok, B. Navarro, and D. E. Clapham. Whole-cell patch-clamp measurements of spermatozoa reveal an alkaline-activated ca2+ channel. *Nature*, 439(7077):737–740, 2006.

[81] R. D. Kirkton and N. Bursac. Engineering biosynthetic excitable tissues from unexcitable cells for electrophysiological and cell therapy studies. *Nature Communications*, 2:300, 2011.

[82] N. C. Klapoetke, Y. Murata, S. S. Kim, et al. Independent optical excitation of distinct neural populations. *Nature methods*, 11:338–346, 2014.

[83] T. Knopfel, M. Z. Lin, A. Levskaya, et al. Toward the second generation of optogenetic tools. *Journal of neuroscience*, 30(45):14998–15004, Nov 10 2010.

[84] M. H. Kole and G. J. Stuart. Signal processing in the axon initial segment. *Neuron*, 73(2):235–247, 2012.

[85] P. Kolodner, E. P. Lukashev, Y. Ching, and D. L. Rousseau. Electric-field-induced schiff-base deprotonation in d85n mutant bacteriorhodopsin. *Proceedings of the National Academy of Sciences*, 93(21):11618–11621, 1996.

[86] T. Kotnik and D. Miklavcic. Analytical description of transmembrane voltage induced by electric fields on spheroidal cells. *Biophysical journal*, 79(2): 670–679, 2000.

[87] J. M. Kralj, D. R. Hochbaum, A. D. Douglass, and A. E. Cohen. Electrical spiking in escherichia coli probed with a fluorescent voltage indicating protein. *Science*, 333:345–348, 2011.

[88] J. M. Kralj*, A. D. Douglass*, D. R. Hochbaum*, D. Maclaurin, and A. E. Cohen. Optical recording of action potentials in mammalian neurons using a microbial rhodopsin. *Nature Methods*, 9(1):90–95, 2012.

[89] R. H. Kramer, D. L. Fortin, and D. Trauner. New photochemical tools for controlling neuronal activity. *Current opinion in neurobiology*, 19(5):544–552, 2009.

[90] M. E. Lambo and G. G. Turrigiano. Synaptic and intrinsic homeostatic mechanisms cooperate to increase l2/3 pyramidal neuron excitability during a late phase of critical period plasticity. *The Journal of Neuroscience*, 33 (20):8810–8819, 2013.

[91] J. K. Lanyi. Proton translocation mechanism and energetics in the light-driven pump bacteriorhodopsin. *Biochimica et biophysica acta*, 1183(2):241–261, Dec 7 1993.

[92] J. K. Lanyi. Bacteriorhodopsin. *Annual Review of Physiology*, 66:665–688, 2004.

[93] M. O. Lenz, R. Huber, B. Schmidt, et al. First steps of retinal photoisomerization in proteorhodopsin. *Biophysical journal*, 91(1):255–262, 2006.

[94] D. H. Lim, M. H. Mohajerani, J. Ledue, et al. In vivo large-scale cortical mapping using channelrhodopsin-2 stimulation in transgenic mice reveals asymmetric and reciprocal relationships between cortical areas. *Frontiers in neural circuits*, 6:11, Mar 15 2012.

[95] J. Y. Lin, M. Z. Lin, P. Steinbach, and R. Y. Tsien. Characterization of engineered channelrhodopsin variants with improved properties and kinetics. *Biophysical journal*, 96(5):1803–1814, 2009.

[96] J. Livet, T. A. Weissman, H. Kang, et al. Transgenic strategies for combinatorial expression of fluorescent proteins in the nervous system. *Nature*, 450(7166):56–62, 2007.

[97] C. J. Lo, M. C. Leake, and R. M. Berry. Fluorescence measurement of intracellular sodium concentration in single escherichia coli cells. *Biophysical journal*, 90(1):357–365, 2006.

[98] C. J. Lo, M. C. Leake, T. Pilizota, and R. M. Berry. Nonequivalence of membrane voltage and ion-gradient as driving forces for the bacterial flagellar motor at low load. *Biophysical journal*, 93(1):294–302, 2007.

[99] L. L. Looger and O. Griesbeck. Genetically encoded neural activity indicators. *Current opinion in neurobiology*, 22(1):18–23, 2012.

[100] A. Losonczy and J. C. Magee. Integrative properties of radial oblique dendrites in hippocampal ca1 pyramidal neurons. *Neuron*, 50:291–307, 2006.

[101] A. Lundby, H. Mutoh, D. Dimitrov, W. Akemann, and T. Knopfel. Engineering of a genetically encodable fluorescent voltage sensor exploiting fast ci-vsp voltage-sensing movements. *PLoS One*, 3(6):2514, 2008.

[102] D. Ma, N. Zerangue, Y.-F. Lin, et al. Role of er export signals in controlling surface potassium channel numbers. *Science*, 291(5502):316–319, 2001.

[103] D. Maclaurin, V. Venkatachalam, H. Lee, and A. E. Cohen. Mechanism of voltage-sensitive fluorescence in a microbial rhodopsin. *Proc. Natl. Acad. Sci. USA*, 110:5939–5944, 2013.

[104] M. C. Marchetto, C. Carromeu, A. Acab, et al. A model for neural development and treatment of rett syndrome using human induced pluripotent stem cells. *Cell*, 143(4):527–539, 2010.

[105] A. M. Maroof, S. Keros, J. A. Tyson, et al. Directed differentiation and functional maturation of cortical interneurons from human embryonic stem cells. *Cell Stem Cell*, 12(5):559–572, 2013.

[106] B. Martinac, M. Buechner, A. H. Delcour, J. Adler, and C. Kung. Pressure-sensitive ion channel in escherichia coli. *Proceedings of the National Academy of Sciences of the United States of America*, 84(8):2297–2301, 1987.

[107] B. Martinac, Y. Saimi, and C. Kung. Ion channels in microbes. *Physiological Reviews*, 88(4):1449, 2008.

[108] J. Mattis, K. M. Tye, E. A. Ferenczi, et al. Principles for applying optogenetic tools derived from direct comparative analysis of microbial opsins. *Nature methods*, 9(2):159–172, 2012.

[109] K. D. McCarthy and J. D. Vellis. Preparation of separate astroglial and oligodendroglial cell cultures from rat cerebral tissue. *The Journal of cell biology*, 85(3):890–902, 1980.

[110] M. Melkonian and H. R. Preisig. A light and electron microscopic study of scherffelia dubia, a new member of the scaly green flagellates (prasinophyceae). *Nordic Journal of Botany*, 6(2):235–256, 1986.

[111] G. Miesenbock, D. A. D. Angelis, and J. E. Rothman. Visualizing secretion and synaptic transmission with ph-sensitive green fluorescent proteins. *Nature*, 394(6689):192–195, Jul 9 1998.

[112] E. W. Miller, J. Y. Lin, E. P. Frady, et al. Optically monitoring voltage in neurons by photo-induced electron transfer through molecular wires. *Proceedings of the National Academy of Sciences*, 109(6):2114–2119, 2012.

[113] V. Montana, D. L. Farkas, and L. M. Loew. Dual-wavelength ratiometric fluorescence measurements of membrane potential. *Biochemistry*, 28(11): 4536–4539, 1989.

[114] E. A. Mukamel, A. Nimmerjahn, and M. J. Schnitzer. Automated analysis of cellular signals from large-scale calcium imaging data. *Neuron*, 63(6): 747–760, 2009.

[115] T. Nagai, K. Ibata, E. S. Park, et al. A variant of yellow fluorescent protein with fast and efficient maturation for cell-biological applications. *Nature biotechnology*, 20(1):87–90, 2002.

[116] E. Neher and B. Sakmann. Single-channel currents recorded from membrane of denervated frog muscle fibres. *Nature*, 260(5554):799–802, 1976.

[117] D. G. Nicholls and M. W. Ward. Mitochondrial membrane potential and neuronal glutamate excitotoxicity: mortality and millivolts. *Trends in neurosciences*, 23(4):166–174, 2000.

[118] T. Noumi, M. Maeda, and M. Futai. Mode of inhibition of sodium azide on h+-atpase of escherichia coli. *FEBS letters*, 213(2):381–384, 1987.

[119] L. Novikova, L. Novikov, and J. O. Kellerth. Persistent neuronal labeling by retrograde fluorescent tracers: a comparison between fast blue, fluorogold and various dextran conjugates. *Journal of neuroscience methods*, 74(1): 9–15, 1997.

[120] D. Novo, N. G. Perlmutter, R. H. Hunt, and H. M. Shapiro. Accurate flow cytometric membrane potential measurement in bacteria using diethyloxacarbocyanine and a ratiometric technique. *Cytometry*, 35(1):55–63, 1999.

[121] A. L. Obaid and B. M. Salzberg. Optical recording of electrical activity in guinea-pig enteric networks using voltage-sensitive dyes. *J. Vis. Exp.*, 34, 2009.

[122] D. Oesterhelt, M. Meentzen, and L. Schuhmann. Reversible dissociation of the purple complex in bacteriorhodopsin and identification of 13-cis and all-trans-retinal as its chromophores. *European Journal of Biochemistry*, 40 (2):453–463, 1973.

[123] L. M. Palmer and G. J. Stuart. Membrane potential changes in dendritic spines during action potentials and synaptic input. *Journal of neuroscience*, 29(21):6897–6903, May 27 2009.

[124] J. Park, C. A. Werley, V. Venkatachalam, et al. Screening fluorescent voltage indicators with spontaneously spiking hek cells. *PloS one*, 8(12):e85221, Dec 31 2013.

[125] S. Peron and K. Svoboda. From cudgel to scalpel: toward precise neural control with optogenetics. *Nature methods*, 8(1):30–34, 2010.

[126] A. Perron, H. Mutoh, W. Akemann, et al. Second and third generation voltage-sensitive fluorescent proteins for monitoring membrane potential. *Front Mol Neurosci.*, 2:1–8, 2009.

[127] D. S. Peterka, H. Takahashi, and R. Yuste. Imaging voltage in neurons. *Neuron*, 69(1):9, 2011.

[128] L. Petreanu, T. Mao, S. M. Sternson, and K. Svoboda. The subcellular organization of neocortical excitatory connections. *Nature*, 457(7233):1142–1145, 2009.

[129] M. A. Popovic, A. J. Foust, D. A. McCormick, and D. Zecevic. The spatiotemporal characteristics of action potential initiation in layer 5 pyramidal neurons: a voltage imaging study. *J. Physiol.*, 589:4167–4187, 2011.

[130] D. C. Prasher, V. K. Eckenrode, W. W. Ward, F. G. Prendergast, and M. J. Cormier. Primary structure of the aequorea victoria green-fluorescent protein. *Gene*, 111(2):229 – 233, 1992.

[131] R. Prevedel, Y.-G. Yoon, M. Hoffmann, et al. Simultaneous whole-animal 3d imaging of neuronal activity using light-field microscopy. *Nature methods*, 11(7):727–730, 2014.

[132] G. Pucihar and T. Kotnik. Measuring the induced membrane voltage with di-8-anepps. *Journal of Visualized Experiments*, 33(33):e1659, 2009.

[133] M. Rehorek and M. P. Heyn. Binding of all-trans-retinal to the purple membrane. evidence for cooperativity and determination of the extinction coefficient. *Biochemistry*, 18(22):4977–4983, 1979.

[134] N. Ruiz, S. S. Chang, A. Hiniker, D. Kahne, and T. J. Silhavy. Nonconsecutive disulfide bond formation in an essential integral outer membrane protein. *Proceedings of the National Academy of Sciences*, 107(27):12245, 2010.

[135] B. L. Sabatini and K. Svoboda. Analysis of calcium channels in single spines using optical fluctuation analysis. *Nature*, 408(6812):589–593, 2000.

[136] R. Sakai, V. Repunte-Canonigo, C. D. Raj, and T. Knopfel. Design and characterization of a dna-encoded, voltage-sensitive fluorescent protein. *European Journal of Neuroscience*, 13(12):2314–2318, 2001.

[137] B. Salzberg, H. Davila, and L. Cohen. Optical recording of impulses in individual neurones of an invertebrate central nervous system. *Nature*, 246 (5434):508–509, 1973.

[138] B. M. Salzberg, A. Grinvald, L. B. Cohen, H. V. Davila, and W. N. Ross. Optical recording of neuronal activity in an invertebrate central nervous system: simultaneous monitoring of several neurons. *Journal of Neurophysiology*, 40 (6):1281–1291, 1977.

[139] M. Scanziani and M. Hausser. Electrophysiology in the age of light. *Nature*, 461:930–939, 2009.

[140] B. Scharf, B. Hess, and M. Engelhard. Chromophore of sensory rhodopsin ii from halobacterium halobium. *Biochemistry*, 31(49):12486–12492, 1992.

[141] A. Schmid, M. Dehlinger-Kremer, I. Schulz, and H. Gogelein. Voltage-dependent insp3-insensitive calcium channels in membranes of pancreatic endoplasmic reticulum vesicles. *Nature*, 346(6282):374–376, 1990.

[142] G. Schmies, B. LÃ¼ttenberg, I. Chizhov, et al. Sensory rhodopsin ii from the haloalkaliphilic natronobacterium pharaonis: light-activated proton transfer reactions. *Biophysical journal*, 78(2):967–976, 2000.

[143] P. Schoenenberger, A. Grunditz, T. Rose, and T. G. Oertner. Optimizing the spatial resolution of channelrhodopsin-2 activation. *Brain cell biology*, 36 (1-4):119–127, 2008.

[144] N. C. Shaner, P. A. Steinbach, and R. Y. Tsien. A guide to choosing fluorescent proteins. *Nature Methods*, 2(12):905, 2005.

[145] A. Shcheglovitov, O. Shcheglovitova, M. Yazawa, et al. Shank3 and igf1 restore synaptic deficits in neurons from 22q13 deletion syndrome patients. *Nature*, 503:267–271, 2013.

[146] R. I. Shrager. Chemical transitions measured by spectra and resolved using singular value decomposition. *Chemometrics and Intelligent Laboratory Systems*, 1(1):59–70, 1986.

[147] M. S. Siegel and E. Y. Isacoff. A genetically encoded optical probe of membrane voltage. *Neuron*, 19:735–741, 1997.

[148] L. Sjulson and G. Miesenbock. Rational optimization and imaging in vivo of a genetically encoded optical voltage reporter. *Journal of Neuroscience*, 28 (21):5582, 2008.

[149] S. Song, P. J. Sjöström, M. Reigl, S. Nelson, and D. B. Chklovskii. Highly nonrandom features of synaptic connectivity in local cortical circuits. *PLoS Biol*, 3, 03 2005. URL `http://dx.doi.org/10.1371%2Fjournal.pbio.0030068`.

[150] G. D. Sprott, W. G. Martin, and H. Schneider. Differential effects of near-uv and visible light on active transport and other membrane processes in escherichia coli. *Photochemistry and photobiology*, 24(1):21–27, 1976.

[151] J. L. Spudich, C. S. Yang, K. H. Jung, and E. N. Spudich. Retinylidene proteins: structures and functions from archaea to humans. *Annual Review of Cell and Developmental Biology*, 16(1):365–392, 2000.

[152] F. St-Pierre, J. D. Marshall, Y. Yang, et al. High-fidelity optical reporting of neuronal electrical activity with an ultrafast fluorescent voltage sensor. *Nature neuroscience*, 17:884–889, 2014.

[153] L. Stoppini, P.-A. Buchs, and D. Muller. A simple method for organotypic cultures of nervous tissue. *Journal of neuroscience methods*, 37(2):173–182, 1991.

[154] H. Takahashi, T. Sakurai, H. Sakai, et al. Light-addressed single-neuron stimulation in dissociated neuronal cultures with sparse expression of chr2. *Biosystems*, 107(2):106–112, 2012.

[155] I. Tasaki, A. Watanabe, R. Sandlin, and L. Carnay. Changes in fluorescence, turbidity, and birefringence associated with nerve excitation. *Proceedings of the National Academy of Sciences of the United States of America*, 61(3):883–888, 1968.

[156] L. Tian, S. A. Hires, T. Mao, et al. Imaging neural activity in worms, flies and mice with improved gcamp calcium indicators. *Nature methods*, 6:875–881, 2009.

[157] J. Tittor, U. Schweiger, D. Oesterhelt, and E. Bamberg. Inversion of proton translocation in bacteriorhodopsin mutants d85n, d85t, and d85, 96n. *Biophysical journal*, 67(4):1682–1690, 1994.

[158] A. Trounson, K. A. Shepard, and N. D. DeWitt. Human disease modeling with induced pluripotent stem cells. *Current opinion in genetics and development*, 22:509–516, 2012.

[159] S. Tsuda, M. Z. Kee, C. Cunha, et al. Probing the function of neuronal populations: combining micromirror-based optogenetic photostimulation with voltage-sensitive dye imaging. *Neuroscience research*, 75:76–81, 2012.

[160] H. Tsutsui, S. Karasawa, Y. Okamura, and A. Miyawaki. Improving membrane voltage measurements using fret with new fluorescent proteins. *Nature Methods*, 5(8):683–685, 2008.

[161] G. Turrigiano, L. Abbott, and E. Marder. Activity-dependent changes in the intrinsic properties of cultured neurons. *Science*, 264(5161):974–976, 1994.

[162] V. Venkatachalam, D. Brinks, D. Maclaurin, et al. Flash memory: photochemical imprinting of neuronal action potentials onto a microbial rhodopsin. *Journal of the American Chemical Society*, 136(6):2529–2537, Feb 12 2014.

[163] J. C. Venter, K. Remington, J. F. Heidelberg, et al. Environmental genome shotgun sequencing of the sargasso sea. *Science*, 304(5667):66–74, 2004.

[164] L. Vogeley, V. D. Trivedi, O. A. Sineshchekov, et al. Crystal structure of the anabaena sensory rhodopsin transducer. *Journal of Molecular Biology*, 367 (3):741–751, 2007.

[165] K. E. Vogt, S. Gerharz, J. Graham, and M. Canepari. Combining membrane potential imaging with l-glutamate or gaba photorelease. *PloS one*, 6(10): e24911, 2011.

[166] B. J. Wainger, E. Kiskinis, C. Mellin, et al. Intrinsic membrane hyperexcitability of amyotrophic lateral sclerosis patient-derived motor neurons. *Cell reports*, 7:1–11, 2014.

[167] J. C. Williams, J. Xu, Z. Lu, et al. Computational optogenetics: empirically-derived voltage-and light-sensitive channelrhodopsin-2 model. *PLoS computational biology*, 9(9):e1003220, 2013.

[168] P. Yan, C. D. Acker, W.-L. Zhou, et al. Palette of fluorinated voltage-sensitive hemicyanine dyes. *Proceedings of the National Academy of Sciences*, 109(50): 20443–20448, 2012.

[169] H. Zhao, L. Giver, Z. Shao, J. A. Affholter, and F. H. Arnold. Molecular evolution by staggered extension process (step) in vitro recombination. *Nature biotechnology*, 16(3):258–261, 1998.

[170] Y. Zhao, S. Araki, J. Wu, et al. An expanded palette of genetically encoded ca2+ indicators. *Science*, 333(6051):1888–1891, 2011.

[171] P. Zou, Y. Zhao, A. D. Douglass, et al. Bright and fast multicoloured voltage reporters via electrochromic fret. *Nature Communications*, in press, 2014.